Coordination Chemistry Reviews 385 (2019) 44–80

Contents lists available at ScienceDirect

Coordination Chemistry Reviews

journal homepage: www.elsevier.com/locate/ccr

Review

Artificial Z-scheme photocatalytic system: What have been done and where to go?

Danlian Huang [a,b,*], Sha Chen [a,b], Guangming Zeng [a,b,*], Xiaomin Gong [a,b], Chengyun Zhou [a,b], Min Cheng [a,b], Wenjing Xue [a,b], Xuelei Yan [a,b], Jing Li [a,b]

[a] College of Environmental Science and Engineering, Hunan University, Changsha 410082, PR China
[b] Key Laboratory of Environmental Biology and Pollution Control, Hunan University, Ministry of Education, Changsha 410082, PR China

ARTICLE INFO

Article history:
Received 13 July 2018
Accepted 23 December 2018

Keywords:
Z-scheme
Photocatalysis
Visible-light-driven
Charge separation
Solar energy harvesting

ABSTRACT

Artificial Z-scheme photocatalysis has become a potential solution for resisting environmental degradation and to the worldwide energy shortage because they can effectively promote the separation of photogenerated electron-hole pairs and optimize the oxidation and reduction ability of the photocatalytic system. Currently, the application of Z-scheme photocatalysts in environmental remediation and energy conversion have ushered in a climax over the past several years. Hence, it is the ripe and right period to provide a comprehensive and state-of-the-art review on the latest achievements and the future trends of Z-scheme photocatalysis. Here, we begin with a review about the historical development of the Z-scheme photocatalytic system from redox-mediator Z-scheme photocatalytic system to current direct Z-scheme photocatalytic system. Then the latest research activities on the application of Z-scheme photocatalysts for target organic pollutants degradation, heavy metal ion redox, micro-organisms inactivation, water-splitting, H_2 and O_2 evolution are systematically summarized and highlighted. Many recent advances in Z-scheme photocatalysis have been achieved by increasing the absorption region of visible light or promoting the separation and transfer of photogenerated charge carriers to achieve optimal photocatalytic performance. Especially, we discuss the charge carrier transfer process and photocatalytic reaction pathways of key aspects of Z-scheme photocatalysts. Finally, conclusions and inspiring perspectives on the challenges of this emerging research direction are presented. We desire that insights and up-to-date information in this overview will prompt the scientific community to fully explore the potential of Z-scheme photocatalytic systems in environmental remediation and energy conversion.

Contents

* Corresponding authors at: College of Environmental Science and Engineering, Hunan University, Changsha, Hunan 410082, PR China.
E-mail addresses: huangdanlian@hnu.edu.cn (D. Huang), zgming@hnu.edu.cn (G. Zeng).

https://doi.org/10.1016/j.ccr.2018.12.013
0010-8545/

1. Introduction

With the unceasing expanding of industrialization and urbanization, the environmental pollution and energy crisis caused by over-exploited fossil fuels have become overriding issues for all countries in the world [1,2]. Therefore, it is imperative to find environment-friendly technologies for environmental remediation and to explore promising measures for the sustainable development of clean energy. Photocatalysis is an advanced oxidation process over the surface of the semiconductor photocatalyst that can generate hydrogen (H_2) by splitting water (H_2O) (Fig. 1a) [3–6], produce electric energy from solar energy (Fig. 1b) [7,8], photodegrade organic pollutants (Fig. 1c) [9,10] and reduce carbon dioxide (CO_2) to fuels (Fig. 1d) [11,12], which has been regarded as a significant technology to solve aforementioned issues since Fujishima and Honda reported the photoelectrochemcial H_2-evolution on the TiO_2 electrode in 1972 [13].

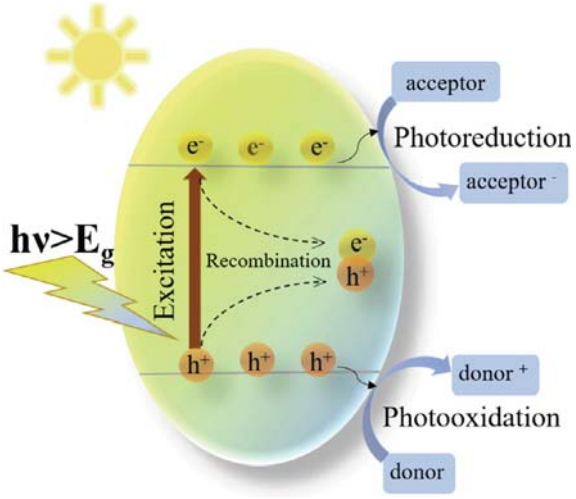

Fig. 2. Schematic illustration of semiconductor photocatalytic processes.

1.1. Basic principles of photocatalysis

Currently, it is inclined to explain the complex physicochemical processes of photocatalysis with energy band theory [14]. At absolute zero, the valence band (VB) with relatively low energy is completely occupied with electrons, while the conduction band (CB) with relatively high energy is empty. As shown in Fig. 2, in the photocatalytic process, when the absorbed energy ($h\nu$) of the semiconductor is above or equal to band gap energy (E_g), the photogenerated electrons will be excited from the VB of semiconductor to the corresponding CB, leaving holes in the VB, resulting in the electrons and holes occupying the CB and VB of semiconductor, respectively [15,16]. Then oxidative holes and reductive electrons participate in the redox reaction over the surface of semiconductor, respectively [17,18]. For target pollutants elimination, holes can directly oxidize pollutants or react with H_2O/OH^- to yield hydroxyl (**.**OH). In general, the electrons capture oxygen (O_2) to generate superoxide radical ($.O_2^-$), those generated **.**OH and $.O_2^-$ also take part in the degradation of pollutants. For energy conversion, carbon dioxide (CO_2) or H^+ can be reduced to hydrocarbon or hydrogen (H_2), and H_2O/OH^- can be oxidized to O_2 [19–23]. Among them, the key step is the capture of photogenerated electrons by O_2 to generate $.O_2^-$, which not only inhibits the recombination of photogenerated carriers, but also prolongs the lifetime of the holes [24]. However, the photogenerated electrons and holes might also

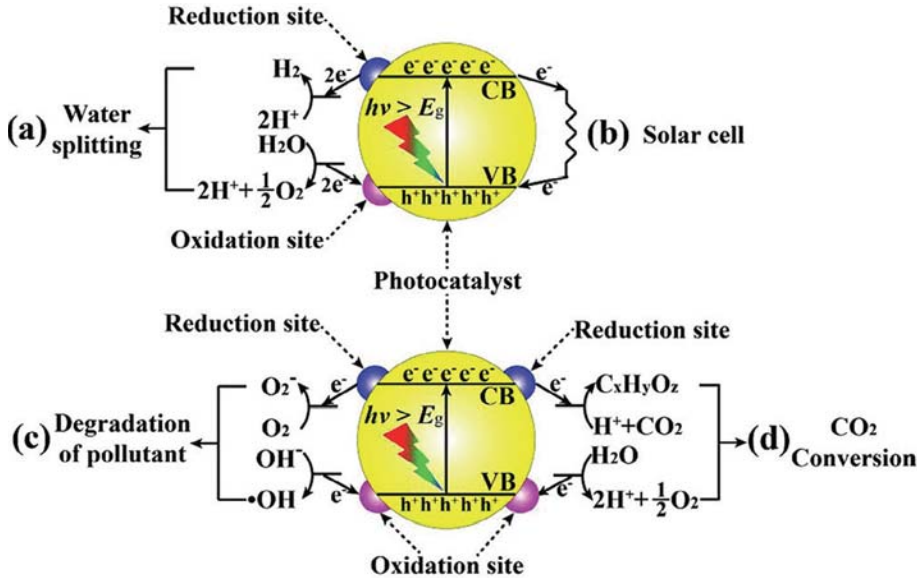

Fig. 1. (a) Photocatalytic mechanisms of water splitting, (b) solar cell, (c) photocatalytic degradation of pollutants, (d) photocatalytic reduction of CO_2. Adapted and reprinted with permission from Ref. [34], Copyright 2014 John Wiley and Sons.

recombine either on the surface or in the bulk of the semiconductor, releasing the absorbed energy as heat or light if they are not scavenged quickly after photoexcitation [25]. The rate of migration and the possibility of recombination of electron-hole pairs largely depend on the level of VB and CB and on the redox potential of the adsorbates. Oxidation reaction will occur if the oxidation potential of VB is more positive than the oxidation potential of the surface reaction. Similarly, reduction reaction will be accomplished if the reduction potential of CB is more negative than the reduction potential of the surface reaction.

The generation and recombination of photogenerated carriers in semiconductor are the two key factors that restrict the photocatalytic performance of photocatalysts. Single-component photocatalyst is hard to meet all the requirements because the photogenerated carriers of narrow band gap single-component photocatalyst are easy to recombine, whereas it is difficult to produce photogenerated electrons and holes for wide band gap single-component photocatalyst, resulting in poor quantum efficiency and low photocatalytic performance [26]. Fortunately, extensive studies have demonstrated that heterogeneous photocatalysts have several potential advantages: (1) The light absorption of wide band gap materials can be greatly enhanced by functionalizing with narrow band gap semiconductors or molecules; (2) The separation and migration of photogenerated electrons and holes can be effectively promoted due to the built-in electric field between the semiconductors; (3) The redox overpotential of active sites could be reduced by integrating the co-catalyst. For example, in 1987, the TiO_2/CdS prepared by Spanhel et al. is the most typical double-charge transfer heterogeneous photocatalysts. The blue shift of the absorption spectrum of ZnO demonstrated that photogenerated electrons in the CB of CdS are injected into the CB of attached TiO_2 under visible light irradiation [27]. Nevertheless, there are two key problems existing in the type II heterojunctions. Firstly, the CB-electrons in one semiconductor will transfer to the CB of another semiconductor having a relatively small negative potential, while the VB-holes will migrate to the VB of another semiconductor having a relatively small positive potential, thereby weakening the redox ability of photogenerated electrons and holes. Secondly, due to the electrostatic repulsion in the hole-hole or electron-electron, it is not easy for the strongly oxidative VB-holes in the semiconductor I and the strongly reductive CB-electrons in the semiconductor II to transfer to the VB of the semiconductor I and the CB of semiconductor II, respectively. Although the band structure of Z-scheme photocatalytic system is quite similar to that of the type II heterojunction, the charge transfer direction is completely different. In Z-scheme photocatalytic system, the CB-electrons in the semiconductor I with lower energy combine with the VB-holes in the semiconductor II, resulting in the strongly oxidative VB-holes and strongly reductive CB-electrons respectively in the two semiconductors, which not only improve the charge separation efficiency of individual semiconductor but also retain strong redox electron-hole to participate the photocatalytic reaction. Therefore, it can be concluded that the photocatalytic performance of Z-scheme photocatalysts is superior to that of the conventional type II heterojunction, let alone a single-component semiconductor photocatalyst, and its use will facilitate different technical applications [28]. For example, Sayama et al. successfully prepared Pt-WO_3 and Pt-$SrTiO_3$ to generate H_2 and O_2 by splitting water [29]. Some other studies are elaborated in the third section of the fourth quarter.

1.2. Rapid development of Z-scheme photocatalytic system

In order to fully understand the Z-scheme photocatalysts, it is necessary to review the development of the Z-scheme photocatalytic system. In 1960, Hill et al. proposed a hypothetical ring photoreaction pathway to explain how electrons transfer from H_2O to CO_2 between two photo-systems and accurately described the dynamic equilibrium between enzyme consumption and recovery, which is the origin of the Z-scheme system [30]. The theoretical data obtained from the hypothesis of Hill indicates that the electron transfer between two photo-systems is a spontaneous reaction [31]. Barber further illustrated the feasibility of simplifying the photo-system [32]. Inspired by the Z-scheme system in photosynthesis, the researches attempted to simplify the complex multi-mediator system into a two-step photoinduced single-mediator reaction system in which the oxidation reaction and the reduction reaction were respectively carried out on the oxidized photocatalyst (PS II) and the reduced photocatalyst (PS I), and the mediator is used to deliver electrons, whereby the Z-scheme photocatalytic system come into being [33].

Over the past few decades, there is no ending on constantly perfecting the Z-scheme photocatalytic system to improve its photocatalytic performance. Especially in the past three years, the application of Z-scheme photocatalysts on environmental restoration and energy conversion have ushered in a climax (Fig. 3). It is the ripe and appropriate period to provide a comprehensive and state-of-the-art review about the application of Z-scheme photocatalysts. As a matter of fact, several excellent reviews about Z-scheme photocatalytic system have been published. For example, Zhou et al. reported a paper about all-solid-state Z-scheme photocatalytic system, which reviewed the composition, construction, optimization and electron transfer process of photocatalytic water-splitting of Z-scheme photocatalysts [34]. Low et al. reported a review concerning the applications and characterization methods of direct Z-scheme photocatalytic system [35]. However, published reviews tend to describe several typic material such as TiO_2, g-C_3N_4, WO_3, few of them systematically describe various applications of Z-scheme photocatalytic systems based on novel materials. What's more, many advance studies have proved that Z-scheme photocatalytic systems have great potential for solving practical energy and environment problems, and much attention have been focused on how to maximize photocatalytic performance. Therefore, a comprehensive review about "what have been done and where to go?" about Z-scheme photocatalytic system is necessary, which provides some inspiration for further optimization of the Z-scheme photocatalytic system.

In line with the focus of this review, the historical development of the Z-scheme photocatalytic system is summarized, from redox-mediator to current direct Z-scheme photocatalytic system. Besides, the latest research activities in the application of the Z-scheme photocatalytic system such as the photocatalytic degradation of organic pollutants, the redox of heavy metal ion, oxidative decomposition of pathogens, water-splitting, H_2 and O_2 evolution, are systematically discussed. In particular, we discuss the charge carrier transfer process and photocatalytic reaction pathways of key aspects of Z-scheme photocatalysts. We may not mention all of the published papers due to the proliferation of papers published in this field, but rather a summary and description of these applications of Z-scheme photocatalytic system based on various novel materials. Last but not least, conclusions and inspiring perspectives on the challenges of this emerging research direction are presented at the end of the review, which demonstrates that tremendous undiscovered prospects are still present on the subject of application of the Z-scheme photocatalytic system. We hope that the insights and up-to-date information in this overview will inspire researchers to further optimize the Z-scheme photocatalytic systems from reaction conditions, crystal facet engineering, surface heterojunction and so on to achieve maximum potential for environmental remediation and energy conversion.

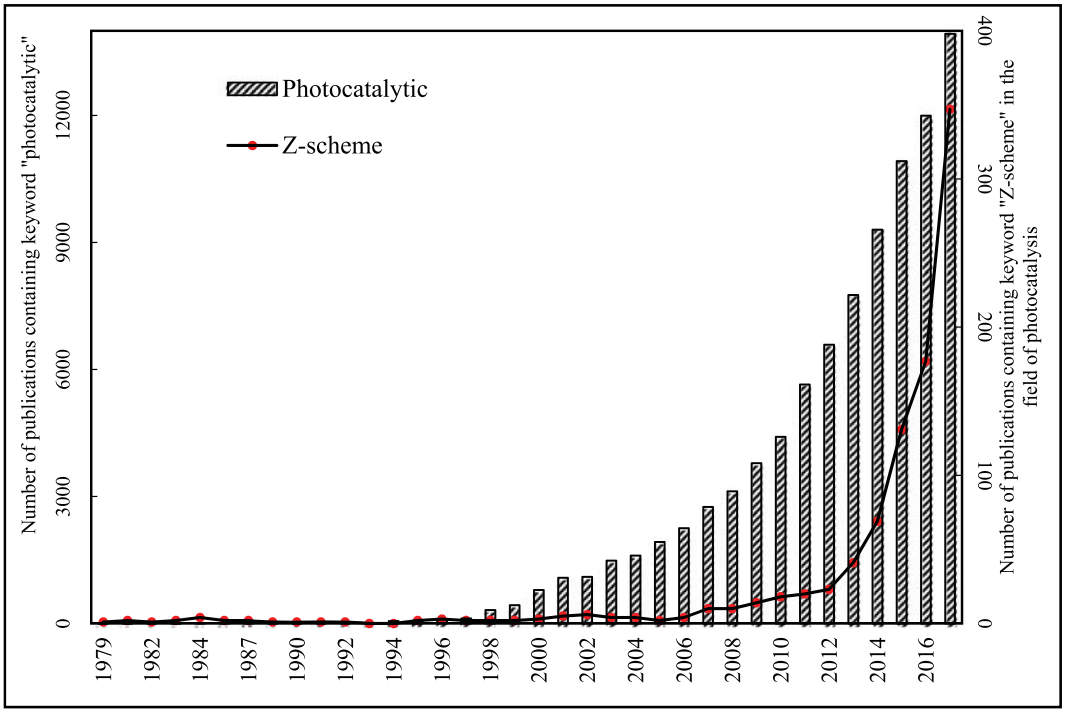

Fig. 3. Evolution of the number of publications concerning the keywords "Photocatalytic" and "Photocatalytic + Z-scheme" on indexed journals from 1979 to 2017. The data comes from the research on "web of science".

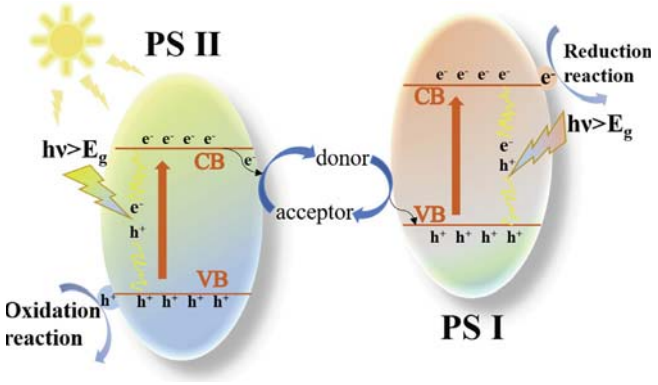

Fig. 4. Schematic illustration of the process of redox-mediator Z-scheme charge transfer.

2. Basic principles of electron transfer in Z-scheme photocatalytic system

Inspired by the biomimetic artificial photosynthesis, Bard first proposed the concept of the Z-scheme photocatalytic system in 1979 [36]. As shown in Fig. 4 that the charge carriers transfer in the Z-scheme system is initially achieved by ionic redox shuttle in solution. Both PS II and PS I are photoexcited and then generate electrons and holes respectively in their CB and VB under light irradiation. Subsequently, the photogenerated electrons in the CB of PS II transfer to the VB of PS I via a shuttle redox mediator, leaving the strong oxidizing holes in the VB of PS II and strong reductive electrons in the CB of PS I to participate in redox reaction on the surface of photocatalysts, respectively. Photogenerated electrons in the CB of PS II are consumed by reacting with high-valent ions in the redox electron mediator, while the holes in the VB of PS I react with the low-valent ions to generate high-valent ions. Hence, the concentration ratio of redox couples basically remains unchanged during the electrode reactions.

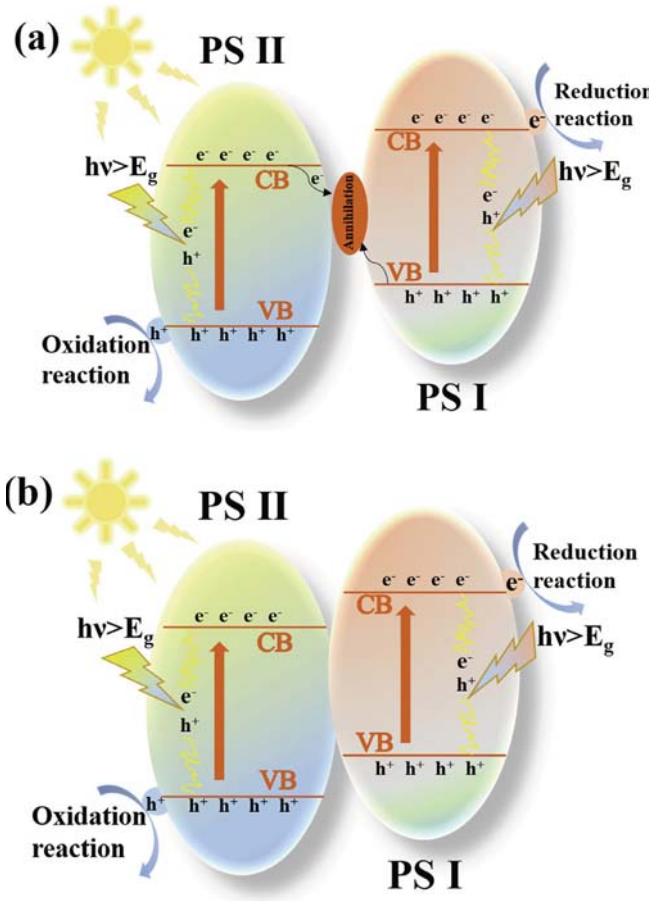

Fig. 5. Schematic illustration of the process of (a) all-solid-state Z-scheme charge transfer, (b) direct Z-scheme charge transfer.

Fe^{3+}/Fe^{2+} and IO_3^-/I^- are the most typical electron mediators in the liquid phase Z-scheme photocatalytic system. For example, Wang et al. [37] investigated the effect of IO_3^-/I^- on the O_2 evolution rate over α-Fe_2O_3 nanocrystals with different exposed facets. They found that O_2 yield of the cubic-Fe_2O_3 exposed by {0 1 2} and {1 0 4} planes in aqueous $NaIO_3$ was 85 times that of Octo-Fe_2O_3 exposed by {1 0 1} and {1 1 1}, which was ascribed to IO_3^- acting as an electron trapping agent, facilitating the separation of electrons and holes. Furthermore, Yan et al. [38] prepared TiO_2/g-C_3N_4 binary heterojunction by a hydrothermal method and overall water-splitting to H_2 and O_2 was achieved with I^-/IO_3^- or Fe^{2+}/Fe^{3+} as redox mediator. Different from Fe^{2+}/Fe^{3+} and I^-/IO_3^-, NO_3^-/NO_2^- can complete electron transfer by participating in the generation of the product. Sayama and her co-workers [39] conducted experiments on H_2 photolysis in $NaNO_2$ and Na_2CO_3 aqueous solutions, they found that the oxygen atoms in O_2 came from the photolysis of NO_3^- generated from the oxidation of NO_2^-, while CO_3^{2-} promoted the desorption of O_2 generated on the photocatalyst surface. In addition to inorganic redox mediator, studies regarding Z-scheme photocatalysts also focus on organic redox couples. Sasaki et al. [40] carried out the experiment of H_2-evolution via the photolysis of water under sunlight irradiation with $[Co(phen)_3]^{3+}/[Co(phen)_3]^{2+}$ and $[Co(bpy)_3]^{3+}/[Co(bpy)_3]^{2+}$ as electron mediators, respectively. The introduction of redox mediator in the photocatalytic system does enhance the photocatalytic performance, but redox mediator such as I^-/IO_3^-, Fe^{2+}/Fe^{3+} and NO_3^-/NO_2^- are sensitive to the reaction environment. For instance, Fe^{2+} is easily oxidized by O_2, thus the reaction must be carried out under strong acid conditions. In addition, not only the concentration ratio of ion pair changes as the reaction progresses but also ions are inefficient in gain or loss of electrons, which are also important limiting factors. What's more, redox-mediator Z-scheme photocatalytic system can only be used in the liquid phase, which greatly constrain its widely application.

To address the above defects, Tada et al. [41] proposed the concept of all-solid-state photocatalytic system consisting of two different semiconductors with a noble-metal nanoparticle as the electron mediator, in 2006. Different from the photocatalytic mechanism of the redox-mediator Z-scheme system, the photogenerated electrons in all-solid-state Z-scheme photocatalytic systems are directly transferred through the interface, shortening the distance of electron migration and improving the photocatalytic performance. In addition, Ohmic contact with low contact resistance is formed between PS II and PS I by inserting a conductor, which facilitates the recombination of the photogenerated electrons in the CB of PS II and the photogenerated holes in the VB of PS I (Fig. 5a). As a result, the strongly reductive electrons and the strongly oxidative holes remaining in the CB of PS I and the VB of PS II will respectively participate in reduction and oxidation reactions [42].

Besides, the backward reactions in redox-mediator Z-scheme photocatalytic system and the light-shielding effect caused by the redox mediator are removed. What's more, the all-solid-state Z-scheme photocatalytic system can be used not only in the liquid-phase but also gas-phase environments. Therefore, the application range of all-solid-state systems are extended from water splitting to photocatalytic CO_2 reduction, heavy metals removal, pollutants degradation and solar cells. For instance, Kim et al. synthesized a three-dimensional all-solid-state Z-scheme photocatalysts with superior photocatalytic CO_2 conversion by coating conductive carbon and $BiVO_4$ particles onto Cu_2O nanowire arrays. Due to the introduction of Cu_2O nanowire arrays as the base material, the light harvesting and the surface area of composites are greatly increased. Moreover, the charge flow follows a Z-scheme transfer path with carbon layer as an electron mediator not only achieves an efficient charge separation, but also remains strong oxidation and reduction potentials [43]. Bi@BiOCl/g-C_3N_4 having a core-shell structure of Bi spheres coated with porous g-C_3N_4 was prepared, which showed excellent photocatalytic performance in Cr(VI) reduction. Both BiOCl and g-C_3N_4 can be excited with visible light irradiation, the evoked electrons in the CB of BiOCl would transfer to the VB of porous g-C_3N_4 through metallic Bi functioned as a charge transfer bridge. The strongly redox capability of single components can be maintained, resulting in more active radicals being generated in the composite. Therefore, the photocatalytic efficiency of Cr(VI) reduction was greatly improved [44]. Three-component photocatalysts Ag/AgBr/BiOBr prepared by Ye et al. exhibited enhanced photocatalytic performance for the RhB degradation, which was ascribed to the charge transfer following a Z-scheme mechanism. Specifically, the photogenerated electrons in the CB of BiOBr would flow into metallic Ag through the Schottky barrier. Then the CB-electrons of BiOBr would transfer to the VB of AgBr and combine with the holes therein because the Fermi level of Ag is more positive than the VB potential of AgBr. Therefore, the photocatalytic degradation efficiency of RhB was greatly improved in the Ag/AgBr/BiOBr composites [45].

Besides, some organic photosensitizers can also be used as mediators, which not only transfer photogenerated electrons from PS II to PS I but also generate electrons under light irradiation. For example, Hagiwara et al. [46] investigated the electron transfer mechanism of tetraphenylporphyrin chromium chloride (Cr-TPPCl), a dye similar to porphyrin, during photolysis water reaction. The dye was supported on the surface of $KTa(Zr)O_3$ and then Pt was loaded on the other side of the dye. The results showed that photogenerated electrons transferred from the surface of $KTa(Zr)O_3$ to Pt through the Cr-TPPCl. Furthermore, nearly twenty different dyes such as vitamin B12 and tetrakis (pentafluorophenyl) porphyrin (TPFPP) were anchored on the surface of $KTa(Zr)O_3$ by Ishihara et al. [47]. All dyes were excited and electrons can be transferred to the Pt surface more efficiently, resulting in the yield of H_2 and O_2 that was about twenty times higher than $KTa(Zr)O_3$.

Although electron mediators play a significant role for the electrons transfer between PS II and PS I, there are several adverse effects. For example, colored electron transporters might interfere the light absorption of photocatalyst. In addition, noble-metal nanoparticles are not only expansive and rare but also strong light absorbers, which will greatly low the light absorption ability of photocatalysts [48]. Subsequently, the mediator-free Z-scheme photocatalytic system, which omits the process of carriers passing through the electron mediator, has attracted widespread concern since Wang et al. [49] constructed the first mediator-free all-solid-state Z-scheme photocatalytic system in 2009. Then Yu et al. [50] proposed the concept of a direct Z-scheme photocatalyst in 2013 to explain the excellent photocatalytic performance of the TiO_2/g-C_3N_4. Although the band structures of the direct Z-scheme photocatalytic system are very similar to Type- II heterostructures, the transfer paths of photogenerated charge carriers between two semiconductors is completely different. As shown in Fig. 5b, the CB-electrons of PS II with relatively low energy would combine with the VB-holes of PS I, thereby remaining the strongly reductive electrons in the CB of PS I and the strongly oxidative holes in the VB of PS II, respectively. Finally, the CB-electrons and VB-holes participate in the redox reaction occurred on the surface of catalysts. Obviously, compared with redox-mediator and all-solid-state Z-scheme photocatalytic systems, direct Z-scheme photocatalytic system with direct contact between two components can omit the process of carriers passing through the electron mediator, greatly lowing the possibility of recombination of bulk electrons and holes. Moreover, direct Z-scheme photocatalytic system can reduce the cost of constructing Z-scheme photocatalytic system

and also overcome the light-shielding effect caused by the noble-metal electron mediator, which has a promising future in the field of various applications.

In summary, many successful examples demonstrate that the construction of direct Z-scheme photocatalytic system has great potential for solving environment pollution and energy shortages, but there are still many challenges to overcome, such as how to improve light conversion efficiency and long-term stability of each semiconductor, how to optimize the contact interface of two components to maximize photocatalytic performance. It is difficult for a single-component semiconductor photocatalyst to solve the above key problems simultaneously, while the artificial Z-scheme photocatalytic system can do. Since the photocatalytic performance of redox-mediator Z-scheme photocatalytic system is limited by the backward reactions, light-shielding effect, long-distance electrons transfer and reaction environment, redox-mediator-free Z-scheme photocatalytic system that can shorten the electron transfer distance and can be used in liquid-phase and gas-phase environment is the optimal candidate in the application of water splitting, pollutants degradation as well as CO_2 conversion.

3. What contributions have the artificial Z-scheme photocatalytic system done on environmental restoration and energy conversion?

3.1. The photocatalytic degradation of organic pollutants

Rapid industrialization and urbanization have accelerated the generation of organic pollutants in the environment over the past decades such as organic synthetic dyes, pesticides, food additives and so on [51,52]. Survey data shows that the global annual production of organic synthetic dyes is up to 700,000 tons, of which 40% from the textile, paper, cosmetics, leather manufacturing and electronics manufacturing industries [53]. Organic dyestuff with stable physical and chemical properties is essentially complex aromatic compounds that are resistant to degradation. The direct discharge of colored pollutants to aquatic ecosystems poses a variety of threats to food chain and public health. Compared with the traditional oxidation technology [54,55], semiconductor photocatalysis provides a fixed reaction environment where adsorbed organic and inorganic species can be chemically altered by photo-induced redox reactions, which is a rapidly emerging advanced oxidation process for organic pollution abatement [56].

3.1.1. Basic principles of photodegradation

During photocatalysis, photogenerated electrons transfer to the surface of photocatalyst through the interfacial charge and then react with adsorbed O_2 molecules to generate $\cdot O_2^-$ [57]. VB-holes with strong oxidation ability can directly oxidize organic pollutants or react with hydroxide ions (OH^-) or H_2O to yield **.**OH. Those generated **.**OH and $\cdot O_2^-$ participate in the photodegradation of organic pollutants. Hydrogen substitution, electrophilic attack or electron transfer is considered to be three ways of photocatalytic degradation of organic pollutants by **.**OH, of which hydrogen abstraction is the most typical way [58]. As shown in Eq. (3.1) that hydrogen abstraction is the process of removing hydrogen atoms from the organic compound to form an organic radical through reacting with **.**OH. These peroxyl radicals completely mineralize organic compounds into CO_2, H_2O and inorganic salts (Eq. (3.2)) through a series of oxidation reactions [59]. During electrophilic attack, **.**OH is added to the π-system of organic compounds to form organic radical (Eq. (3.3)). Electron transfer is a viable route in the degradation of organic compounds when hydrogen abstraction or electrophilic addition are hindered by multiple halogen substitution or steric hindrance. As shown in Eq. (3.4) that **.**OH react with organic compounds to form hydroxide ions (OH^-) and organic radicals, and the subsequent reaction is the same as Eq. (3.2). Additionally, organic compounds can also be directly degraded by reacting with h^+ in the VB of semiconductor (Eq. (3.5)). Ultimately, organic pollutants can be degraded through the above routes.

$$\cdot OH + RH \rightarrow R\cdot + H_2O \quad (3.1)$$

$$R\cdot + O_2 \rightarrow RO_2\cdot \rightarrow H_2O + CO_2 + \text{Inorganic ions} \quad (3.2)$$

$$PHX + \cdot OH \rightarrow HOPHX\cdot \quad (3.3)$$

$$OH\cdot + RX \rightarrow RX\cdot + OH^- \quad (3.4)$$

$$\text{Pollutants} + h_{VB}^+ \rightarrow \text{Pollutants}^+ \rightarrow\rightarrow \text{Degradation products} \quad (3.5)$$

Dyes, a typical organic pollutant, are generally classified as cationic dyes and anionic dyes according to whether the chromogenic particles or molecules of dye molecules are positively charged or negatively charged in aqueous solution. Because the charging type of dye molecules mainly affects its adsorption process on the catalyst surface. Besides, the photocatalytic reactions are surface processes that occur on the surface of the catalyst. The dye molecules are first adsorbed on the surface of the catalyst and then participate in the oxidation reaction on the surface of the catalyst. Therefore, the type of dye molecules affects the efficiency of photocatalytic degradation and it should be considered when applying photocatalytic technology to treat dye wastewater.

3.1.2. Typical cationic dye degradation

Rhodamine B (RhB) is a synthetic water-soluble cationic dye. Toxicity tests have shown that irresistible damage may occur if animals or humans consume foods containing RhB. Hence, it is necessary to remove RhB in the environment through an efficient and environmentally-friendly photocatalytic technology, especially the Z-scheme photocatalyst that exhibits higher photodegradation efficiency compared with the type II heterojunction photocatalyst. The latest studies on RhB photocatalytic degradation based on the Z-scheme photocatalytic system are recorded in Table 1.

It is well known that the separation efficiency of electron-hole pairs directly influence the photocatalytic performance of the photocatalyst. The most prominent advantage of the Z-scheme photocatalytic system is to improve the charge separation efficiency. In 2006, Tada et al. [41] constructed the first all-solid-state Au@CdS/TiO_2 Z-scheme photocatalyst with Au as electrons mediator. In the most of Z-scheme photocatalytic systems, the noble metals are used as charge transmission bridge or recombination center of undesired electrons and holes, which efficiently promote the separation of electron-hole pairs. Therefore, it is a promising direction to modify semiconductor materials by coupling with noble metals to obtain excellent photocatalytic performance. For instance, Li and co-workers [67] prepared Ag/Ag_3PO_4/WO_3 composite to promote the separation efficiency of electron-hole pairs of pure WO_3. The UV–vis diffuse reflectance spectra (DRS) analysis showed that the combination of WO_3 causes the edges of light absorption to move towards longer wavelengths, indicating that the visible light response of composite was enhanced and more photogenerated electrons and holes were produced. Meanwhile, the absorption intensity in the visible light region was enhanced due to the reduced contact barrier and enhanced electronic coupling between WO_3 and Ag/Ag_3PO_4 nanoparticles. In Ag/Ag_3PO_4/WO_3 Z-scheme photocatalytic system, metallic Ag severs as charge transmission bridge. Specifically speaking, photogenerated electrons in the CB of WO_3 quickly transfer to Ag nanoparticles and recombine with the holes from the VB of Ag_3PO_4, thus the strongly reductive electrons are stored in the CB of Ag_3PO_4 and the strongly

Table 1
Photocatalytic degradation of RhB by Z-scheme photocatalysts in aqueous solution.

Photocatalysts	Initial concentration	Catalyst dose (g L^{-1})	Irradiation time (min)	Light source	Electron transfer	Photocatalytic activity	Ref.
g-C_3N_4/BiOBr/Au	10 mg L^{-1}	0.2	100	300 W high-pressure xenon lamp	All-solid-state Z-scheme	380 nm monochromatic light g-C_3N_4/BiOBr/Au-B: (4.51 h^{-1}) (3.8×> g-C_3N_4/BiOBr/Au-S) (1.18 h^{-1}) (5.8×> g-C_3N_4/BiOBr) (0.777 h^{-1}) 550 nm monochromatic light g-C_3N_4/BiOBr/Au-S (0.408 h^{-1}) (2.2×> g-C_3N_4/BiOBr/Au-B) (3.2×> g-C_3N_4/BiOBr) (0.129 h^{-1})	[60]
$BiVO_4$/Au@CdS	5 mg L^{-1}	0.6	60	300 W Xe lamp (λ > 420 nm)		$BiVO_4$/Au@CdS: 0.0138 min^{-1} (3.4×> $BiVO_4$/CdS/Au) (4.0×> $BiVO_4$/CdS) (5.8×> $BiVO_4$/Au) (19.7×> $BiVO_4$/Au)	[61]
AgI/Ag/I-$(BiO)_2CO_3$	10 mg L^{-1}	0.6	300	500 W Xe lamp (λ > 400 nm)		AgI/Ag/I-$(BiO)_2CO_3$: ~96.3% $(BiO)_2CO_3$: ~6.4% AgI/Ag: ~21.5% I-$(BiO)_2CO_3$: ~69.5% AgI/Ag/$(BiO)_2CO_3$: ~75.3%	[62]
Ag/AgCl/$_{(0\,4\,0)}$ $BiVO_4$	10 mg L^{-1}	2	35	λ ≥ 420 nm		Ag@AgCl/$BiVO_4$: ~100% (4×> Ag/$BiVO_4$; 300×> $BiVO_4$) $BiVO_4$: ~0.4% Ag/$BiVO_4$: ~42.4%	[63]
AgCl/Ag/$AgFeO_2$ (Cl: Fe = 3:1)	10 mg L^{-1}	0.5	60	300 W Xe lamp		AgCl/Ag/$AgFeO_2$: ~97.47% (0.05861 min^{-1}) (2.2×> AgCl; 10.8×> $AgFeO_2$) AgCl: 0.01319 min^{-1} $AgFeO_2$: 0.00136 min^{-1}	[64]
Ag/AgCl@MIL-53-Fe	10 mg L^{-1}	0.4	45	500 W Xe arc lamp (λ > 420 nm)		Ag/AgCl@MIL-53-Fe (Fe: Ag = 2:1): ~100% (0.107 min^{-1}) (21.4×~ bare MIL-53-Fe) MIL-53-Fe: ~20% (0.005 min^{-1})	[65]
Ag@AgBr/g-C_3N_4	10 mg L^{-1}	0.8	10	300 W Xe lamp (680 < λ < 710 nm)		Ag@AgBr/g-C_3N_4 (3:7): ~92% Ag@AgBr: ~82% g-C_3N_4: ~58%	[66]
Ag/Ag_3PO_4/WO_3	10 mg L^{-1}	1/3	20	300 W Xenon lamp (λ > 420 nm)		Ag_3PO_4/Ag/WO_3: ~100% (2.7×> Ag/Ag_3PO_4) (3.8×> pure Ag_3PO_4) (35×> WO_3)	[67]
g-C_3N_4@Ag@Ag_3PO_4	10 mg L^{-1}	1	60	laser-induced fluorescence spectroscopy with 405-nm laser		g-C_3N_4@Ag@Ag_3PO_4: ~94.8% (3.7×> g-C_3N_4) (2.85×> g-C_3N_4@Ag-12%) (3.7×> g-C_3N_4@Ag_3PO_4-1%)	[68]
Ag-C_3N_4/Bi_2WO_6	–	–	90	–		Ag-C_3N_4/Bi_2WO_6: ~100%	[69]
SnS_2-Ag_2O/Ag	10 mg L^{-1}	1	85	500 W Xenon lamp		SnS_2-Ag_2O/Ag-10: ~100% (0.0162 min^{-1}) (2×> pure SnS_2) SnS_2: ~60% (0.0075 min^{-1})	[70]
g-C_3N_4/RGO/Bi_2MoO_6	10 mg L^{-1}	1	60	500 W Xe lamp (λ < 420 nm)		g-C_3N_4/RGO/Bi_2MoO_6: 0.055 min^{-1} (8.73×> Bi_2MoO_6) (5.19×> g-C_3N_4/Bi_2MoO_6) Bi_2MoO_6: 0.0063 min^{-1} g-C_3N_4/Bi_2MoO_6: 0.0106 min^{-1}	[71]
TiO_2/SnS_2/RGO	5 mg L^{-1}	0.64	90	XG500 xenon long-arc lamp		TiO_2/SnS_2/RGO: ~100% pure TiO_2: ~42.0% TiO_2/RGO: ~87%	[72]
Ag_3PO_4/RGO/La,Cr:$SrTiO_3$	10 mg L^{-1}	1	10	300 W Xe lamp (λ > 420 nm)		(visible light irradiation) Ag_3PO_4/RGO/La,Cr:$SrTiO_3$: 0.79 min^{-1} Ag_3PO_4: 0.15 min^{-1} Ag_3PO_4/RGO: 0.50 min^{-1} (natural outdoor light) Ag_3PO_4/RGO/La,Cr:$SrTiO_3$: 0.65 min^{-1} Ag_3PO_4: 0.23 min^{-1} Ag_3PO_4/RGO: 0.52 min^{-1}	[73]

Table 1 (*continued*)

Photocatalysts	Initial concentration	Catalyst dose (g L^{-1})	Irradiation time (min)	Light source	Electron transfer	Photocatalytic activity	Ref.
g-C_3N_4/GO/AgBr	10 mg L^{-1}	0.5	30	250 W Xe lamp ($\lambda > 420$ nm)		g-C_3N_4/GO/AgBr-2: 0.1119 min^{-1} 17.5×~ P25 (0.0064 min^{-1}); 7.9×~ g-C_3N_4 (0.0141 min^{-1}); 3.5×~ AgBr (0.0323 min^{-1}); 4.0×~ g-C_3N_4/GO (0.0279 min^{-1}); 2.2×~ g-C_3N_4/AgBr (0.0519 min^{-1}).	[74]
Ag_2CrO_4/GO/g-C_3N_4	15 mg L^{-1}	0.2	60	300 W Xe lamp ($\lambda > 420$ nm)		GO/Ag_2CrO_4/g-C_3N_4: ~82.23% (2.73×> Ag_2CrO_4; 1.62×> g-C_3N_4) Ag_2CrO_4: ~46.16% g-C_3N_4: ~28.76%	[75]
Ag_3PO_4@$CuFe_2O_4$	10 mg L^{-1}	–	30	–		Ag_3PO_4@$CuFe_2O_4$: ~99% (0.1423 min^{-1})	[76]
g-C_3N_4/Ag_3PO_4	4×10^{-5} mol L^{-1}	0.8	75	500 W halogen lamp (420 < λ < 800 nm)	Direct Z-scheme	g-C_3N_4/Ag_3PO_4-20: ~ 99% (4.1×> b-g-C_3N_4/Ag_3PO_4-20) bulk-g-C_3N_4/Ag_3PO_4-20: ~ 65%	[77]
Ag_3PO_4/TiO_2-OV	20 mg L^{-1}	1	30	300 W Xe arc lamp ($\lambda > 400$ nm)		Ag_3PO_4/TiO_2-OV(1:5): 0.27 min^{-1} (90% in 16 min) (4.8×> Ag_3PO_4/TiO_2) Pure Ag_3PO_4: 90% in 26 min Ag_3PO_4/TiO_2: 0.056 min^{-1} (80% in 28 min)	[78]
$SnSe_2$/Ag_3PO_4	10 mg L^{-1}	0.2	50	300 W Xe lamp ($\lambda > 400$ nm)		Ag_3PO_4/$SnSe_2$-6 wt%: ~100% (4.2×> Ag_3PO_4; 26×> $SnSe_2$) Ag_3PO_4: ~58.7% $SnSe_2$: ~14.1%	[79]
Ag_3PO_4@MoS_2 quantum dot/MoS_2 nanosheet (ANP@MQD/FL-MNS)	10 mg L^{-1}	1	16	300 W Xenon lamp ($\lambda > 420$ nm)		ANP@MQD/FL-MNS-6: ~100% (0.2697 min^{-1}) (2.85×~pure Ag_3PO_4 NPs) pure Ag_3PO_4: ~80% (0.0945 min^{-1})	[80]
Fe_3O_4@MoS_2/Ag_3PO_4	20 mg L^{-1}	0.2	180	500 W Xe lamp equipped with a 420 nm (visible light); AM 1.5 (sunlight) cut-off filters		Fe_3O_4@MoS_2/Ag_3PO_4: ~98.90% (20×> Ag_3PO_4; 71×> MoS_2) (44×> MoS_2/Ag_3PO_4) pure Ag_3PO_4: ~ 64.6% MoS_2: ~63.1% Fe_3O_4@MoS_2: ~ 57.0%	[81]
Ag_3PO_4/ZnO-lO	5 mg L^{-1}		240	300 W xenon lamp		Ag_3PO_4/ZnO-lO: ~31.95% (1.4×> ZnO-lO) ZnO-lO: ~22.63%	[82]
Ag_2CO_3/ZnO	10 mg L^{-1}	1	10	500 W Xe lamp		Ag_2CO_3/ZnO: ~86.1% ZnO: ~44.6%	[83]
AgBr@Bi_2WO_6/WO_3	10 mg L^{-1}	1	80	400 W Xe lamp ($\lambda > 420$ nm)		40%-AgBr@Bi_2WO_6/WO_3: ~99% Bi_2WO_6/WO_3: ~57% AgBr: ~ 87%	[84]
AgBr/MoO_3	10 mg L^{-1}	0.2	60	250 W Xenon lamp ($\lambda > 420$ nm)		AgBr/MoO_3(1:3): ~95% (2×> AgBr)	[85]
AgCl/SmOCl	10 mg L^{-1}	–	40	500 W mercury lamp		AgCl/SmOCl : ~95% (0.04768 min^{-1}) (16×~ SmOCl) SmOCl: ~20% (0.00297 min^{-1})	[86]
AgI/Bi_5O_7I	10 mg L^{-1}	1	120	350 W Xe lamp with UV and IR filters		AgI/Bi_5O_7I : 0.046 min^{-1} (3.83×> Bi_5O_7I) (6.57×> AgI)	[87]
Bi_2O_3/g-C_3N_4	1.0×10^{-5}mol L^{-1}	1	60	500 W xenon lamp (4 7 0〉 λ > 400 nm)		Bi_2O_3/g-C_3N_4: ~45% (5.05×~ g-C_3N_4) g- C_3N_4: ~11.1%	[88]
Bi_2O_3/$NaNbO_3$	1.0×10^{-5}mol L^{-1}	2	40	375 W medium pressure mercury lamp (λ < 365 nm)		Bi_2O_3/$NaNbO_3$: ~91% (6.3×> $NaNbO_3$) pure $NaNbO_3$: ~32%	[89]
$KNbO_3$/Bi_2O_3	3.0×10^{-6}mol L^{-1}	1	30	375 W medium pressure mercury lamp (λ < 365 nm)		$KNbO_3$/Bi_2O_3: ~92.2% (0.0673 min^{-1}) (3.7×> pure Bi_2O_3) (6.9×> pure $KNbO_3$) pure Bi_2O_3: ~36.7% pure $KNbO_3$: ~20.4%	[90]

(*continued on next page*)

Table 1 (*continued*)

Photocatalysts	Initial concentration	Catalyst dose (g L^{-1})	Irradiation time (min)	Light source	Electron transfer	Photocatalytic activity	Ref.
g-C_3N_4/Bi_4O_7	1.0 × 10^{-5}mol L^{-1}	0.8	140	500 W halogen lamp (420 < λ < 800 nm)		g-C_3N_4/Bi_4O_7-30%: ~100%	[91]
Ag_2O/BiOF	10 mg L^{-1}	1	90(simulated solar) 120(visible light)	500 W Xe lamp (λ ≥ 420 nm)		Ag_2O/BiOF: ~67.5% (simulated solar) BiOF: ~29.5% Ag_2O/BiOF: ~36.7% (visible light) BiOF: ~14.7%	[92]
BiOBr/g-C_3N_4	1.0 × 10^{-5}mol L^{-1}	0.5	50	300 W Xe lamp (λ < 420 nm)		BiOBr/g-C_3N_4-80%: ~100% BiOBr: ~66.2% g-C_3N_4: ~91%	[93]
SnS_2/BiOBr	10 mg L^{-1}	0.625	30	400 W Xe lamp (λ > 420 nm)		SnS_2/BiOBr: ~88% (0.1203 min^{-1}) (75.1×> SnS_2; 2.2×> BiOBr) BiOBr: ~72%% (0.0545 min^{-1}) SnS_2: 0.0016 min^{-1}	[94]
BiOBr-Bi_2MoO_6	1.0 × 10^{-5}mol L^{-1}	0.2	30	300 W xenon lamp (λ > 470 nm)		BiOBr-Bi_2MoO_6 (9:1): ~95%, BiOBr: 38.36% (10×> BiOBr) Bi_2MoO_6: 15.21% (54.5×> Bi_2MoO_6)	[95]
Bi_2MoO_6/MO (M Cu, $Co_{3/4}$, or Ni)	10 mg L^{-1}	1	140	500 W Xe lamp (λ ≥ 420 nm)		Bi_2MoO_6/Co_3O_4-0.2 wt%: ~93% Bi_2MoO_6/NiO-0.2 wt%: ~66% Bi_2MoO_6: ~51%	[96]
Carbon nanodots/ WO_3 nanorods (CDots /WO_3)	10 mg L^{-1}	0.5	60	150 W Xenon lamp (λ > 780 nm) (7 8 0〉 λ > 420 nm)		CDots/WO_3: ~99.1% (7 8 0〉 λ > 420 nm) WO_3 nanorods : ~69.1% commercial WO_3: ~11.6% CDots/WO_3: ~61.2% (λ > 780 nm) WO_3 nanorods: ~0% commercial WO_3: ~0%	[97]
WO_3/$SnNb_2O_6$	10 mg L^{-1}	0.5	180	500 W tungsten lamp		WO_3/$SnNb_2O_6$: ~93.4% (4.7×> WO_3; 2×> $SnNb_2O_6$) WO_3: ~ 44.7% $SnNb_2O_6$: ~74.2%	[98]
CuS-WO_3	4 mg L^{-1}	0.5	150	500 W xenon lamp (λ > 420 nm)		CuS-WO_3: 96% (4.4×> WO_3; 9.2×> CuS) CuS: ~ 33% WO_3: ~ 49%	[99]
WO_3/g-C_3N_4	5 mg L^{-1}	0.6	20	500 W xenon lamp (λ > 420 nm)		WO_3/g-C_3N_4: ~100%	[100]
g-C_3N_4/Fe_2O_3	10 mg L^{-1}	0.8	20	300 W Xe lamp (λ > 400 nm)		Fe_2O_3/g-C_3N_4: >90% g-C_3N_4: < 20% γ-Fe_2O_3: < 20%	[101]
rTiO_2/g-C_3N_4(CNQDs)	5 mg L^{-1}	1	15	500 W Xenon lamp (λ > 420 nm)		15%–CN QDs-rTiO_2: 0.69 h^{-1} (7.8×> rTiO_2; 6.0×> g-C_3N_4) rTiO_2: 0.089 h^{-1} g-C_3N_4: 0.12 h^{-1}	[102]
g-C_3N_4/$BiOIO_3$	20 mg L^{-1}	1	25	300 W Xe arc lamp (λ > 420 nm)		g-C_3N_4/$BiOIO_3$ > g-C_3N_4	[103]
N-$K_2Ti_4O_9$/g-C_3N_4/UiO-66	10 mg L^{-1}	0.2	180	PHILIPS 70 W metal halide lamp (λ < 380 nm)		N-$K_2Ti_4O_9$/g-C_3N_4/UiO-66: ~90% (2.4×> N-$K_2Ti_4O_9$) (3×~ g-C_3N_4) (1.2×> UiO-66)	[104]
SnO_{2-x}/g-C_3N_4	10 mg L^{-1}	1	50	350 W Xe lamp equipped with a UV cut and an IR cut filters (800 > λ > 420 nm). Other filters (λ > 320 nm, λ > 360 nm, λ > 480 nm, λ > 580 nm)		SnO_{2-x}/g-C_3N_4: (0.088 min^{-1}) (8.8 × pure g-C_3N_4) pure g-C_3N_4: 0.001 min^{-1} SnO_{2-x}: 0.001 min^{-1}	[105]
Pg-C_3N_4/Ag_2CrO_4	10 mg L^{-1}	1	90	300 W Xe lamp (λ ≥ 420 nm)		Ag_2CrO_4/g-C_3N_4: 99.2% (5.542 min^{-1}) (6.1×> Ag_2CrO_4) (9.7×> g-C_3N_4)	[106]
Cr-$SrTiO_3$/g-C_3N_4	5 mg L^{-1}	0.33	30	500 W xenon lamp (λ < 420 nm)		Cr-$SrTiO_3$/g-C_3N_4-70%: ~97% (4.5×> g-C_3N_4; 3.5×> Cr-$SrTiO_3$) g-C_3N_4: ~47% Cr-$SrTiO_3$: ~57%	[107]
Bi_2WO_6 QDs/g-C_3N_4	10 mg L^{-1}	1	50	300 W Xe lamp (λ > 420 nm)		Bi_2WO_6/g-C_3N_4: ~100% (0.168 min^{-1}) (10×> Bi_2WO_6 QDs) Bi_2WO_6 QDs: ~60% (0.0157 min^{-1})	[108]

oxidative holes are retained in the VB of WO_3, respectively. The holes could directly oxidize dye molecules or react with H_2O or OH^- to generate **.**OH, the electrons cannot reduce dissolves O_2 to $\cdot O_2^-$, but can react with O_2 to generated **.**OH, those active species and oxidative holes participate in the photodegradation of dye molecules. In this process, the efficient separation of photogenerated electron-hole pairs enables optimal photocatalytic performance.

More recently, metal-organic frameworks (MOFs) with a large amount of porosity and large specific surface area, where metal ions or clusters are linked to organic linkers forming a three-dimensional well-defined structure, have attracted much attention in industrial applications and academic research [109]. Photosensitive MOFs interact with incident light and show semiconducting properties, which can drive a variety of chemically desirable photo-redox reactions. An iron terephthalate metal-organic framework MIL-53 (Fe) with iron (III) oxide clusters shows inherent visible light absorption and can be used as an effective photocatalyst. However, the visible light photocatalytic performance of pure MIL-53 (Fe) is not satisfactory due to the small number of active radicals. Therefore, Liu et al. [65] synthesized Ag/AgCl@MIL-53-Fe photocatalysts by coupling MIL-53-Fe with plasmonic Ag/AgCl to enhance the photocatalytic performance of MIL-53-Fe. DRS images show that the absorption intensity of Ag/AgCl@MIL-53-Fe in the range of 300–600 nm is greatly enhanced after introduction of plasmonic Ag/AgCl, due to the SPR absorption of Ag nanoparticles at wavelength above 400 nm and the excitation of AgCl at wavelength below 400 nm. Additionally, Ag/AgCl can also promote the separation of photogenerated electron-hole pairs. In general, the AgCl cannot be excited under visible light irradiation owing to its large band gap, while metallic Ag can be excited due to its SPR effects. The SPR-excited electrons are transferred to AgCl through Schottky barrier formed between Ag and AgCl. Simultaneously, MIL-53-Fe is excited under visible light irradiation and generates photogenerated electrons and holes. As show in Fig. 6, the photogenerated electrons in the CB of MIL-53-Fe would transfer to Ag particles and combine with its positive charge species, resulting in the accumulation of holes in the VB of MIL-53-Fe. The stored photogenerated holes can directly oxidize target pollutants. What's more, the large surface area and intrinsic porosity of MOFs provide open channels for efficient reactant diffusion, which also facilitate the improvement of photocatalytic performance. Li et al. [78] loaded the uniform and ultrafine Ag_3PO_4 nanoparticles on the oxygen vacated TiO_2 (TiO_2-OV) with average particle size as small as 2.6 nm to fabricated Ag_3PO_4/TiO_2-OV photocatalysts. These zero dimensional defects with relatively free movable electrons formed by removing some oxygen atoms from TiO_2 crystalline can strongly absorb Ag^+ ions. Most of the electrons are neutralized by Ag^+ cations, while small amount of electrons will reduce Ag^+ to Ag nanoparticles that serve as the charge transfer bridge. In the photocatalytic process, the electrons in the CB of Ag_3PO_4 migrate to Ag nanoparticles since the CB potential of Ag_3PO_4 is more negative than the Fermi level of Ag, and at the same time, the holes in the VB of TiO_2-OV transfer to the Ag nanoparticles and combine with the electrons from Ag_3PO_4, which greatly promotes the separation of electron-hole pairs, thus improving the photocatalytic performance of Ag_3PO_4/TiO_2-OV (Fig. 7).

In addition, due to the large specific surface area and high stability of graphene oxide (GO) or reduced graphene (RGO), which also makes them to be an electron mediators in all-solid-state Z-scheme photocatalytic system. For example, Chong et al. [69] synthesized $Ag/g\text{-}C_3N_4/Bi_2WO_6$ with RGO as electron mediator through a facile hydrothermal synthesis method. Scanning electron microscope (SEM) and transmission electron microscope (TEM) analyzes indicate that Ag^+ ions were successfully reduced and deposited on the surface of $g\text{-}C_3N_4/Bi_2WO_6$ composites. The $Ag/g\text{-}C_3N_4/Bi_2WO_6$ composites exhibit higher photodegradation efficiency than pure $g\text{-}C_3N_4$ and single Bi_2WO_6. This enhanced photocatalytic performance is ascribed to the photogenerated electron-hole pairs following the Z-scheme transfer mechanism. Here, metallic Ag severs as the center of charge recombination, the relative weak oxidative holes and the relative weak reductive electrons are annihilated on Ag nanoparticles, resulting in the accumulation of strongly reductive electrons in the CB of $g\text{-}C_3N_4$ and strongly oxidative holes in the VB of Bi_2WO_6, respectively. The photogenerated electrons reduce O_2 to $\cdot O_2^-$ and holes react with H_2O to produce **.**OH. Accordingly, the stored holes and formed **.**OH and $\cdot O_2^-$ can oxidize target pollutants to achieve an excellent photocatalytic performance.

Moreover, the absorption efficiency of visible light is another important factor affecting the photocatalytic performance of photocatalysts. Among various methods, ion doping is an excellent method to increase visible light absorption by forming impurity levels in the band structure. For instance, Liang et al. [62] fabricated a novel double Z-scheme AgI/Ag/I-$(BiO)_2CO_3$ composite photocatalysts through ion-exchange method and evaluated their photocatalytic performance for RhB photodegradation. The Mott-Schottky curves indicates that the valance band potential of $(BiO)_2CO_3$ is reduced from 3.05 eV to 2.45 eV of I-$(BiO)_2CO_3$ after doping I^- ion and the band gap of $(BiO)_2CO_3$ is narrowed from 3.21 eV to 2.61 eV, which allows I-$(BiO)_2CO_3$ to be excited under visible light irradiation. Additionally, the metallic Ag severs as the electrons transfer bridge, the CB-electrons of I-$(BiO)_2CO_3$ transfer to the VB of AgI and combine with the holes therein. As a result,

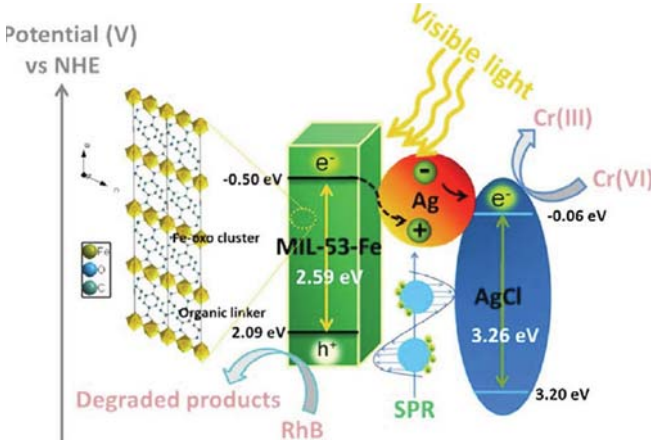

Fig. 6. Plasmonic Z-scheme photocatalytic mechanism of Ag/AgCl@MIL-53-Fe under visible light irradiation. Adapted and reprinted with permission from Ref. [65], Copyright 2017 Elsevier.

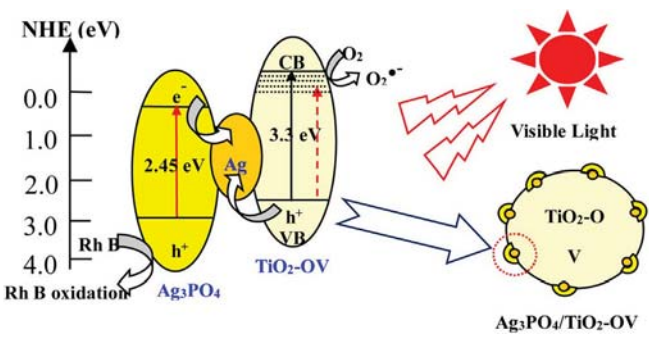

Fig. 7. Proposed Z-scheme mechanism for photocatalytic degradation in Ag3PO 4/Ag/TiO 2-OV catalyst under visible light irradiation. Adapted and reprinted with permission from Ref. [78], Copyright 2016 Elsevier.

the photogenerated stored in the CB of AgI could reduce absorbed O_2 to $\cdot O_2^-$, both $\cdot O_2^-$ and VB-holes of I-$(BiO)_2CO_3$ with strong oxidizing ability can oxidize the RhB molecule.

Feng et al. [85] constructed a novel direct Z-scheme nanocomposite AgBr/MoO_3 via an oriented diffusing and charge induced deposition. The AgBr/MoO_3 composite with 1:3 mole ratio of Ag to Mo exhibited the best photocatalytic performance. This enhanced photocatalytic performance is attributed to three aspects: Firstly, according to the calculation of plane-wave-density function (DFT), the band gap of the AgBr/MoO_3 (1.378 eV) is much smaller than those of single MoO_3 (2.087 eV) and AgBr (1.661 eV), which is caused by the hybridization between the Br 4p orbital and O 2p orbital in AgBr/MoO_3, thus promoting the visible-light absorption. Next, the highly dispersed VB and CB of AgBr facilitate the excitation and migration of charge carrier. Also, the Ohmic contact formed in the contact surface between AgBr and MoO_3 serves as the center of photogenerated electron-hole recombination, thus remaining the photogenerated electrons with a more negative reduction potential in the CB of AgBr and holes with a more positive oxidation potential in the VB of MoO_3, respectively. This efficient separation of electron-hole pairs greatly improve the photocatalytic performance of AgBr/MoO_3.

Methyl blue (MB), another common cationic dye, poses a threat to the human health and the environment. The studies of the Z-scheme nanocomposites towards the photodegradation of MB over the past several years are listed in Table 2. Similar to RhB, MB can also be effectively photodegraded under different experimental conditions.

Graphene, a monolayer of graphite, has been an effective co-catalyst due to its high specific surface area and excellent electron mobility [137]. Graphitic carbon nitride (g-C_3N_4) with a narrow band gap and a relative more negative reduction potential has gotten appreciable attention recently and is widely used to degrade organic pollutants since it was first employed as photocatalyst to split water in 2009 [138]. However, the oxidation ability of g-C_3N_4 is poor owing to its undesirable VB potential of 1.4 eV, resulting in a fast recombination of photogenerated electron-hole pairs. Hence, various g-C_3N_4-based Z-scheme composite photocatalysts are designed to promote the charge separation of pure g-C_3N_4. For instance, Wu et al. [111] reported the synthesis of the all-solid-state Z-scheme g-C_3N_4-RGO-TiO_2 heterojunctions with excellent photocatalytic performance and stability for the photodegradation of MB under the visible light irradiation. UV–vis absorption spectra indicates that the absorption edges of g-C_3N_4-RGO-TiO_2 show obvious red-shift to higher wavelengths, while RGO-TiO_2 show blue-shift to lower wavelengths, which demonstrates that the introduction of RGO increases the light absorption efficiency of g-C_3N_4-RGO-TiO_2 composites. Also, the strong interaction formed between g-C_3N_4-TiO_2 and RGO narrows the band gap of g-C_3N_4-RGO-TiO_2, further improving the visible light absorption. Furthermore, the charge separation mechanism of all-solid-state Z-scheme is verified by the photoluminescence (PL) spectra and the trapping experiment. Here, the prolong lifetime of charge carriers result in generating more active oxidizing species such as $\cdot O_2^-$ and $\cdot$OH, thus achieving an enhanced photocatalytic performance in g-C_3N_4-RGO-TiO_2. Chen et al. [75] constructed GO/Ag_2CrO_4/g-C_3N_4 nanocomposite by one-step chemical precipitation method and also discussed the photodegradation performance of MB under visible light irradiation. DRS image indicates that the absorption intensity in visible light region of g-C_3N_4/Ag_2CrO_4 is obvious enhanced after introducing GO since GO can suppress the reflection of light. Additionally, GO severs as the bridge between g-C_3N_4 and Ag_2CrO_4 and involves in electrical conduction, which is beneficial to the separation of photogenerated electrons and holes. Besides, the introduction of GO and g-C_3N_4 greatly suppress the photo-corrosion of Ag_2CrO_4, improving the photostability of composites. Finally, a double Z-scheme transfer also facilitate the enhancement of photocatalytic performance. Here, the photogenerated electrons in the CB of Ag_2CrO_4 would migrate to the metallic Ag owing to the CB potential of Ag_2CrO_4 is more negative than the Fermi level of Ag. At the same time, the holes in the VB of GO and g-C_3N_4 shift to Ag nanoparticles and combine with the electrons. Hence, the remained holes with more positive oxidation potential directly oxidize the pollutants or oxidize OH^- to $\cdot$OH, while the electrons left in the CB of GO and g-C_3N_4 reduce absorbed O_2 to $\cdot O_2^-$. Those active species formed in the photocatalytic process could decompose the pollutants into smaller molecules or directly transformed into CO_2 and H_2O.

Although many advantages of g-C_3N_4 endow it an excellent photocatalytic performance, the amount of photocatalytic active sites in g-C_3N_4 nanosheets is still restricted due to its limited boundaries and exposed edges. In order to solve this problem, the g-C_3N_4 nanosheets can be made into porous g-C_3N_4 (Pg-C_3N_4) by morphological changes, which can not only increase the surface area, but also expose more active sites, finally improving the separation of photogenerated electrons and holes. For instance, Shang et al. [106] used microemulsion-assisted co-precipitation route to prepare Pg-C_3N_4/Ag_2CrO_4 composites and evaluated the photocatalytic activity of Pg-C_3N_4/Ag_2CrO_4 with different content of Ag_2CrO_4. The high resolution X-ray photoelectron spectra (HRXPS) spectra of Ag 3d demonstrated that part of Ag_2CrO_4 was reduced to Ag^0, which acted as the bridge of electron transfer during the reaction process. Additionally, g-C_3N_4 severed as an electron acceptor can accept the electrons from the CB of Ag_2CrO_4 and combine with the holes therein, resulting in the electrons with more negative potential store in the CB of g-C_3N_4. This process not only facilitate the separation of electron-holes pairs, but also greatly inhibit the photo-corrosion of Ag_2CrO_4. Zhang et al. [125] reported that the kinetic constant of MB degradation over Pg-C_3N_4/Ag_3PO_4 was 9.6 and 1.45 times as high as that of Pg-C_3N_4 and Ag_3PO_4, respectively. This enhanced photocatalytic performance is mainly attributed to the fact that Pg-C_3N_4 nanosheets with many active edges and diffusion channels can greatly accelerate the mass transfer and diffusion of photo-generated carriers. Additionally, the electrons migration between Pg-C_3N_4 and Ag_3PO_4 with Z-scheme mechanism is also contribute to the improvement of the photocatalytic performance.

GO, another derivative of graphene, retains the layer structure of graphene and has strong hydrophilic property due to the presence of abundant oxygen-containing functional groups. These properties make it a favorable support to fabricate various GO-involved hybrid photocatalysts. For instance, Xu et al. [124] prepared direct Z-scheme Ag_2CrO_4-GO composite photocatalysts via a simple precipitation method. Ag_2CrO_4-GO with 1.0 wt% GO content exhibited the highest photocatalytic activity and stability towards MB degradation, owing to the fast transfer of electrons from Ag_2CrO_4 to GO sheets followed the Z-scheme mechanism. The CB level of Ag_2CrO_4 is 0.47 V, which is less negative than the $\cdot O_2^-/O_2$ potential (−0.28 V), so it is difficult to generate $\cdot O_2^-$. However, the reactive specie trapping experiments proved that $\cdot O_2^-$ was the main active specie. Hence, a Z-scheme mechanism of electron transfer in Ag_2CrO_4-GO can explain the excellent photocatalytic performance. The electrons in the CB of Ag_2CrO_4 would transfer and recombine with the holes in the VB of GO. The remaining holes in the VB of Ag_2CrO_4 directly oxidize MB and electrons in the CB of GO reduce the absorbed O_2 into $\cdot O_2^-$. Liu et al. [132] coupled TiO_2 with Bi_2S_3 to form Bi_2S_3 sensitized TiO_2 nanoparticles and then introduce graphene to form ternary Bi_2S_3/RGO/TiO_2 composite photocatalyst. Nearly 97.8%MB was photodegraded by Bi_2S_3/RGO/TiO_2 within 90 min, whereas nano-TiO_2 just degrade 27.5% under the same condition. This excellent photocatalytic performance is ascribed to three aspects: (1) Bi_2S_3/RGO/TiO_2 showed

Table 2
Photocatalytic degradation of MB based on Z-scheme photocatalyst in aqueous solution.

Photocatalyst	Initial concentration	Catalyst dose (g L^{-1})	Irradiation time (min)	Light source	Electron transfer	Photocatalytic activity	Ref.
CdS-Au-TiO_2 hollow nanorod arrays (CdS-Au-THNAs)	10 mg L^{-1}	–	120	20 W low-pressure mercury lamp	All-solid-state Z-scheme	CdS-Au-THNAs: ~72% CdS-THNAs: ~25% Au-THNAs: ~35% pure THNAs: ~15%	[110]
g-C_3N_4-RGO-TiO_2	30 mg L^{-1}	0.25	180	300 W Xe lamp ($\lambda > 420$ nm)		G-C_3N_4-RGO-TiO_2: ~92% (0.0137 min^{-1}) (4.7×> g-C_3N_4; 3.2×> g-C_3N_4-TiO_2) g-C_3N_4: ~39% (0.0029 min^{-1}) g-C_3N_4-TiO_2: ~53% (0.0043 min^{-1})	[111]
RGO-Fe_2O_3-MoS_2	10 mg L^{-1}	0.1	50	350 W Xe lamp ($\lambda > 400$ nm)		RGO-Fe_2O_3-MoS_2: ~98% (0.045 min^{-1}) (5.6×~ Fe_2O_3;1.8×~ RGO-Fe_2O_3) (3.7×~ RGO-MoS_2) Fe_2O_3: 0.008 min^{-1} RGO-Fe_2O_3: 0.025 min^{-1} RGO-MoS_2: 0.012 min^{-1}	[112]
Cu_2O/graphene/α-Fe_2O_3 (Cu_2O/G/FNA)	20 mg L^{-1}	–	60	xenon lamp ($\lambda \geq 400$ nm)		Cu_2O/G/FNA: ~86.2%	[113]
Ag_2CrO_4/GO/g-C_3N_4	15 mg L^{-1}	0.2	60	300 W Xe lamp ($\lambda > 420$ nm)		GO/Ag_2CrO_4/g-C_3N_4: ~92.69% (0.04329 min^{-1}) (1.62×> Ag_2CrO_4; 2.26×> g-C_3N_4) Ag_2CrO_4: ~79.52% g-C_3N_4: ~70.58%	[75]
Ag_2CO_3/Ag/AgCl	10 mg L^{-1}	0.5	15	300 W xenon lamp ($\lambda > 400$ nm)		Ag_2CO_3/Ag/AgCl: ~100% (0.23 min^{-1}) (7.6×> Ag_2CO_3; 2×> Ag/AgCl) (11×> Ag_2CO_3/AgCl) Ag_2CO_3: ~53% (0.03 min^{-1}) Ag/AgCl: ~81% (0.11 min^{-1}) Ag_2CO_3/AgCl: ~42% (0.02 min^{-1})	[114]
Ag_2SO_3/AgBr	20 mg L^{-1}	0.625	18	500 W xenon lamp ($\lambda > 420$ nm)		GO/Ag_2SO_3/AgBr: ~ 99.9% (9 min) Ag_2SO_3/AgBr: ~99.9% (12 min) Ag_2SO_3: ~55% (18 min) AgBr: ~88% (18 min)	[115]
Ag_3PO_4/Ag_2MoO_4	1.0×10^{-5}mol L^{-1}	0.4	5	350 W Xe lamp ($\lambda > 420$ nm)		Ag_2MoO_4/Ag_3PO_4: ~97%	[116]
3DOM-$SrTiO_3$/Ag/Ag_3PO_4	2.0×10^{-5}mol L^{-1}	0.25	12	300 W Xe lamp ($\lambda > 420$ nm)		$SrTiO_3$/Ag/Ag_3PO_4: ~100% (0.32 min^{-1})	[117]
$SrTiO_3$(La, Cr)/WO_3	15 mg L^{-1}	0.3	120	300 W Xe lamp ($\lambda > 420$ nm)	Direct Z-scheme	$SrTiO_3$(La, Cr)/WO_3: 0.0069 min^{-1} (1.8×~ WO_3; 1.7×> $SrTiO_3$(La, Cr)) WO_3: ~30% (0.0038 min^{-1}) $SrTiO_3$(La, Cr): ~ 37% (0.0040 min^{-1})	[118]
WO_3/g-C_3N_4	0.9×10^{-5} mol L^{-1}	2.0	60	500 W Xenon lamp (4 7 0〉 λ >400 nm)		WO_3/g-C_3N_4: 87.9% (0.0353 min^{-1}) (4.77×~ pure g-C_3N_4) g-C_3N_4: 35.6% (0.0074 min^{-1})	[119]
WO_3/g-C_3N_4	50 mg L^{-1}	0.5	90	300 W Xe lamp ($\lambda > 400$ nm)		30 wt%-WO_3/g-C_3N_4: ~95% (0.01897 min^{-1}) (2.5×> g-C_3N_4; 2.7×> WO_3) g-C_3N_4: 0.00763 min^{-1} WO_3: 0.00694 min^{-1}	[120]
Ag_3PO_4/MoS_2	10 mg L^{-1}	1.0	60	35 W Xe arc lamp ($\lambda > 420$ nm)		Ag_3PO_4/MoS_2-15: ~98.2% (0.06548 min^{-1}) (1.28×> Ag_3PO_4; 16.37×> MoS_2) MoS_2: ~20.3% (0.004 min^{-1}) Ag_3PO_4: ~94.8% (0.05117 min^{-1})	[121]
Cu_2O/Ag_3PO_4	10 mg L^{-1}	0.5	8	300 W Xe lamp ($\lambda > 420$ nm)		Cu_2O/Ag_3PO_4: ~90% (0.30447 min^{-1}) (7.0×~ Cu_2O; 2.1×~ Ag_3PO_4) Cu_2O: 0.04349 min^{-1} Ag_3PO_4: 0.14331 min^{-1}	[122]
Ag_2CO_3/SiC	0.78×10^{-5}mol L^{-1}	1.0	90	natural sunlight		Ag_2CO_3/SiC-12 wt%: ~98% formal quantum efficiency (FQE): 0.154% TiO_2: ~90%	[123]
Ag_2CrO_4-GO	1.0×10^{-5}mol L^{-1}	0.2	15	300 W Xe arc lamp ($\lambda \geq 400$ nm)		Ag_2CrO_4/GO-1.0 wt%: ~100% (0.28 min^{-1}) (3.5×~ Ag_2CrO_4; 14×> N-TiO_2) N-TiO_2: ~20% Ag_2CrO_4: ~70%	[124]

(*continued on next page*)

Table 2 (*continued*)

Photocatalyst	Initial concentration	Catalyst dose (g L^{-1})	Irradiation time (min)	Light source	Electron transfer	Photocatalytic activity	Ref.
Pg-C_3N_4/Ag_2CrO_4	10 mg L^{-1}	0.67	120	300 W Xe lamp ($\lambda \geq 420$ nm)		Ag_2CrO_4/g-C_3N_4: ~99.1% ($3.727\ min^{-1}$) ($7.9\times$>Ag_2CrO_4; $15.2\times$>g-C_3N_4) Ag_2CrO_4: $0.245\ min^{-1}$ g-C_3N_4: $0.473\ min^{-1}$	[106]
Pg-C_3N_4/Ag_3PO_4	10 mg L^{-1}	0.5	10	300 W Xe lamp ($\lambda > 420$ nm)		Pg-C_3N_4/Ag_3PO_4: ~96% ($0.33945\ min^{-1}$) ($1.45\times\sim$ Ag_3PO_4; $9.6\times\sim$ Pg-C_3N_4) pure Pg-C_3N_4: ~26% Ag_3PO_4: ~85%	[125]
Pg-C_3N_4/BiOBr	10 mg L^{-1}	1.0	40	50 W 410 nm LED light		Pg-C_3N_4/BiOBr: ~90% ($0.088\ min^{-1}$) ($3.7\times$> Pg-C_3N_4; $4.2\times$> BiOBr) ($7.3\times$> g-C_3N_4) pure g-C_3N_4: ~40% ($0.012\ min^{-1}$) pure BiOBr: ~50% ($0.021\ min^{-1}$) pure Pg-C_3N_4: ~60%($0.024\ min^{-1}$)	[126]
$BiVO_4$/Pg-C_3N_4	20 mg L^{-1}	1.0	60	50 W 410 nm LED light		$BiVO_4$/Pg-C_3N_4 : ~100% ($0.05251\ min^{-1}$) ($4.6\times$> $BiVO_4$; $7.2\times$> Pg-C_3N_4) $BiVO_4$: $0.00938\ min^{-1}$ Pg-C_3N_4: $0.00643\ min^{-1}$	[127]
N-ZnO/$BiVO_4$	1.0×10^{-5}mol L^{-1}	0.05	60	AM 1.5 solar illumination at 100 mW·cm^{-2}		N-ZnO/$BiVO_4$: ~77% ($0.022\ min^{-1}$) ($1.76\times\sim$ pure ZnO) pure ZnO: ~39% pure $BiVO_4$: ~27% N-ZnO: ~45%	[128]
g-C_3N_4/Bi_2MoO_6	10 mg L^{-1}	1.0	40	50 W LED light		g-C_3N_4/Bi_2MoO_6:~90% ($0.0688\ min^{-1}$) ($4.8\times\sim$ g-C_3N_4; $8.2\times\sim$ Bi_2MoO_6) Bi_2MoO_6: ~30% ($0.0084\ min^{-1}$) g-C_3N_4: ~40% ($0.0143\ min^{-1}$)	[129]
Bi_2MoO_6/Ag_3PO_4	8 mg L^{-1}	1.0	1.5	50 W 410 nm LED		Bi_2MoO_6/Ag_3PO_4: ~96.8% ($0.04\ s^{-1}$) ($4.3\times\sim$ Ag_3PO_4; $7.9\times$> Bi_2MoO_6) Bi_2MoO_6: ~35% Ag_3PO_4: ~56.7%	[130]
$Bi_2Sn_2O_7$/g-C_3N_4	10 mg L^{-1}	1.0	180	300 W Xe arc lamp ($\lambda > 420$ nm)		$Bi_2Sn_2O_7$/g-C_3N_4:~94.7% ($0.9107\ h^{-1}$) $Bi_2Sn_2O_7$: ~ 61.35% g-C_3N_4 : ~ 40.56%	[131]
Bi_2O_3/g-C_3N_4	1.0×10^{-5}mol L^{-1}	1.0	60	500 W xenon lamp ($4\ 7\ 0\rangle\ \lambda > 400$ nm)		Bi_2O_3/g-C_3N_4: $0.0253\ min^{-1}$ ($3.42\times\sim$ pure g-C_3N_4) g-C_3N_4: $0.0074\ min^{-1}$	[88]
g-C_3N_4/Bi_4O_7	5 mg L^{-1}	0.8	90	500 W halogen lamp ($420 < \lambda < 80$ nm)		g-C_3N_4/Bi_4O_7: ~93% ($10.1\times$> g-C_3N_4; $2.5\times$> Bi_4O_7) g-C_3N_4: ~15% pure Bi_4O_7: ~78%	[91]
Bi_2S_3/TiO_2/RGO	10 mg L^{-1}	0.4	90	400 W Xe lamp ($8\ 0\ 0\rangle\ \lambda > 380$ nm)		Bi_2S_3/TiO_2/RGO: ~ 97.8% nano-TiO_2: ~27.5% Bi_2S_3, Bi_2S_3/RGO: almost have no degradation ability	[132]
CdS/$CoWO_4$ (CdS: $CoWO_4$ = 3:5)	10 mg L^{-1}	1.0	60	250 W Xe lamp ($\lambda > 420$ nm)		CdS/$CoWO_4$: ~83% ($3\times$> CdS; $8\times$> $CoWO_4$) CdS: ~30%	[133]
CeO_2/Ce_2O_3	10 mg L^{-1}	0.5	120	Nd: YAG Laser light		CeO_2/Ce_2O_3: ~24% ($2.16 \times 10^{-3}\ min^{-1}$) ($1.5\times$> CeO_2) CeO_2: ~15% ($1.46 \times 10^{-3}\ min^{-1}$)	[134]
hematite ore/g-C_3N_4 (LW/g-C_3N_4)	–	–	60	300 W simulated solar light lamp ($\lambda > 420$ nm)		g-C_3N_4/LW: ~97% ($0.057\ min^{-1}$) ($5.2\times\sim$ LW; 11.4 × g-C_3N_4; $1.5\times$>TiO_2) pure natural LW: $0.011\ min^{-1}$ g-C_3N_4: $0.005\ min^{-1}$	[135]
$Zn_3(VO_4)_2$ porous nanoflower/g-C_3N_4 nanosheet (ZV-CN)	10 mg L^{-1}	1.0	300	250 W Xenon lamp		ZV-CN: ~95.45% ($0.62\ h^{-1}$) ($6.6\times$> $Zn_3(VO_4)_2$; $3.6\times$> g-C_3N_4) $Zn_3(VO_4)_2$-CN: ~66.26% g-C_3N_4: ~57.66% $Zn_3(VO_4)_2$: ~36.71%	[136]

enhanced absorption capabilities and wider visible region after coupling Bi_2S_3 and RGO; (2) SEM and TEM images proved that part of Bi_2S_3/TiO_2 were uniformly dispersed on the GO, resulting in less agglomeration; (3) the introduction of graphene facilitate the separation of electrons and holes.

The photocatalytic performance towards the photodegradation of MB by $GO/Ag_2SO_3/AgBr$ was evaluated under visible light [115]. BET specific surface areas (S_{BET}) measurement indicate that the introduction of GO and AgBr greatly increase the S_{BET} of Ag_2SO_3, thus increasing the absorption of dye molecules. For $Ag_2SO_3/AgBr$, the photogenerated electrons in the CB of AgBr migrate to the metallic Ag owing to its more negative potential. Meanwhile, due to the SPR effect and dipolar character of Ag, the absorbed photons are separated to holes and electrons. The photogenerated electrons migrated from the CB of AgBr combine with the holes in the highest occupied orbital of Ag. At the same time, the electrons in the lowest unoccupied orbital of Ag transfer to the CB of Ag_2SO_3, which result in the generation of electron-hole pairs in the Ag_2SO_3 by dipolar-dipolar interaction. While for $GO/Ag_2SO_3/AgBr$, both the photogenerated electrons in the CB of Ag_2SO_3 and on metallic Ag transfer to GO sheets, further promoting the separation efficiency of electrons and holes and suppress the reduction of Ag^+ ions. The electrons on the surface of GO could reduce GO to rGO or react with the absorbed O_2 to produce $\cdot O_2^-$.

In addition to g-C_3N_4-based composites, strontium titanate ($SrTiO_3$) with low toxicity, excellent stability, structural flexibility and high photocatalytic performance is widely applied in the field of photocatalysis. Zhang et al. [117] successfully prepared 3DOM-$SrTiO_3/Ag/Ag_3PO_4$ samples with different molar ratio of $SrTiO_3$ to Ag_3PO_4 through a deposition-precipitation route. The results show that almost all MB are degraded by 3DOM-$SrTiO_3/Ag/Ag_3PO_4$ with 35:65 molar ratio of 3DOM-$SrTiO_3$ to Ag_3PO_4 and 300 nm pore diameter within 12 min, owing to the photo-corrosion of Ag_3PO_4 being inhibited by forming the Z-scheme system between 3DOM-$SrTiO_3$ and Ag_3PO_4. Liu et al. [118] fabricated a direct Z-scheme composites $WO_3/SrTiO_3$ (La, Cr). Noteworthy, $WO_3/SrTiO_3$ (La, Cr) with 90 wt% $SrTiO_3$ (La, Cr) possessed the optimal photocatalytic performance, which can photodegrade about 70% MB within 120 min. This enhancement of photocatalytic performance is attributed to the effective separation of photogenerated electrons and holes via forming a close-contact heterojunction interface between WO_3 and $SrTiO_3$ (La, Cr). WO_3 with much negative zeta potential strongly attract MB molecules and $SrTiO_3$ (La, Cr) can provide a large surface area. Additionally, the electrons in the CB of WO_3 will shift to the VB of $SrTiO_3$ (La, Cr) and combine with the holes therein, thus promoting the separation of photogenerated electrons in the CB of $SrTiO_3$ (La, Cr) and holes in the VB of WO_3.

3.1.3. Typical anionic dyes photodegradation

Methyl orange (MO), a kind of azo dyes, is widely used in printing and dyeing textile industry. Similar to RhB and MB, the discharge of industrial wastewater containing MO into the water environment would bring many negative effects such as teratogenicity and carcinogenicity. The latest research activities of various Z-scheme nanocomposites on MO photocatalytic degradation was summarized in Table 3.

The photocatalytic performance of photocatalysts largely depend on the separation efficiency of photogenerated electron-hole pairs, visible light absorption efficiency and the stability of photocatalysts. Taking Ag-based photocatalyst as an example, we will discuss how to improve the photocatalytic performance of Ag-based photocatalysts by constructing a Z-scheme photocatalytic system.

Considerable studies have shown that Ag/AgCl exhibits excellent photocatalytic performance due to its SPR effect. However, the agglomeration of Ag/AgCl limits its utilization of visible light. Coupling Ag/AgCl with a suitable material to increase its visible light absorption efficiency is a good method to improve the photocatalytic performance of Ag/AgCl. Simultaneously, the separation efficiency of electron-hole pairs is also improved due to the metallic Ag as a charge transmission center. Metal-free such as polymer material, graphite carbon nitride (g-C_3N_4) is usually used to improve the photocatalytic performance of Ag/AgCl under the visible light irradiation. For example, because the C≡N bonds in polyacrylonitrile (CPAN) can be converted to C=N through a heat-treatment method to form a cyclized structure with conjugated groups. The resulting cyclized CPAN promote the π-electrode localization and increase the absorption intensity in the visible light region. Based on that, Li et al. [142] modified Ag/AgCl by coupling CPAN to synthesize CPAN/Ag/AgCl and discussed the photocatalytic performance towards MO photodegradation. In the photocatalytic process, AgCl cannot produce electron-hole pairs due to its wide band gap, while Ag nanoparticles can absorb visible light owing to its strong SPR effect and then produce photogenerated electrons and holes. Also, CPAN with a narrow band gap can be excited under visible light irradiation and generate holes and electrons. In this Z-scheme photocatalytic system, the electrons in the lowest unoccupied orbital of metallic Ag combine with the holes in the highest occupied molecular orbital of CPAN. Hence, the electrons stored in the lowest unoccupied molecular orbital react with the absorbed O_2 to form $\cdot O_2$, resulting the photodegradation of MO. Additionally, the holes in the lowest occupied orbital migrate to the surface AgCl and oxidize Cl^- ions to Cl^0. Then the formed Cl^0 participate in the oxidation of organic pollutants.

Different from AgCl, the band gap of AgBr is 2.6 eV, which can be excited under visible light irradiation. However, the rapid recombination of photogenerated electrons and holes causes low photocatalytic performance. In order to promote the separation efficiency, Xu et al. [148] dispersed different weight ratios of $ZnFe_2O_4$ on the surface of Ag/AgBr to synthesize $Ag/AgBr/ZnFe_2O_4$ through a simple hydrothermal route. DRS measurement indicates that the band gap of $Ag/AgBr/ZnFe_2O_4$ (2.36 eV) is smaller than that of Ag/AgBr (2.6 eV), thus promoting the visible light absorption efficiency. For $Ag/AgBr/ZnFe_2O_4$ composite photocatalysts, metallic Ag severs as the charge migration bridge to construct the Z-scheme system. Here, the photogenerated electrons in the CB of AgBr would transfer to Ag nanoparticles. At the same time, the photogenerated holes in the VB of $ZnFe_2O_4$ transfer to Ag and combine with the electrons. Therefore, the separation efficiency of electron-hole pairs could be efficiently improved, resulting in the strongly reductive electrons reduce absorbed O_2 to yield $\cdot O_2$ and the strongly oxidative holes directly oxidize organic pollutants. As a result, such charge transfer pathway enhances the photocatalytic performance of $Ag/AgBr/ZnFe_2O_4$.

Silver phosphate (Ag_3PO_4) with a constructive effect of both the large dispersion of CB and the inductive effect of PO_4^{3-} is regarded as an efficient visible light photocatalyst for the photocatalytic degradation of organic dyes. However, its poor stability due to the photo-corrosion limits its photocatalytic performance, constructing Z-scheme photocatalytic system via coupling with other semiconductor seems an ideal strategy to improve its stability. For example, loading Ag_3PO_4 on In_2S_3 hierarchical microspheres to synthesize Ag_3PO_4/In_2S_3 composite photocatalysts through a facile precipitate method [144]. Compared with pure Ag_3PO_4 and In_2S_3, the absorption edge of Ag_3PO_4/In_2S_3 show red-shift to long wavelength, resulting in a higher utilization efficiency of solar light. Additionally, loading Ag_3PO_4 nanoparticles on In_2S_3 hierarchical microspheres dramatically increase the surface area of In_2S_3, which provides more active sites to absorb the target pollutants. Ag nanoparticles in the Ag_3PO_4/In_2S_3 Z-scheme system function as the charge migration bridge to quickly capture photogenerated electrons in the CB of Ag_3PO_4 and then transfer it to the

VB of In_2S_3. This process inhibits the reduction of Ag^+ ions, thus improving the stability of Ag_3PO_4/In_2S_3. Additionally, the strongly reductive photogenerated electrons stored in the CB of In_2S_3 can reduce absorbed O_2 to $.O_2^-$, and the holes in the VB of Ag_3PO_4 can react with H_2O/OH^- to generate .OH, those formed active species participate in the photodegradation of target pollutants over the surface of photocatalysts. Shao et al. [151] prepared Ag_3PO_4/TiO_2@-MoS_2 with different content of TiO_2@MoS_2 through chemical deposition. DRS result demonstrated that the light absorption capability of 3D composite Ag_3PO_4/TiO_2@MoS_2 with 3.5 wt% TiO_2@MoS_2 depositing was greatly enhanced compared with Ag_3PO_4, which is attributed to the fact that the TiO_2@MoS_2 heterostructure maximizes the edge position of MoS_2 and reduces the recombination rate of electron and hole in Ag_3PO_4. Additionally, the face-to-face restacking of MoS_2 was restrained by TiO_2@MoS_2 heterostructure and achieved better separation of photogenerated electrons. In the Ag_3PO_4/TiO_2@MoS_2 system, TiO_2 function as the 'wire' to guide electrons captured by MoS_2 and shift electrons to solution. Those electrons can react with H_2O, O_2 or OH^- to generate active species, while the holes in the VB of Ag_3PO_4 can directly oxidize the organic pollutants or react with OH– to yield .OH. Hence, Ag_3PO_4/TiO_2@MoS_2 composite exhibited an excellent photodegradation efficiency and stability.

Additionally, Guo and her co-workers [81] deposited the Ag_3PO_4 onto the surface of crumpled Fe_3O_4@MoS_2 nanosphere to synthesize hierarchical Fe_3O_4@MoS_2/Ag_3PO_4 photocatalyst. The as-prepared Fe_3O_4@MoS_2/Ag_3PO_4 with 6 wt% Ag_3PO_4 loading exhibited highest photocatalytic activity for the CR photodegradation. The excellent photocatalytic performance is mainly attributed to the following advantages: firstly, the electrons transfer in the Fe_3O_4@MoS_2/Ag_3PO_4 composites followed the Z-scheme mechanism, the photogenerated electrons in the CB of Ag_3PO_4 transfer to the VB of MoS_2 and then combine with the holes therein, resulting in an efficient separation of electron-hole pairs. Secondly, two-dimensional crumpled MoS_2 nanosheets with huge specific surface area are in favor of the deposition of Ag_3PO_4 and also provided more active sites to degrade pollutants. Finally, the presence of MoS_2 nanosheets inhibit the photo-corrosion of Ag_3PO_4, thereby increasing the stability of the photocatalyst.

3.1.4. Persistent organic pollutants photodegradation

Compared to ordinary dyes, persistent organic pollutants (POPs) with a long half-life can resist to degradation, which pose a greater threat to humans and the environment. Hence, the degradation of such pollutants is of great significance. As shown in Table 4, the latest studies on photodegradation of POPs based on Z-scheme photocatalysts are recorded.

The separation efficiency of electron-hole pairs is of great significance for the photocatalytic performance of photocatalysts. Charge recombination center at the interface facilitate the combination of weak oxidative holes and reductive electrons, which greatly promote the separation of electrons and holes. For all-solid-state Z-scheme photocatalytic system, electron mediators acting as charge transfer bridges or charge recombination centers facilitate the separation of electron-hole pairs, resulting in an excellent photocatalytic performance of photocatalysts. For example, Ma and his co-workers [161] prepared all-solid-state Z-scheme g-C_3N_4/RGO/Bi_2WO_6 photocatalysts through hydrothermal method and evaluated its photocatalytic performance towards 2,4,6-trichlorophenol (TCP) photodegradation. The enhanced photocatalytic performance of g-C_3N_4/RGO/Bi_2WO_6 is attributed to RGO as the charge transfer bridge in Z-scheme system, the photogenerated electrons in the CB of Bi_2WO_6 migrate quickly to the VB of g-C_3N_4 and combine with the holes therein. Therefore, not only can the electron-hole pairs be efficiently separated, but also the inherent strong redox ability of the electron-hole is retained. Ag_3PO_4/MoS_2 composites with different weight ratios of MoS_2 prepared through ethanol-water mixed solvents precipitation method were examined towards the photocatalytic degradation of phenol [121]. The MoS_2 with a two-dimensional π-conjugated structure could function as an electron acceptor. The photogenerated electrons in the CB of Ag_3PO_4 transfer to metallic Ag via the Schottky barrier, meanwhile, the photogenerated holes in the VB of MoS_2 migrate to Ag nanoparticles and combine with the electrons. The photogenerated electrons stored in the CB of MoS_2 reduce absorbed O_2 to yield $.O_2^-$, then the photogenerated holes left in the VB of Ag_3PO_4 and the formed $.O_2^-$ participated in the photodegradation of target pollutants. Therefore, Ag_3PO_4/MoS_2 composites show excellent photocatalytic performance. The g-C_3N_4/Ag_3PO_4 hybrids fabricated by Sun et al. [77] exhibited excellent visible-light driven photocatalytic activity towards the degradation of phenol and BPA. The SEM image indicates that the cross-linking structure provide enough contacting surface area between g-C_3N_4 and Ag_3PO_4, which promote the migration of electron-hole pairs over the photocatalysts. In g-C_3N_4/Ag_3PO_4 Z-scheme system, the photogenerated electrons in the CB of Ag_3PO_4 would quickly transfer to the VB of g-C_3N_4 and combine with the holes therein, resulting in the efficient separation of electron-hole pairs. Simultaneously, relatively fast electron transfer greatly inhibits the photo-corrosion of Ag_3PO_4 and improve the stability of composites. Chen and his co-workers [171] synthesized close-connected AgI/Bi_5O_7I photocatalysts through a facile deposition-precipitation method. The photocatalytic performance of the AgI/Bi_5O_7I composites are evaluated for the photodegradation of antibiotics including tetracycline (TC), deoxy tetracycline (DTC), oxytetracycline (OTC), and ciprofloxacin (CIP) under visible light irradiation. The UV–vis absorption spectra indicate that the visible light response region of AgI/Bi_5O_7I is wider than that of Bi_5O_7I, thus the visible light absorption of Bi_5O_7I is distinctly improved after coupling with AgI. In addition, Photoluminescence, Photocurrent, and Electrochemical Impedance Spectroscopy experimental results demonstrate that the separation of electron-hole pairs is greatly improved, which is ascribe to the fact that charge transfer follows the Z-scheme mechanism in AgI/Bi_5O_7I composites. Here, small amount of Ag^0 formed in the early photocatalytic process could function as the charge recombination center, the photogenerated electrons in the CB of Bi_5O_7I transfer to metallic Ag, simultaneously, the holes in the VB of AgI also migrate to Ag nanoparticles and combine with the electrons. Hence, the electrons stored in the CB of AgI can reduce O_2 to generate $.O_2^-$, and the holes left in the VB of Bi_5O_7I can directly oxidize the pollutants or oxidize OH^- to produce .OH. In this way, the photogenerated charges are effectively separated and the photocatalytic performance of composites can be greatly enhanced.

Moreover, energy band structures of semiconductors also greatly influence the electron migration at the interface. Therefore, it is important to adjust the energy band structures to obtain an efficient separation of electron-hole pairs. Among them, electric fields caused by polarization play an important role in adjusting the energy band structure. For example, Li et al. [163] inserted $BiFeO_3$ between $BiVO_4$ and $CuInS_2$ to form the polarization-induced electric field. The photocurrent density tests indicate that the electron transfer is greatly promoted after the material is poles as $BiVO_4$-$BiFeO_3$-$CuInS_2$+. As show in Fig. 8 and Fig. 9, the photocurrent value of $CuInS_2$ is decreased from −0.07 to −0.01 mA cm^{-2} after coupling with $BiVO_4$-$BiFeO_3$, which is attribute to the energy band barrier between $BiFeO_3$ and $CuInS_2$, resulting in the electrons in the CB of $BiVO_4$ and $BiFeO_3$ cannot transfer to the CB of $CuInS_2$. In addition, the holes in the VB of $CuInS_2$ also cannot transfer to the $BiFeO_3$, which facilitate the recombination of electrons and holes within $CuInS_2$. While the photocurrent value is also decreased drastically when the material is poles as $BiVO_4$-$BiFeO_3$-$CuInS_2$-. Here, the photogenerated holes instead of

Table 3
Photocatalytic degradation of MO based on Z-scheme photocatalysts in aqueous solution.

Photocatalyst	Initial dye concentration	Catalyst dose ($g\ L^{-1}$)	Irradiation time (min)	Irradiated light/light source	Electron transfer	Photocatalytic activity	Ref.
Fe_2O_3/Ag-$_{(0\ 1\ 0)}$ $BiVO_4$	10 mg L^{-1}	1	150	500 W Xe lamp	All-solid-state Z-scheme	Fe_2O_3/Ag-$_{010}$$BiVO_4$: ~96% ($0.015\ min^{-1}$) (7.5×~ $BiVO_4$; 4.6×> Fe_2O_3-$BiVO_4$) (3.75×~ Ag-$_{(0\ 1\ 0)}$$BiVO_4$) $BiVO_4$: ~30% ($0.002\ min^{-1}$) Fe_2O_3-$BiVO_4$: ~43% ($0.0032\ min^{-1}$) Ag-$_{(0\ 1\ 0)}$ $BiVO_4$: ~51% ($0.004\ min^{-1}$)	[139]
Cu_2O/Au/$BiPO_4$	10 mg L^{-1}	1	60	300 W Xe lamp (190 < λ < 1100 nm)		Cu_2O/Au/$BiPO_4$: ~100% $BiPO_4$: ~20% Au/$BiPO_4$: ~40%	[140]
Ag/AgCl/$BiFeO_3$	1.0×10^{-5} mol L^{-1}	1	30	λ ≥ 420 nm		17.7 wt%-AgCl/Ag/$BiFeO_3$: ~100% ($0.1038\ min^{-1}$) (45×> $BiFeO_3$; 2×> $BiFeO_3$) $BiFeO_3$: $0.0023\ min^{-1}$ AgCl/Ag: $0.0513\ min^{-1}$	[141]
cyclized polyacrylonitrile/Ag/AgCl (CPAN/Ag/AgCl)	10 mg L^{-1}	1	60	300 W tungsten lamp with a 400 nm optical filter		CPAN/Ag/AgCl (1:5): ~76.3% ($0.12584\ min^{-1}$) (3×~ Ag/AgCl) Ag/AgCl: ~22.2% ($0.03775\ min^{-1}$) CPAN: ~0.5% ($0.00536\ min^{-1}$)	[142]
Ag/AgCl/g-C_3N_4	10 mg L^{-1}	1	180	300 W Xe lamp (λ ≥ 400 nm)		Ag/AgCl/g-C_3N_4 (2.7 at%): ~83.5% ($0.57961\ h^{-1}$) (6.77×~ g-C_3N_4; 6.27×~ Ag/g-C_3N_4) Ag/g-C_3N_4: ~24.4% ($0.09246\ h^{-1}$) g-C_3N_4: ~8.7% ($0.08556\ h^{-1}$)	[143]
Ag/Ag_3PO_4/In_2S_3	10 mg L^{-1}	1	25	300 W Xe arc lamp (400 < λ < 800 nm)		Ag_3PO_4/In_2S_3: ~100% (7 min) (6×> In_2S_3) In_2S_3: ~<80% (25 min)	[144]
MoS_2QDs-g-C_3N_4/Ag	10 mg L^{-1}	1	40	350 W Xe lamp		MoS_2QDs-g-C_3N_4/Ag: ~90% ($0.057\ min^{-1}$) (4.4× ~g-C_3N_4) g-C_3N_4: ~18%($0.013\ min^{-1}$)	[145]
Ag@AgBr/g-C_3N_4	10 mg L^{-1}	1	10	400 < λ < 680 nm		Ag@AgBr/g-C_3N_4(3:7): ~95% g-C_3N_4: ~19%	[66]
AgBr/ZnO/RGO	10 mg L^{-1}	0.5	60	300 W Xe lamp with a 400 nm filter		AgBr/ZnO/RGO: $k_{app} = 0.02336\ min^{-1}$ (12.8×> ZnO/RGO; 2.3×> AgBr/ZnO) AgBr/ZnO: $k_{app} = 0.01013\ min^{-1}$ ZnO/RGO: $k_{app} = 0.00183\ min^{-1}$	[146]
Cu_2O/Cu/AgBr/Ag	7 mg L^{-1}	0.4	90	300 W Xe-arc lamp (λ > 420 nm)		Cu_2O/Cu/AgBr/Ag: ~98% (50 min) bare Cu_2O: ~2% Cu_2O/AgBr: ~57% Cu_2O/AgBr/Ag: ~72%	[147]
Ag/AgBr/$ZnFe_2O_4$	10 mg L^{-1}	1	10	300 W Xe lamp (λ < 420 nm)		Ag/AgBr/$ZnFe_2O_4$: ~93.20% ($0.44991\ min^{-1}$) Ag/AgBr: ~84.1% ($0.17631\ min^{-1}$)	[148]
GO/Ag_2SO_3/AgBr	20 mg L^{-1}	0.625	18	500 W xenon lamp with a 420 nm UV cutoff filter (λ > 420 nm)		GO/Ag_2SO_3/AgBr: ~99.9% (9 min) Ag_2SO_3: ~55% (18 min) AgBr: ~88% (18 min) Ag_2SO_3/AgBr: ~99.9% (12 min)	[115]
AgI/Ag/AgBr	3.0×10^{-5} mol L^{-1}	2	16	λ > 420 nm		AgI/Ag/AgBr: ~97.0% ($0.207\ min^{-1}$) (1.87×> Ag/AgBr; 29.57×>	[149]

(*continued on next page*)

Table 3 (*continued*)

Photocatalyst	Initial dye concentration	Catalyst dose ($g\ L^{-1}$)	Irradiation time (min)	Irradiated light/light source	Electron transfer	Photocatalytic activity	Ref.
						Ag/AgI) Ag/AgBr: ~89.9% ($0.111\ min^{-1}$) Ag/AgI: ~8.8% ($0.007\ min^{-1}$)	
Ag/AgI/BiOI	10 mg L^{-1}	2	180	500 W Xe lamp ($\lambda > 420$ nm)		Ag/AgI/BiOI: ~93% ($0.950\ h^{-1}$) BiOI: $0.142\ h^{-1}$ AgI: $0.093\ h^{-1}$	[150]
Ag_2MoO_4/Ag_3PO_4	10 mg L^{-1}	0.4	6	350 W Xe lamp ($\lambda > 420$ nm)		Ag_2MoO_4/Ag_3PO_4: ~90%	[116]
Ag_3PO_4/MoS_2	10 mg L^{-1}	0.4	21	300 W xenon lamp ($\lambda > 400$ nm)	Direct Z-scheme	Ag_3PO_4/MoS_2: ~90% ($0.0964\ min^{-1}$) g-C_3N_4-N: ~18.5% ($0.0089\ min^{-1}$) Ag_2CrO_4: ~30.6% ($0.0163\ min^{-1}$)	[121]
$Ag_3PO_4/TiO_2@MoS_2$	2.5 mg L^{-1}	0.5	16	800 w xenon arc lamp		$Ag_3PO_4/TiO_2@MoS_2$(3.5 wt %): ~95% ($0.2085\ min^{-1}$) (2.5×~ Ag_3PO_4) Ag_3PO_4 ($0.0834\ min^{-1}$)	[151]
SnS_2/Ag_3PO_4	10 mg L^{-1}	0.2	60	500 W Xe-arc lamp ($\lambda > 400$ nm)		SnS_2/Ag_3PO_4: ~50% ($0.012\ min^{-1}$) (1.5× ~SnS_2; 2.0× ~Ag_3PO_4) SnS_2: $0.008\ min^{-1}$ Ag_3PO_4: $0.006\ min^{-1}$	[152]
g-C_3N_4/Ag_3PO_4	10 mg L^{-1}	0.8	40	500 W halogen lamp ($420 < \lambda < 800$ nm)		g-C_3N_4/Ag_3PO_4: ~92% ($0.0625\ min^{-1}$) (2.96×> b-g-C_3N_4/APO-20) (4.3× ~Ag_3PO_4; 312× ~g-C_3N_4) b-g-C_3N_4/APO-20: 70% ($0.0211\ min^{-1}$). g-C_3N_4: $0.0002\ min^{-1}$ Ag_3PO_4: $0.0144\ min^{-1}$	[77]
WO_3/Ag_2CrO_4	10 mg L^{-1}	0.2	120	300 W Xe lamp $\lambda > 420$ nm		WO_3/Ag_2CrO_4: ~44.5% ($0.00487\ min^{-1}$) (10.8× ~WO_3; 2.5× ~Ag_2CrO_4) Ag_2CrO_4: ~18.1% ($0.00158\ min^{-1}$) WO_3: $0.00034\ min^{-1}$	[153]
Ag_2CrO_4/g-C_3N_4	10 mg L^{-1}	0.2	120	300 W Xe-arc lamp ($\lambda > 420$ nm)		Ag_2CrO_4/g-C_3N_4: $0.0068\ min^{-1}$ (5.7×> g-C_3N_4; 4.3×> Ag_2CrO_4) g-C_3N_4: ~13.8% ($0.0012\ min^{-1}$) Ag_2CrO_4: ~18.1% ($0.0016\ min^{-1}$)	[154]
g-C_3N_4/Ag_2WO_4	10 mg L^{-1}	1	150	300 W Xe lamp		g-C_3N_4/Ag_2WO_4: ~95% g-C_3N_4: ~42% α-Ag_2WO_4: ~71%	[155]
g-$C_3N_4/BiOIO_3$	20 mg L^{-1}	1	180	300 W Xe arc lamp ($\lambda > 420$ nm)		$C_3N_4/BiOIO_3$(10:2): ~73%	[103]
$BiOI/TiO_2$	10 mg L^{-1}	1	25	500 W Xe lamp ($\lambda > 420$ nm)		$BiOI/TiO_2$: ~85% TiO_2: ~51.5%	[156]
$KNbO_3/Bi_2O_3$	1.0×10^{-5} mol L^{-1}	1	50	375 W mercury lamp ($\lambda < 365$ nm)		$KNbO_3/Bi_2O_3$: ~90.8% ($0.061\ min^{-1}$) (4.1×> Bi_2O_3; 7.1×> $KNbO_3$) Bi_2O_3: ~29.9% ($0.015\ min^{-1}$) $KNbO_3$: ~17.2% ($0.0086\ min^{-1}$)	[90]
g-$C_3N_4/Bi_2O_3/BiPO_4$	10 mg L^{-1}	1	160	—		g-$C_3N_4/Bi_2O_3/BiPO_4$: >90% ($0.01154\ min^{-1}$) $BiPO_4$: $0.0009\ min^{-1}$ g-$C_3N_4/BiPO_4$: $0.0055\ min^{-1}$ $Bi_2O_3/BiPO_4$: $0.00832\ min^{-1}$	[157]
TiO_2/g-C_3N_4	10 mg L^{-1}	1	80	500 W Xe lamp		TiO_2/g-C_3N_4: $0.012\ min^{-1}$ g-C_3N_4: $0.005\ min^{-1}$	[158]

Table 3 (*continued*)

Photocatalyst	Initial dye concentration	Catalyst dose ($g\ L^{-1}$)	Irradiation time (min)	Irradiated light/light source	Electron transfer	Photocatalytic activity	Ref.
g-C_3N_4 nanosheets /titania nanosheets(CNNS/TNS)	10 mg L^{-1}	1	90	300 W xenon lamp ($\lambda \geq 420$ nm)		0.7CNNS/0.3TNS: ~100% (2.34× > H-CNNS; 48.5× > H-TNS) H-TNS: ~10%	[159]
g-C_3N_4/Vo-ZnO	10 mg L^{-1}	1	60	$\lambda \geq 400$ nm		g-C_3N_4/Vo-ZnO: ~93%	[160]

electrons are driven from $BiFeO_3$ to $CuInS_2$, which is opposite to the direction of photocurrent inside $CuInS_2$. Thus, the electrons in the CB of $CuInS_2$ prefer to combine with the holes generated from $BiFeO_3$. However, the photocurrent value is greatly increased when the material is poles as $BiVO_4$-$BiFeO_3$-$CuInS_2$+. Due to the photogenerated electrons in the CB of $BiFeO_3$ transfer to the VB of $CuInS_2$ and combine with the holes therein, as a result, the electrons and holes can be efficiently separated. Therefore, a suitable electric field direction facilitate electron transfer through the Z-scheme mechanism. Chen and her co-workers [162] synthesized micro-nano $Ag_3PO_4/ZnFe_2O_4$ composites and evaluate the photodegradation efficiency of 2,4-dichlorophenol (2,4-DCP). The excellent photocatalytic performance of $Ag_3PO_4/ZnFe_2O_4$ is attributed to the enhanced separation efficiency of electrons and holes. In the photocatalytic process, a considerable number of defects accumulated in the contact interface of $ZnFe_2O_4$ and Ag_3PO_4 facilitate the formation of quasi-continuous energy levels, which endows the $ZnFe_2O_4$-Ag_3PO_4 contact interface the similar properties to conductors. The Ohmic contact is formed in the $ZnFe_2O_4$-Ag_3PO_4 contact interface due to its low electric resistance, which makes the $ZnFe_2O_4$-Ag_3PO_4 contact interface act as the charge recombination center for the photogenerated electrons from the CB of Ag_3PO_4 and the holes from the VB of $ZnFe_2O_4$. Therefore, the charge separation efficiency is greatly improved and the photocatalytic performance is also enhanced.

At present, the photodegradation of target pollutants by constructing a Z-scheme photocatalytic system is still a promising method. A large number of photocatalysts with excellent visible light response have been design, such as Ag-based, Bi-based, g-C_3N_4-based photocatalysts. However, the efficiency of charge separation is still not satisfactory. It is important to generate driving force at the interface of the photocatalytic oxidation system and the photocatalytic reduction system to control vector electron transfer and achieve efficient separation of electrons and holes. Among them, the adjustment of bandgap structure of semiconductors plays a significant role. Additionally, electron-mediators acting as undesired charge recombination center or charge transfer bridge also influence the separation efficiency of electron-hole pairs. Moreover, the photocatalytic performance of photocatalysts also depend on the visible light absorption density and the stability of the photocatalyst.

3.2. Inactivation of microorganisms

As 80% of illnesses in developing countries are caused by waterborne diseases, the elimination of pathogenic microorganisms such as bacteria, viruses and fungi play an important role in wastewater treatment [174–176]. What most important is to investigate the mechanism that leads to the inactivation of microorganisms. It is reported that the destruction of cell membrane is a pivotal process of cell inactivation. Studies have proved that most organic macromolecules will eventually be oxidized if given sufficient photocatalytic time. For example, pure TiO_2 can photo-oxidize organic macromolecules such as amino acids [177] and DNA [178]. The various targeting sites based on cell structure play significant roles in the overall photocatalytic inactivation process, including peptidoglycan, lipids and polysaccharides that make up the cell membranes and cell walls existing in the extracellular environment as well as the cytoplasm existing in the intracellular environment. Photocatalytic experiments and other reactions involving free radicals have demonstrated that lipids, especially polyunsaturated fatty acids (PUFA), are the main targets of oxidative radical [179,180]. Unsaturated fatty acid with free radical reacts with oxygen to form peroxyl radical, which in turn reacts with other nearby lipid molecules to produce additional lipid radicals. As these newly formed lipid radicals react with other unsaturated lipids, Radical chain reaction initiated by reactive oxygen species (ROS) is propagated and eventually destroy the important components of the cell.

Escherichia coli, a pathogenic microorganism, is prevalent in the intestine of warm-blooded vertebrates [181,182]. It enters the aquatic environment and then invades the body, which in turn cause numerous intestinal diseases such as peritonitis, cholecystitis, cystitis and diarrhea. However, the current water disinfection methods such as ozonation, chlorination and ultraviolet disinfection have secondary pollution and potential safety issues, especially the consumption of energy, thereby limiting its long-term sustainable development [183,184]. Therefore, solar-driven photocatalysis, an alternative "green", gentle, low-cost microbial inactivation method, came into being.

Photocatalysis is first proved to be an effective sterilization process by Matsunaga et al. who reported that *Lactobacillus acidophilus*, *Saccharomyces cerevisiae* and *Escherichia coli* were perfectly sterilized when they were incubated with TiO_2/Pt particles under metal halide lamp irradiation for 60–120 min [185]. Among the various types of photocatalysts, titanium dioxide (TiO_2) is widely recognized as one of the most promising photocatalysts in the field of bacteria inactivation owing to its excellent disinfection performances and wide availability, However, TiO_2 with large band gap energy of 3.2 eV just is excited under UV-light accounting for less than 5% of the solar spectrum, limiting its wider application [186]. The development of visible light driven photocatalysts have evolved from modified TiO_2 [187,188] to non-TiO_2 based semiconductor photocatalysts in the past few decades [189,190].

Up to now, Z-scheme photocatalysts with unique electron transfer pathway have become a hot spot for photocatalytic disinfection. For example, Wang et al. reported the disinfection of the *E. coli K-12* via Ni_2P/g-C_3N_4 exposed to a 300 W Xenon lamp with a 420 nm cut-off filter [191]. Scavenging studies using Cr(VI), isopropanol, Fe(II)-EDTA and oxalate as scavengers to validate the formation of holes, which are described as the main reactive species for the bacterial inactivation. Due to the electron transfer in Ni_2P/g-C_3N_4 composites following the Z-scheme mechanism, the Ni_2P capture the photogenerated electrons generated from g-C_3N_4 and suppress the recombination of electron-hole pairs, so that more holes can be used to enhance bacterial inactivation efficiency.

Table 4
Photocatalytic degradation of POPs based on Z-scheme photocatalysts in aqueous solution.

Photocatalyst	Initial concentration	Catalyst dose (g L^{-1})	Irradiation time (min)	Pollutants	Electron transfer	Photocatalytic activity	Ref.
g-C_3N_4/RGO/Bi_2WO_6	20 mg L^{-1}	1	120	2,4,6-trichlorophenol (TCP)	All-solid-state Z-scheme	100% g-C_3N_4/RGO/Bi_2WO_6: 98% Bi_2WO_6: 52% g-C_3N_4: 58% Bi_2WO_6/g-C_3N_4: 62%	[161]
g-C_3N_4/$BiOIO_3$	20 mg L^{-1}	1	180	2,4-dichlorophenol (2,4-DCP)	Direct Z-scheme	g-C_3N_4/$BiOIO_3$: 71%	[103]
Ag_3PO_4/$ZnFe_2O_4$ (w/w = 9:1)	20 mg L^{-1}	0.5	120	2, 4-dichlorophenol (2, 4-DCP)	Direct Z-scheme	Ag_3PO_4/$ZnFe_2O_4$: 86.08% (0.0155 min^{-1}) (5.74× ~$ZnFe_2O_4$) $ZnFe_2O_4$: 0.0027 min^{-1} (1.89× ~Ag_3PO_4) Ag_3PO_4: 0.0082 min^{-1}	[162]
$BiVO_4$/$BiFeO_3$/$CuInS_2$+	5 mg L^{-1}	—	120	4-nitrophenol (4-NP); 2,4-dichlorophenol (2,4-DCP)	Direct Z-scheme	4-NP: $BiVO_4$-$BiFeO_3$-$CuInS_2$+: 1.19 h^{-1} (2.8×> $CuInS_2$) $CuInS_2$: 0.43 h^{-1} $BiVO_4$-$CuInS_2$: 0.07 h^{-1} (16.9×> $BiVO_4$-$CuInS_2$) $BiVO_4$-$BiFeO_3$-$CuInS_2$: 0.38 h^{-1} 2,4-DCP: $BiVO_4$-$BiFeO_3$-$CuInS_2$+: 2.24 h^{-1} (1.6×> $CuInS_2$) $CuInS_2$: 1.41 h^{-1} (3.4×> $BiVO_4$-$CuInS_2$) $BiVO_4$-$CuInS_2$: 0.65 h^{-1} $BiVO_4$-$BiFeO_3$-$CuInS_2$: 1.11 h^{-1}	[163]
Ag_3PO_4@RGO@La,Cr:$SrTiO_3$	10 mg L^{-1}	1	60	2,4-DNP	All-solid-state Z-scheme	Ag_3PO_4@RGO@La,Cr:$SrTiO_3$: 0.052 min^{-1} Ag_3PO_4@RGO: 0.016 min^{-1} Ag_3PO_4: 0.004 min^{-1} La,Cr:$SrTiO_3$: 0.0005 min^{-1}	[73]
C/ZnO/CdS	1.0×10^{-4} mol L^{-1}	0.5	120	4-chlorophenol	Direct Z-scheme	C/ZnO/CdS: ~98%	[164]
g-C_3N_4/ZnO 10 wt% g-C_3N_4 (CN-10/OD-ZnO)	1.0×10^{-4} mol L^{-1}	1	90	4-chlorophenol (4-CP)	Direct Z-scheme	CN-10/OD-ZnO: ~95% (11×> g-C_3N_4) g-C_3N_4: ~34.2% (4.6×> OD-ZnO) OD-ZnO: ~64.2%	[165]
Attapulgite(ATP)/Cu_2O/Cu/g-C_3N_4	20 mg L^{-1}	0.08	120	chloramphenicol	All-solid-state Z-scheme	ATP/Cu_2O/Cu/g-C_3N_4: ~61%	[166]
RGO-Cu_2O/Bi_2O_3 Cu_2O/Bi_2O_3 = 8:2 GO: 50 mg (G50-8/2)	10 mg L^{-1}	0.5	180	tetracycline	All-solid-state Z-scheme	G50-8/2: ~75% (2×> RGO-Cu_2O) (2×> RGO-Bi_2O_3)	[43]
Ag_3PO_4/Ag/$BiVO_{4(0\,4\,0)}$	10 mg L^{-1}	0.5	60	tetracycline	All-solid-state Z-scheme	Ag/Ag_3PO_4/$BiVO_4$/RGO: ~94.96% pure $BiVO_4$: ~46.69% pure Ag_3PO_4: ~49.89%	[167]
Ag_3PO_4/$CuBi_2O_4$ 5 wt.%Ag_3PO_4 (ACBO-5)	10 mg L^{-1}	0.5	60	tetracycline	All-solid-state Z-scheme	ACBO-5: 75% (0.0201 min^{-1}) (2.79×> $CuBi_2O_4$) $CuBi_2O_4$: 32% (0.0072 min^{-1}) (2.16×> Ag_3PO_4) Ag_3PO_4: ~45% (0.0093 min^{-1})	[168]
Ag@g-C_3N_4@$BiVO_4$	20 mg L^{-1}	0.3	60	tetracycline (TC)	All-solid-state Z-scheme	Ag@g-C_3N_4@$BiVO_4$: ~90.76%. TiO_2: ~75.89% Ag@TiO_2: ~86.51%	[169]
AgI/WO_3 20 wt% AgI (20-A/W)	35 mg L^{-1}	1	60	tetracycline	Direct Z-scheme	20-A/W: 75% (0.0235 min^{-1}) (25×~WO_3) WO_3: ~5% (0.000927 min^{-1}) (4.3× ~AgI) AgI: ~28% (0.00544 min^{-1})	[170]
AgI/Bi_5O_7I (AI/BOI-5)	TC:20 mg L^{-1}, DTC、OTC、CIP:10 mg L^{-1}	0.5	40	tetracycline (TC); deoxy tetracycline (DTC); oxytetracycline (OTC); ciprofloxacin (CIP)	Direct Z-scheme	AI/BOI-5: ~93.81%(TC) (0.0107 min^{-1}) AI/BOI-5: ~41.65% (DTC), ~28.26% (OTC), ~40.58%(CIP)	[171]
BiOBr-Bi_2MoO_6	10 mg L^{-1}	0.2	120	Ciprofloxacin (CIP)	Direct Z-scheme	BiOBr-Bi_2MoO_6: ~84.63% BiOBr: ~38.36%	[95]

						Bi2MoO_6: ~15.21% g-C_3N_4/BiOBr/Au-B: 4.51 h^{-1} (3.8×>g-C_3N_4/BiOBr/Au-S) (1.18 h^{-1}) (5.8×>g-C_3N_4/BiOBr) (0.777 h^{-1}) 550 nm monochromatic light g-C_3N_4/BiOBr/Au-S: 0.408 h^{-1} (2.2×>g-C_3N_4/BiOBr/Au-B) (0.186 h^{-1}) (3.2×> g-C_3N_4/BiOBr) (0.129 h^{-1})	
CDots/WO_3	20 mg L^{-1}	0.5	210; 240	tetracycline hydrochloride (TCH); phenol	Direct Z-scheme	TCH :CDots/WO_3: ~78.6% (0.403 h^{-1}) (2.9×> WO_3) WO_3: ~40.8%(0.139 h^{-1}) Phenol :CDots/WO_3: ~70.2% WO_3: ~34.7%	[97]
Ag_2CrO_4/GO/g-C_3N_4	10 mg L^{-1}	0.2	90	Phenol; oxytetracycline	Double Z-scheme transfer	Ag_2CrO_4/GO/g-C_3N_4: 94.21% (phenol) Ag_2CrO_4/GO/g-C_3N_4: 81.34% (oxytetracycline)	[75]
Ag_2CO_3/N-g-C_3N_4 NG content of Ag_2CO_3-NG = 0.28 (Ag_2CO_3-NG-3)	8 mg L^{-1}	2	25	phenol	Direct Z-scheme	Ag_2CO_3-NG-3: ~90% (0.093 min^{-1}) (5× ~Ag_2CO_3) Ag_2CO_3: 0.022 min^{-1}	[172]
g-C_3N_4/Bi_4O_7	4.0×10^{-4} mol L^{-1}	0.8	140	phenol	Direct Z-scheme	g-C_3N_4/Bi_4O_7: ~93% Bi_4O_7: ~78%	[91]
Ag_3PO_4/MoS_2 MoS_2 = 0.648 wt% (Ag_3PO_4/MoS_2-15)	5 mg L^{-1}	0.6	200	phenol	All-solid-state Z-scheme	Ag_3PO_4/MoS_2-15: ~95%	[121]
Bi_2O_3-$BiVO_4$ composite microrods (CMRs)	25 mg L^{-1}	0.75	60	phenol	Direct Z-scheme	Bi_2O_3-$BiVO_4$ CMRs: ~96.3% Bi_2O_3/$BiVO_4$: ~2.06% Bi_2O_3: ~0.5% $BiVO_4$: ~0.6%	[173]
g-C_3N_4/Ag_3PO_4 (CN/APO)	phenol (4.0×10^{-4}mol L^{-1});BPA (10 mg L^{-1})	0.8	220; 50	Phenol; bisphenol A(BPA)	Direct Z-scheme	Phenol CN/APO-20: ~71% (0.0103 min^{-1}) (1.66×>b-g-C_3N_4/APO-20) b-g-C_3N_4/APO-20: ~51% bisphenol A (BPA) CN/APO-20: ~91% (0.0542 min^{-1}) (1.58×> b-g-C_3N_4/APO-20) b-g-C_3N_4/APO-20: ~65%	[77]
BiOBr/g-C_3N_4 the mass percentage of g-C_3N_4 = 60%	5 mg L^{-1}	1	100	bisphenol A (BPA)	Direct Z-scheme	BiOBr/g-C_3N_4-60%: ~95%	[93]
Bi_2MoO_6/MO (M Cu, $Co_{3/4}$, or Ni) 0.4 wt%CuO(Bi/Cu-3) 0.2 wt%Co_3O_4(Bi/Co-2) 0.2 wt%NiO(Bi/Ni-2)	10 mg L^{-1}	1	570	sulforhodamine B (SRhB)	Direct Z-scheme	Bi/Cu-3: ~21% (1.3×~Bi_2MoO_6) Bi/Co-2: ~32% (2.1×~ Bi_2MoO_6) Bi/Ni-2: ~66% (4.5×~ Bi_2MoO_6) Bi_2MoO_6: ~17%	[96]

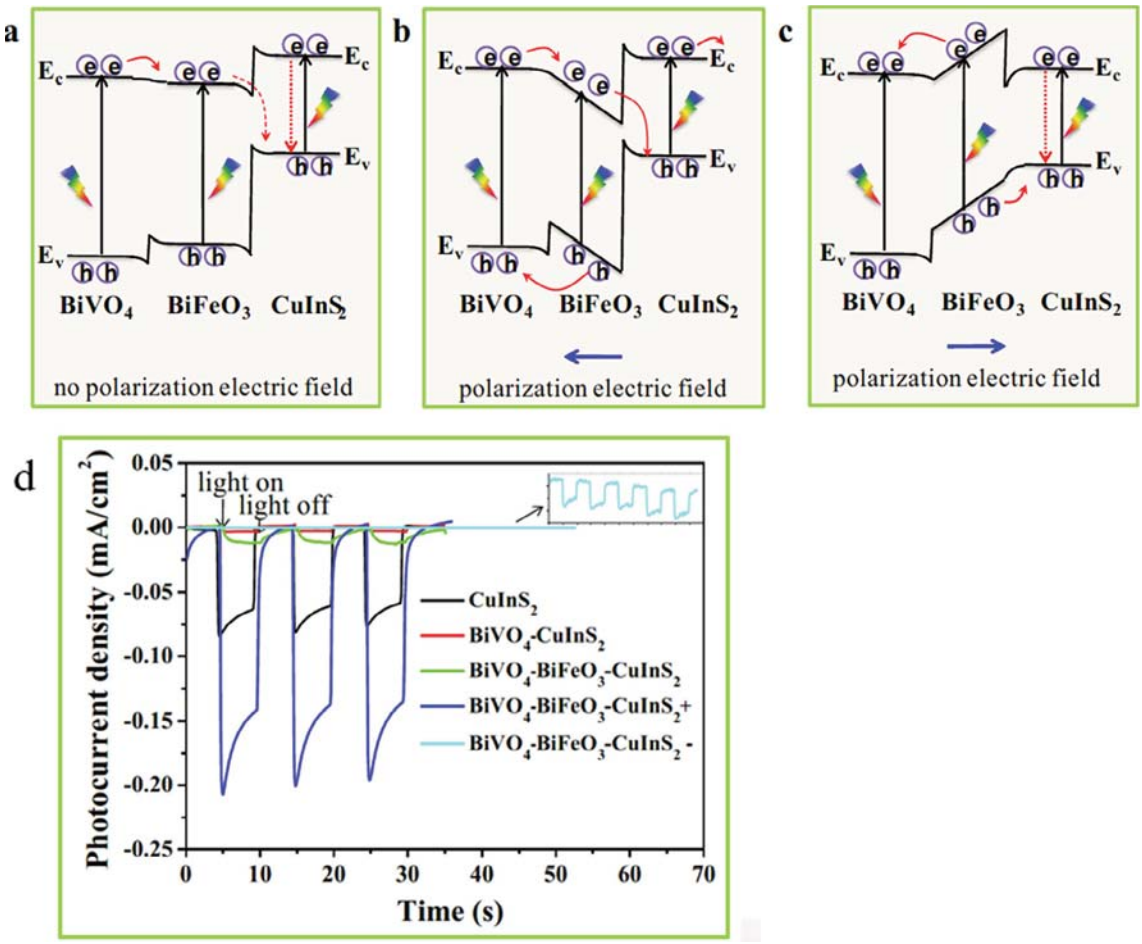

Fig. 8. Charge carrier transfer behaviors in $BiVO_4$-$BiFeO_3$-$CuInS_2$ (a) without polarization, (b-c) after polarization with different poling directions, (d) Photocurrent density-time plots of $BiVO_4$-$BiFeO_3$-$CuInS_2$ under visible light irradiation. Adapted and reprinted with permission from Ref. [163], Copyright 2017 Elsevier.

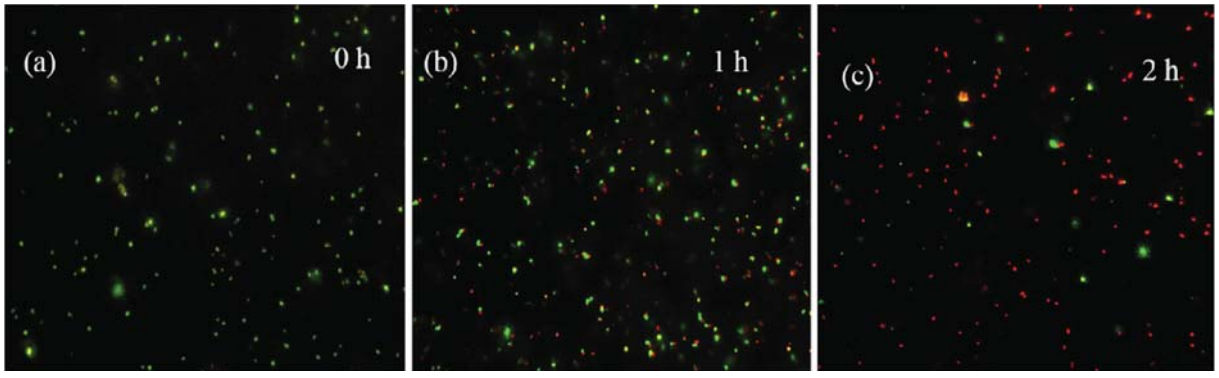

Fig. 9. (a-c) Fluorescence microscopic images. Adapted and reprinted with permission from Ref. [181], Copyright 2017 Elsevier.

The g-C_3N_4 with delocalized conjugated p structures lead to a relatively slow charge recombination rate and a more efficient separation of photogenerated charge, drawing widespread concern of researchers [192]. Xia et al. synthesized all-solid-state g-C_3N_4/m-Bi_2O_4 Z-scheme heterojunction photocatalysts [181]. The enhanced bacterial inactivation efficiency ascribes to the different role of reactive oxygen species. The photogenerated hole, $\cdot O_2^-$ and H_2O_2 played a synergic roles for the *E. coli* inactivation by g-C_3N_4/m-Bi_2O_4, whereas that of g-C_3N_4 was $\cdot O_2^-$ and hole and that of m-Bi_2O_4 was only hole. The Z-scheme heterojunction formed between g-C_3N_4 and m-Bi_2O_4 endows the photogenerated electrons populated to the higher CB and holes to the lower VB, so that more holes generated from m-Bi_2O_4 are used to attack *E. coli*. According to the fluorescence microscopy images (Fig. 9), the green fluorescent cells decreased in number are replaced by the red fluorescent cells in the bacterial destruction process since the generated ROS rupture the cell envelope. As a result, the respiratory chains is destroyed and the generation energy (ATP) is drastically decreased from 123.8 RLU·10^{-3} to zero after visible light irradiation for 1 h, the loss of ATP generation capacity directly caused bacterial death.

Zeng et al. [193] successfully prepared ternary Z-scheme TiO_2/WO_3/rGO composite photocatalysts by a simple hydrolysis-

hydrothermal method, in which WO_3 nanorods and TiO_2 nanocrystals were highly dispersed on rGO nanosheets. The photogenerated electrons in the CB of WO_3 transfer to the VB of TiO_2 through conductive rGO and combine with the holes, as a result, holes and electrons are enriched in the VB of WO_3 and the CB of TiO_2, respectively (Fig. 10a). As show in Fig. 10b, when the electrolyte buffer is saturated with O_2, the obvious currents are observed at about −0.3 V vs. NHE and 0.7 V vs. NHE, which indicates that both the one-electron reduction of O_2 to $\cdot O_2^-$ and the two-electron reduction of O_2 to H_2O_2 can occurred. The photogenerated electrons in the CB of TiO_2 reduce absorbed O_2 to $\cdot O_2^-$ and H_2O_2, and the holes in the VB of WO_3 oxidize H_2O to ·OH. Although the generation rate of ·OH on WO_3 is slower than that of TiO_2 and the oxidation capability of ·OH is stronger than $\cdot O_2^-$ and H_2O_2, the lifetime of ·OH is far shorter than $\cdot O_2^-$ and H_2O_2 and it can diffuse a very short distance in the aqueous solutions, so that the long-lived $\cdot O_2^-$ and H_2O_2 can still reach the *E. coli* cells (Fig. 10c-d). The experiment indicates that long-lived species (H_2O_2 and $\cdot O_2^-$) are more important than the short-life ·OH for photocatalytic disinfection relatively.

Guan et al. [194] fabricated AgI/$BiVO_4$ photocatalysts by a chemical deposition-precipitation approach and investigated the efficiency of photocatalytic disinfection of *E. coli*. Almost all *E. coli* cells (7.0×10^7 CFU mL^{-1}) could be inactivated by the AgI/$BiVO_4$ in 50 min while only 1.26-log and 1.18-log inactivation were observed by pure AgI and $BiVO_4$, respectively. The effect of antibacterial activity on the initial concentration of *E. coli* was also studied considering the practical wastewater treatment. The results showed that the inactivation efficiency decreased with the increase of initial bacterial concentration during the photocatalytic reaction. Probably because the higher initial concentration can extend the light path into the *E. coli* cell solution and reduce photons to the catalyst surface, leading to poor antibacterial properties. In the photocatalytic process, the photogenerated electrons in the CB of $BiVO_4$ combine with the holes in the VB of AgI due to the strong electrostatic attraction between AgI and $BiVO_4$, resulting in the electrons and holes are accumulated in the CB of AgI and the VB of $BiVO_4$, respectively. Consequently, the electrons reduce O_2 to $\cdot O_2^-$. Radical trapping experiments indicates that the holes and $\cdot O_2^-$ are the dominant reactive species for the bacterial inactivation, and the leakage of potassium ions (K^+) is the dominate reason for cell membrane rupture.

Liang et al. [195] described photocatalytic inactivation of Gram-negative strain *Escherichia coli* (*E. coli*) and Gram-positive strain *Staphylococcus aureus* (*S. aureus*), using Z-scheme AgI/Bi_2MoO_6 hybrid photocatalyst fabricated through a solvothermal-precipitation approach. The AgI particles are decorated onto the surface of Bi_2MoO_6 to form the AgI/Bi_2MoO_6 microstructure, which greatly maximize the interface areas. The charge migration at the interface of AgI and Bi_2MoO_6 largely depends on the local internal electric field (IEF). When the particle size of AgI is within the area of IEF, the photocatalytic performance of AgI/Bi_2MoO_6 is increase with the accumulation of AgI particles. In the AgI/Bi_2MoO_6 system, the Z-scheme structure is formed by the Ohmic contact between Bi_2MoO_6 and AgI, the photogenerated electrons in the CB of Bi_2MoO_6 combine with the holes in the VB of AgI, resulting in an excellent separation efficiency of electron-hole pairs. The electron spin resonance (ESR) analysis shows that the holes, $\cdot O_2^-$, e^- and H_2O_2 generated by AgI/Bi_2MoO_6 are the dominate reactive species for the bacterial inactivation. Further disinfection experiments under anaerobic conditions demonstrate that the electrons do not directly disinfect bacterial cells but participates in the formation of $\cdot O_2^-$ and H_2O_2, and the leakage of potassium ions (K^+) is the dominate reason for cell membrane rupture.

Photocatalytic disinfection has become a promising method to inactivate waterborne pathogens since the photocatalytic bacterial inactivation was reported by Matsunaga et al. in 1985 [185].

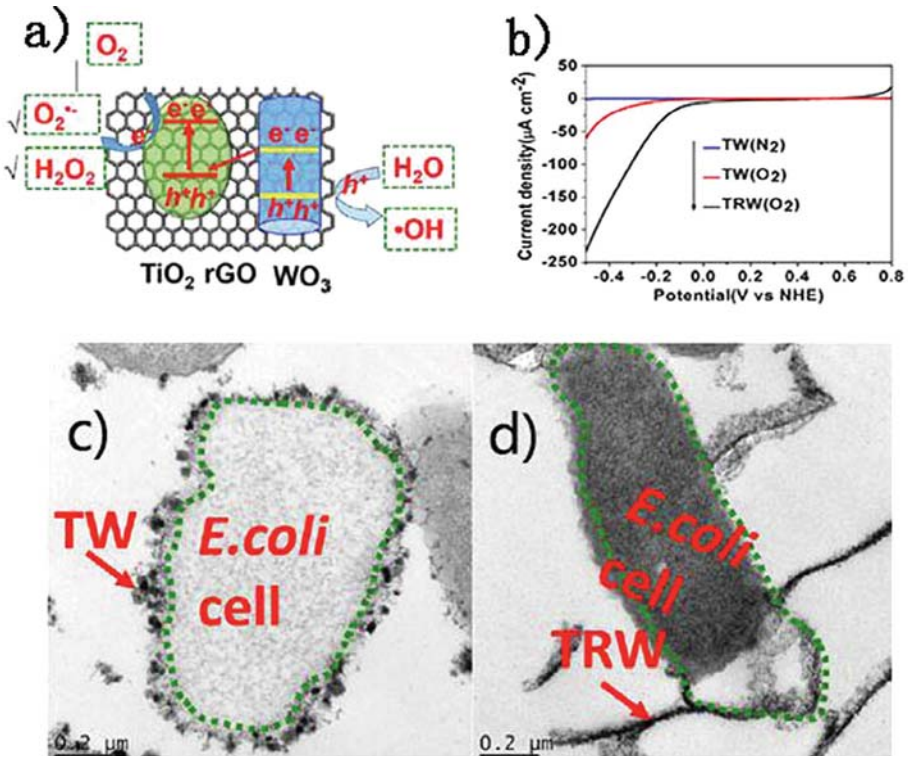

Fig. 10. (a) Schematic diagram for describing Z-scheme charge transfer and surface redox reactions for TiO_2/WO_3/rGO (TWR), (b) Current-potential curves of the prepared TiO_2/WO_3 (TW) and TWR electrodes in N_2 or O_2-saturated phosphate-buffered solutions (0.1 M, pH = 7.0), (c) TEM images of E. coli cells treated by TW photocatalytic suspension, (d) TEM images of E. coli cells treated by TWR photocatalytic suspension. Adapted and reprinted with permission from Ref. [193], Copyright 2017 Elsevier.

Photocatalysts can generated reactive species that can rupture the cell membrane under light irradiation. Artificial Z-scheme photocatalytic system promote the recombination of relatively weak oxidative holes and relatively weak reductive electrons, as a result, the intrinsic redox capacity of electron-hole pairs can be respectively preserved in the CB and VB of photocatalysts. However, the visible light absorption capacity of photocatalysts is still not very satisfactory, and increasing the amount of highly reactive species, especially relatively long-lived radicals, is also a key step in improving the efficiency of photocatalytic disinfection.

3.3. Reduction of heavy metal

Heavy metals exposed to the environment such as cadmium (Cd) [196-200] and lead (Pb) [201–203], have an adverse effect to biology. Hexavalent chromium (Cr (VI)), a common pollutant in groundwater and surface water, is widely used in metal processing, electroplating and leather tanning. The existence of Cr (VI) in aquatic system can invade the human body through the respiratory tract, skin, digestive tract and mucous membranes [204]. Therefore, it is necessary to remove Cr(VI) from the water at any cost.

Various methods have been used to remove or reduce Cr (VI) in the environment, including adsorption [205], precipitation [206], and reduction [207]. Photocatalytic reduction of highly toxic Cr (VI) to lowly toxic Cr (III) by photocatalysts, especially Z-scheme photocatalysts, is more effective and low-cost than chemical reduction. In recent years, in order to achieve efficient utilization of the sunlight, great efforts have been made to search for Z-scheme photocatalysts that exhibit highly efficient Cr (VI) reduction under visible light irradiation. For example, Yang et al. synthesized benzothiadiazole-Bi_2MoO_6 (BBT-BMO) via an in-situ palladium-catalyzed cross-coupling method and evaluated the photoreduction efficiency of Cr (VI) [208]. The maximum rate constant (0.081 min^{-1}) of the optimal composites was 80 times that of single Bi_2MoO_6. The accepted crucial for evaluating photocatalytic activity include surface reaction, solar light harvesting and photogenerated charge separation. N_2 absorption-desorption tests showed the BET surface area of BBT-MO was much higher than pure Bi_2MoO_6 and BBT, which might because of the greater dispersion of BBT on the surfaces of Bi_2MoO_6. The UV–vis absorption spectra demonstrated that the visible-light absorption edge of Bi_2MoO_6 was 460 nm, while BBT-BMO exhibited strong visible-light absorption ability from 42 to 700 nm. In addition, the conjugated microporous structure of BBT endowed it with superior electron transfer properties, which facilitated the recombination of CB-electrons of Bi_2MoO_6 and the HOMO-holes of BBT. The remaining electrons and holes with stronger redox ability significantly improved the photocatalytic performance of Cr (VI) reduction. Zhou et al. reported the photoreduction of Cr (VI) by $Nb_{3.49}N_{4.56}O_{0.44}/(Ga_xZn_{1-x})$ (N_xO_{1-x}). Nearly all the Cr (VI) was reduced by NbNO/GZNO (6.0) within 30 min, which was ascribed to the formation of Z-scheme system between $Nb_{3.49}N_{4.56}O_{0.44}$ and (Ga_xZn_{1-x}) (N_xO_{1-x}) [209]. Upon photoexcitation, the photogenerated electrons in the CB of (Ga_xZn_{1-x}) (N_xO_{1-x}) would transfer and recombine with the holes in the VB of $Nb_{3.49}N_{4.56}O_{0.44}$ owing to the interfacial electronic field and quasi continuous intermediate levels at the interface. Hence, the electrons in the CB of $Nb_{3.49}N_{4.56}O_{0.44}$ and the holes in the VB of (Ga_xZn_{1-x}) (N_xO_{1-x}) retain their original high redox capability to reduce Cr (VI) and oxidize water, respectively. Feng et al. [44] prepared core-shell structured Bi@BiOCl/g-C_3N_4 via a solvothermal method followed by an in-situ oxidation etching. About 82.3% of Cr (VI) was reduced by Bi@BiOCl/g-C_3N_4 within 80 min while pure p-g-C_3N_4 was inactive in Cr (VI) photo-reduction owing to the intimate interfaces in Bi@BiOCl/g-C_3N_4 and its proper energy band structure, of which Bi was functioned as Z-scheme bridge during the charge transfer. Specifically, the photogenerated electron in the CB of BiOCl would transfer and then recombined with the hole in the VB of g-C_3N_4 with the help of metallic Bi. The remaining electrons in the CB of g-C_3N_4 either directly reduced Cr (VI) or first reacted with absorbed O_2 to form $\cdot O_2^-$ and then reduce Cr (VI).

The photoreduction of Cr (VI) is a surface reaction, of which the negatively charged $Cr_2O_7^{2-}$ ions are reduced to Cr^{3+} under the acid condition while CrO_4^{2-} ions are reduced to Cr^{3+} and then the formed Cr (III) will be precipitated into $Cr(OH)_3$ in alkaline medium (Eq. (6–7)). Specifically, due to less active electrons and holes can be effectively diminished in Z-scheme photocatalytic system, as a result, more active electrons can escape from the pair recombination to enhance Cr (VI) reduction, maximizing the utilization of the active electrons and optimize the reduction ability of the photocatalytic system. The photogenerated electrons play a dominant role for Cr (VI) reduction. How to effectively separate photogenerated electron-hole pairs to release more active electrons to participate in the reduction reaction is a key step for Cr (VI) photoreduction. Simultaneously, the effect of pH values on the photocatalytic performance should be took into consideration. Because the zeta potentials of photocatalysts become more negative with the increase of pH values, the negative surface lead to electrostatic repel the anionic Cr(VI) and readily adsorption of the cationic Cr(III). Moreover, the formed Cr(III) will be precipitated into $Cr(OH)_3$ at pH > 6, which will mask the active sites of photocatalysts. Hence, studies on material modification methods should focus on how to allow more efficient channeling of the charge carriers into useful reduction reactions rather than recombination reactions [210,211].

$$Cr_2O_7^{2-} + 14H^+ + 6e^- \rightarrow 2Cr^{3+} + 7H_2O \quad (3.6)$$

$$CrO_4^{2-} + 4H_2O + 3e^- \rightarrow Cr(OH)_3 + 5OH^- \quad (3.7)$$

3.4. Energy conversion, the dawn of the future

Energy shortage can restrict social development and affect human life. Solar energy, environmentally friendly, wide distribution, has been regarded as the most promising candidate to solve above problem. There is an increasing desire to develop effective strategies to directly harvest solar energy and convert it into available energy. Photovoltaic cells such as batteries can directly convert solar energy into electricity, while the energy must be consumed immediately or stored in auxiliary equipment. Photocatalytic process of thermodynamic uphill reactions driving by the solar energy might be another attractive way to harness solar energy.

In general, the semiconductor based photocatalysts consists of a semiconductor particle for solar energy absorption and two redox catalysts for hydrogen and oxygen evolution, respectively (Fig. 11a) [212]. The semiconductor particles excited by solar energy produce electrons and holes in the CB and VB, respectively. The separated electrons and holes might diffuse within the semiconductor and eventually migrate to the redox catalysts to facilitate the desired redox reactions. In order to achieve water splitting, the band gap of semiconductor must be higher than the redox potential of H^+/H_2 (0 eV) and O_2/H_2O (1.23 eV). Additionally, the semiconductor particles must be tightly integrated with the selected redox catalyst for effectively harnessing photogenerated charge for the desired photochemical reaction. Finally, a mechanism protecting semiconductors from direct electrochemical reactions is necessary to ensure photoelectrochemical stability of the system. Although considerable efforts have been made to optimize the photocatalyst construction, the charge separation is still restricted. In addition, the undesired semiconductor degradation

reaction might occur if the separated electrons with high reduction potential and holes with high oxidation potential reached the surface of the semiconductor (Fig. 11b). Hence, designing a photocatalyst with excellent light harvesting capability and photoelectrochemical stability is a big challenge.

Heterogeneous photocatalysts not only enhance the light absorption region of wide band gaps materials through functionalization or sensitization with small band gap semiconductors or molecules, but also facilitate the charge separation by forming built-in electrical potential between semiconductors. Among them, artificial Z-scheme system coupled a photocatalyst for H_2 evolution and another photocatalyst for O_2 evolution with an electron mediator. In this system, each photocatalyst is only involved in one half reaction of water splitting, the electron mediator is oxidized on the H_2 evolution photocatalyst and reduced on the O_2 evolution photocatalyst. Considerable efforts have been made on the construction of Z-scheme systems using different materials (Table 5).

3.4.1. Overall water splitting

$SrTiO_3$ photocatalysts with ideal cubic perovskite structure can maintain the valence-state of metal cations and thereby determining the lifetime of photogenerated charge carriers and the light responsiveness, which makes it excellent materials toward water-splitting to H_2 and O_2 [241]. Sayama et al. [29] first reported the stoichiometric splitting of water into H_2 and O_2 under visible light irradiation using a mixture of Pt-WO_3 and Pt-$SrTiO_3$ photocatalysts and an IO_3^-/I^- shuttle redox mediator. Compared with the single Pt-$SrTiO_3$, the H_2 evolution rate of mixed catalysts was higher. This enhancement was attributed to the added Pt-WO_3 effectively reduced the IO_3^- into I^- and finished O_2 evolution at the same time, inhibiting the effect of cumulative IO_3^- on H_2 evolution. Recently, Chen et al. [213] successfully synthesized $SrTiO_3$:(Cr/Ta) photocatalysts via a polymerizable complex method and also studied the effect of synthesis method and doping amounts to the photocatalytic performance. For H_2 evolution photocatalyst, the result of the density of states (DOS) indicated that, after Cr/Ta co-doping, the Cr 3d and O 2p orbitals formed some new impurity states between VB maximum and CB minimum of $SrTiO_3$, which promotes the excitation of low-energy photons. Here the doped Ta acted as the center of charge recombination, inhibiting the appearance of undesired Cr^{6+}. The high crystalline quality and relatively large specific surface area of the photocatalyst not only reduce the recombination possibility of photoinduced carriers, but also generate a considerable number of active sites for water splitting. Niishiro et al. [215] evaluated the photocatalytic efficiency of water splitting by rhodium (Rh) and antimony (Sb) co-doped $SrTiO_3$ photocatalyst ($SrTiO_3$: Rh/Sb). Here, the effective Rh species involved in the H_2 evolution was different from that of the O_2 evolution. For H_2 evolution reaction, unstable and reversible Rh^{3+} ions formed by the reduction of Rh^{4+} ions are the dominant species of H_2 evolution. For O_2 evolution reaction, even visible-light-sensitized $SrTiO_3$: Rh/Sb photocatalysts doped with Sb cannot achieve four-electron oxidation of water to form O_2 (Fig. 12). However, when IrO_x co-catalyst was loaded on the surface of $SrTiO_3$: Rh/Sb, the O_2 evolution rate was drastically improved. In this process, IrO_x co-catalyst and stabilized Rh^{3+} ions formed by co-doped Sb play a significant role. The unstable Rh^{3+} ions possessing higher electron-donating property form an electron donor levels in more negative position, thus resulting in the energy-gap narrowing and the red shift of the action spectrum. This study achieved the application of half reaction of water to overall water splitting via co-doping technique.

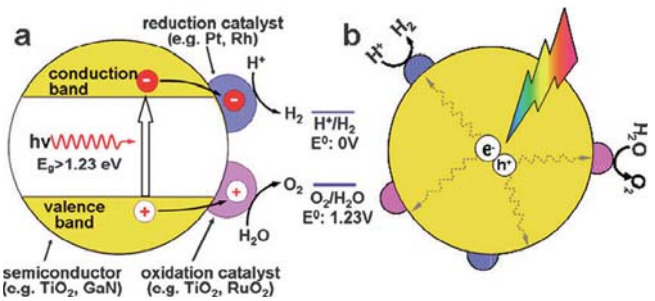

Fig. 11. (a) Schematic illustration of a semiconductor particle based photocatalyst that can be used for water splitting and hydrogen generation; (b) Due to the lack of intrinsic driving force to direct charge separation and transportation in this construction of a photocatalyst, a major portion of the photogenerated charges may not reach the redox catalysts for productive redox reactions before consumed through recombination or undesired semiconductor degradation reactions. Adapted and reprinted with permission from Ref. [212], Copyright 2012 The Royal Society of Chemistry.

3.4.2. H_2 evolution reaction

Hydrogen, a clean and high heating value energy carrier, has got great attention due to the depletion of fossil fuel energy and its adverse impact on the environment. Photocatalytic water splitting is considered as an ideal strategy for the generation of H_2. However, hydrogen production efficiency is limited in practical applications because of the high electron-hole recombination rate of photocatalysts [242,243]. Constructing Z-scheme photocatalytic system to suppress the recombination of electron-hole might be an ideal strategy to solve above problems. Hence, various Z-scheme photocatalysts have been designed to enhance the hydrogen production efficiency. For example, Ng et al. [217] fabricated $Zn_{0.5}Cd_{0.5}S$-MWCNT-TiO_2 core-shell nanocomposites via coating and co-precipitation-hydrothermal route. The H_2-evolution rate reached 21.9 μmol h^{-1} over $Zn_{0.5}Cd_{0.5}S$-MWCNT-TiO_2, which was 4.5 times and 2.8 times higher than that of pure $Zn_{0.5}Cd_{0.5}S$ and binary MWCNT-$Zn_{0.5}Cd_{0.5}S$, respectively. This enhanced photocatalytic performance was mainly due to the use of MWCNTs as a solid-state electron mediator to improve vector electron transfer from TiO_2 to $Zn_{0.5}Cd_{0.5}S$. The direct Z-scheme Er^{3+}: $YAlO_3/Ta_2O_5$-$CaIn_2S_4/MoSe_2$-RGO showed higher photocatalytic H_2-evolution compared with $CaIn_2S_4/MoSe_2$-RGO and Er^{3+}: $YAlO_3/Ta_2O_5/MoSe_2$-RGO under visible-light irradiation [218]. The DRS and PL spectra confirmed that Ta_2O_5 was activated by high-energy ultraviolet light emitting from Er^{3+}:$YAlO_3$, achieving efficient photocatalytic hydrogen-evolution (210 μmol h^{-1} g^{-1}). Zhu et al. [222] constructed ternary $ZnIn_2S_4$/RGO/$BiVO_4$ all-solid-state Z-scheme photocatalyst and estimated the H_2 production with different mass ratio of $ZnIn_2S_4$ to $BiVO_4$. The optimal La-$ZnIn_2S_4$/RGO/RuO_2/$BiVO_4$ composites with 1:5 mass ratio of $ZnIn_2S_4$ to $BiVO_4$, 1.5 wt% RGO and 1.0 wt% RuO_2 loading was obtained and the H_2-evolution rate was 4.1 μmol h^{-1} g^{-1}. It can be explained that the recombination of the holes in the VB of $ZnIn_2S_4$ and the electrons in the CB of $BiVO_4$ was promoted by graphene.

Direct Z-scheme $Ta_3N_5/WO_{2.72}$ photocatalysts was prepared through depositing Ta_3N_5 on $WO_{2.72}$ sol [230]. The as-prepared $Ta_3N_5/WO_{2.72}$ showed higher H_2-evolution (5.3 μmol h^{-1} g^{-1}) compared with pure Ta_3N_5 thin film (13.2 μmol h^{-1} g^{-1}) under the visible light, and highest H_2 evolution of 46.4 μmol h^{-1} g^{-1} was obtained after loading Pt nanoparticles. In contrast, the enhancement of H_2-evolution in the NaI-mediated liquid Z-scheme system was insignificant, which demonstrated that conformal coating of Ta_3N_5 on $WO_{2.72}$ enhanced well physical contact between the two photocatalysts, thereby promoting the transfer of charges.

Compared to all-solid-state Z-scheme systems, direct Z-scheme system might show more excellent photocatalytic performance for H_2 evolution as the electron mediators limit such combination to several system and might shield incident light. However, the elec-

Table 5
Half-reaction of H_2 or O_2 evolution and overall water splitting based on Z-scheme photocatalysts.

Photocatalyst	Electron transfer	Application	Reaction conditions	Photocatalytic activity	Ref.
Pt/$SrTiO_3$:(Cr/Ta)(H_2) Pt/WO_3 (O_2)	Direct Z-scheme	Water splitting	350 mL top irradiation reaction quartz cell; 65 mL methanol solution (10 vol%) containing H_2PtCl_6; 100 mg photocatalyst; 300 W Xe lamp (λ < 420 nm); 65 mL NaI aqueous solution (5 mmol L^{-1}); 4 h reaction time	0.3 wt%Pt/STO:(2%Cr/Ta): 610 μmol h^{-1} g^{-1} (H_2) AYQ = 2.6% (λ = 420 nm) 0.5 wt%Pt/WO_3:270 μmol h^{-1} g^{-1} (O_2) AYQ = 1.52% (λ = 420 nm)	[213]
PtOx/β-Ni(OH)$_2$/WO_3	Redox mediator Z-scheme		home-made side-irradiation-type Pyrex reaction cell; 150 W Xe lamp; 100 mg photocatalyst; 200 mL aqueous solution; 0.01 M $AgNO_3$ and10% (v/v) triethanolamine-water solution; 200 mL 5 mM NaI or 2 mM $FeCl_2$ aqueous solution; 5 h reaction time	1%PtOx/β-Ni(OH)$_2$/WO_3: H_2: 502 μmol h^{-1} g^{-1} O_2: 243 μmol h^{-1} g^{-1} AQE: 4.94% (λ = 365 nm) AQE: 4.01% (λ = 405 nm)	[17]
$BiVO_4$/CDs (carbon dots)/CdS	All-solid-state Z-scheme		Pyrex glass photoreactor; 80 mg photocatalyst; 100 mL ultrapure water; 300 W Xe-lamp (λ > 420 nm); 25 h reaction time	$BiVO_4$/CDs/CdS (mass ratio $BiVO_4$/CdS = 50%) H_2: 15.5 μmol h^{-1} g^{-1} O_2: 7.625 μmol h^{-1} g^{-1}	[214]
H_2:Pt(0.3 wt%)/$SrTiO_3$:Rh(2%) O_2: IrO_X(3.0 wt%)/$SrTiO_3$:Rh(1%)/Sb(1%)	Fe^{3+}/Fe^{2+} redox couple		10 vol% methanol solution (H_2); 0.02 mol L^{-1} silver nitrate solution; top window made of Pyrex; 200 mg photocatalyst; 150 mL reactant solution; top window made of Pyrex; 300 W Xe lamp (λ > 420 nm); 5 h reaction time	A.Q.Y: (λ = 420 nm) Pt(0.3 wt%)/$SrTiO_3$:Rh(1%)/Sb(1%): 0.8% (H_2) IrO_X (3 wt%)/$SrTiO_3$:Rh(1%)/Sb(1%) : 4.5% (O_2)	[215]
Pt/micro-SiC and WO_3	Direct Z-scheme		Lab solar II system; 300 mL Pyrex reaction vessel; 50 mg WO_3 and 50 mg Pt/SiC; 100 mL deionized water containing 0.01 mol/L NaI (pH = 3); (λ ≥ 420 nm); 4 h reaction time	A.Q.Y: 0.021% (λ = 420 nm) SiC/Pt (H_2): 125.5 μmol h^{-1} g^{-1} WO_3 (O_2): 62 μmol h^{-1} g^{-1}	[216]
$Zn_{0.5}Cd_{0.5}S$-MWCNT-TiO_2	All-solid-state Z-scheme	H_2-evolution	30 mg photocatalyst; 120 mL aqueous mixture of Na2S (0.1 M) and Na2SO3(0.1 M); Pyrex side-irradiated cell; 500 W Xe lamp (AM 1.5); 6 h reaction time.	$Zn_{0.5}Cd_{0.5}S$-MWCNT-TiO_2: 3.65 μmol h^{-1} g^{-1} (4.5× ~$Zn_{0.5}Cd_{0.5}S$) (2.8× ~MWCNT-$Zn_{0.5}Cd_{0.5}S$)	[217]
Er^{3+}: $YAlO_3$/Ta_2O_5-$CaIn_2S_4$/$MoSe_2$/RGO (mass ratio of Er^{3+}:$YAlO_3$ to Ta_2O_5 = 50:100, Ta_2O_5 to $CaIn_2S_4$ = 100:100 and 1.0 wt% $MoSe_2$-RGO)	Direct Z-scheme		500 mL Pyrex reactor; 250 mg photocatalyst; methanol–water solution(10.0 wt%); 300 W xenon Lamp; 5 h reaction time	210 μmol h^{-1} g^{-1}	[218]
ZnO/CdS	Direct Z-scheme		CEL-SPH2N photocatalytic water-splitting testing system; 50 mL aqueous solution (0.1 M Na_2S and 0.1 M Na_2SO_3); 300 W xenon lamp; 5 h reaction time	5500 μmol h^{-1} m^{-1} (2.7× ~CdS) (2.0× ~ZnO/CdS)	[219]
Pt/$BiVO_4$/CdS ($BiVO_4$NWs/CdS = 1:2)	Direct Z-scheme		Pyrex top-irradiation reaction vessel; 50 mg of photocatalyst; 200 mL lac-tic acid (20 vol%) solution/1 M Na_2SO_3 solution; 300 W Xe lamp with 420 nm cutting off; 10 h reaction time	CdS/$BiVO_4$: 2480 μmol h^{-1} g^{-1} (3.65× ~CdS) CdS: 680 μmol h^{-1} g^{-1} Pt/CdS/$BiVO_4$: 23060 μmol h^{-1} g^{-1} (2.03×~ Pt/CdS) Pt/CdS :11360 μmol h^{-1} g^{-1}	[220]
TiO_2/WO_3@MoS_2 (TWM) (60 wt% MoS_2)	All-solid-state Z-scheme		300 W Xe arc lamp; quartz reactor; 40 mL deionized water and 25 mL methyl alcohol; 50 mg photocatalyst; 1 h irradiation	TiO_2/WO_3@MoS_2: 273.69 μmol h^{-1} g^{-1} WO_3/TiO_2 NFs: 24.59 μmol h^{-1} g^{-1} TiO_2@MoS_2: 171.24 μmol h^{-1} g^{-1}	[221]
1.0La-$ZnIn_2S_4$/1.5RGO/1.0RuO_2/$BiVO_4$ ($ZnIn_2S_4$:$BiVO_4$ = 1:5)	All-solid-state Z-scheme		868 mL gastight stainless steel reactor; 350-W Xe lamp; 200 mL of deionized water; 200 mg photocatalyst; 10 h reaction time	4.1 μmol h^{-1} g^{-1} A.Q.Y.: 0.8%	[222]
CdS/oxygen-defected $CdWO_4$ (molar ratio of $Cd(CH_3COO)_2$: CH_3CSNH_2 = 2)	Direct Z-scheme		20 mg photocatalyst; 100 mL aqueous solution containing 10 vol.%of lactic acid; quartz vessel; 300 W Xe lamp; 2 h reaction time	CdS/$CdWO_4$: 9.17 μmol h^{-1} g^{-1} (18×> CdS) CdS: 0.51 mmol h^{-1} g^{-1}	[223]
TiO_2/CdS (4.4 wt% CdS)	Direct Z-scheme		100 mL Pyrex flask; 350 W Xenon lamp; 50 mg photocatalyst; 80 mL methanol/water solution (25% methanol in volume); 3 h reaction time	TiO_2/CdS: 51.4 μmol h^{-1} (28×> TiO_2)	[224]
anatase/rutile TiO_2 (rapid cooling, 45 wt% rutile/55 wt% anatase)	Direct Z-scheme		100 mL Pyrex flask; 350 W Xe arc lamp; 50 mg photocatalyst; 80 mL of a mixed solution of methanol (16 mL) and water (64 mL); 3 h irradiation	RC500: 6.48 mmol h^{-1} g^{-1} AQE : 20.9%	[225]
Ni_2P/g-C_3N_4 (1% Ni_2P loading)	Direct Z-scheme		Pyrex reaction cell; 40 mg photocatalyst; 50 mL of aqueous solution containing 10 vol% triethanolamine (TEOA); 300 W Xenon lamp; 4 h reaction time	g-C_3N_4:~16.4 μmol h^{-1} g^{-1} Ni_2P/g-C_3N_4: 362.4 μmol h^{-1} g^{-1} (22×~ g-C_3N_4) AQE:1.8% (λ = 420 nm)	[191]
Pt/MoO_3/TiO_2 (loading 20% MoO_3 on the TiO_2)	All-solid-state Z-scheme		quartz reaction cell; 75 W side-irradiated Xenon lamp; 100 mg photocatalyst; 300 mL methanol solution (20 vol%); 1 h irradiation	MoO_3/Pt/TiO_2:169 μmol h^{-1} g^{-1} (4×> Pt/TiO_2; 2×> Pt/P25)	[226]
g-C_3N_4/Au/P25	All-solid-state Z-scheme		Top-illuminated, jacketed quartz photoreactor; 50 mg photocatalyst; 50 mL methanol/water (v/v = 3:7) solution; 300 W Xe lamp; 5 h irradiation	g-C_3N_4/Au/P25: 259 μmol h^{-1} g^{-1} (30×>g-C_3N_4) (1.15×~ Au/g-C_3N_4-P25) g-C_3N_4-P25 (w/w = 8:2): 7.72 μmol h^{-1} g^{-1} 0.2 wt%-Au/g-C_3N_4-P25: 219 μmol h^{-1} g^{-1} (g-C_3N_4-P25 (w/w = 8:2))	[227]
$Cd_xZn_{1-x}S$/Au/g-C_3N_4	Direct Z-scheme		Pyrex reaction cell with top irradiation; 300 W Xe lamp; 50 mg photocatalyst; 100 mL aqueous solution containing 0.1 mol L^{-1} glucose; 10 h irradiation	$Cd_{0.8}Zn_{0.2}S$/Au/g-C_3N_4: 123 μmol h^{-1} g^{-1} (52.2×>Au/g-C_3N_4) (8.63×>CdS/Au/g-C_3N_4)	[228]
WO_3/g-C_3N_4/Ni(OH)x (20 wt% defective WO_3 and 4.8 wt% $Ni(OH)_x$)	Direct Z-scheme		100 mL Pyrex flask sealed; 300 W Xe lamp; 50 mg photocatalyst; aqueous solution (80 mL) containing 15% triethanolamine; 3 h irradiation	WO_3/g-C_3N_4/$Ni(OH)_x$: 576 μmol h^{-1} g^{-1} (5.7×> g-C_3N_4/4.8%$Ni(OH)_x$) (10.8×>20 wt.%WO_3/g-C_3N_4) (230×>g-C_3N_4)	[229]

$Pt/Ta_3N_5/WO_{2.72}$	Direct Z-scheme		homemade steel reaction cell (volume = 65 mL) with a quartz window (diameter = 6 cm); 150 W Xe lamp($\lambda \geq 420$ nm); 25 mL aqueous methanol solution (20 vol%); NaI(5×10^{-4} M); 1:1 M mixture of Ta3N5(0.02 g) and WO3(0.076 g); 6 h irradiation	$Pt/Ta_3N_5/WO_{2.72}$: ~7.7 μmol h^{-1} g^{-1} $Ta_3N_5/WO_{2.72}$: ~5.3 μmol h^{-1} g^{-1} Ta_3N_5: 2.2 μmol h^{-1} g^{-1} Pt/Ta_3N_5: 2.7 μmol h^{-1} g^{-1} (without the filter) Ta_3N_5: ~50.33 μmol h^{-1} g^{-1} $Ta_3N_5/WO_{2.72}$: ~171.56 μmol h^{-1} g^{-1} $Pt/Ta_3N_5/WO_{2.72}$: ~512.1 μmol h^{-1} g^{-1}	[230]
$Cu_2O/Au/TiO_2$ (TiO_2 to Cu_2O ratio of 34.7 wt%; Au content of 0.38 mg cm^{-2})	All-solid-state Z-scheme		photochemical electrolytic cell sealed with a silicone cap with a hydrogen sampling port; 300 W xenon lamp; 100 mL 20% (vol%) methanol aqueous solutions; composite film (5.0 cm^2); 2.5 h irradiation	Cu_2O/TiO_2 film: 83.2 mmol h^{-1} m^{-2} $Au/Cu_2O/TiO_2$: 125.3 mmol h^{-1} m^{-2} (2.2×~Au/TiO_2) (1.5×~Cu_2O/TiO_2) Au/TiO_2: 56.13 mmol h^{-1} m^{-2} Cu_2O/TiO_2: 83.2 mmol h^{-1} m^{-2}	[231]
hierarchical porous CdS/Au/N-TiO_2 (6.71 wt% CdS)	All-solid-state Z-scheme		quartz flask; 750 W Xe arc lamp($\lambda > 400$ nm); 100 mg photocatalyst; Na_2S (0.25 M)-Na_2SO_3 (0.35 M) mixed solution (100 mL); 5 h irradiation	CdS/Au/N-TiO_2: ~90 μmol h^{-1} g^{-1} AQE: 3.23% (2.6×~ N-TiO_2) (270×~ Au/N-TiO_2)	[232]
mp-CdS/$H_2Ti_3O_7$ (molar ratio of CdS to $H_2Ti_3O_7$ = 1:2)	Direct solid-state		top-irradiation Pyrex vessel; 50 mg photocatalyst; 100 mL aqueous solution containing 0.005 M Na_2S and 0.005 M Na_2SO_3; 300 W Xe lamp; 12 h irradiation	CdS/$H_2Ti_3O_7$: 1523 μmol h^{-1} g^{-1} (13×~ CdS) CdS:117 μmol h^{-1} g^{-1}	[233]
Pt/g-C_3N_4-20/ZnO nanorods (OD-ZnO) (1.0 wt% Pt; 20 wt% g-C_3N_4)	Direct Z-scheme		250 mL sealed three-necked Pyrex flask; 300 W Xenon lamp ($\lambda > 420$ nm); 100 mL of 10 vol% triethanolamine (TEOA) aqueous solution; 100 mg photocatalyst; 6 h irradiation	Pt/CN-20/OD-ZnO: 322 μmol h^{-1} g^{-1} (5×~ g-C_3N_4/Pt) g-C_3N_4/Pt: 65 μmol h^{-1} g^{-1}	[165]
CdS/ZnO	Direct Z-scheme		top-irradiation vessel; 100 mg photocatalyst; 270 mL aqueous solution of 0.1 mol L^{-1} Na_2SO_3 and 0.1 mol L^{-1} Na_2S; 300 W Xe lamp; 10 h irradiation	ZnO : 2.3 μmol h^{-1} CdS/ZnO: 58.4 μmol h^{-1} AQY = 12.94%(λ = 380 nm) CdS/OV-ZnO: 132.9 μmol h^{-1} AQY = 19.01%(λ = 380 nm)	[234]
TiO_2/WO_3/Au $HAuCl_4$: 0.3 wt% (S2), 0.45 wt% (S3)	All-solid-state Z-scheme		300 W Xe arc lamp; 50 mg photocatalyst; 45 mL deionized water and 25 mL methyl alcohol; 1 h irradiation	TiO_2/WO_3: 26.12 μmol h^{-1} TiO_2/WO_3/Au(0.45% $HAuCl_4$) UV: 165.57 μmol h^{-1} Vis : 75.64 μmol h^{-1} UV + Vis: 269.63 μmol h^{-1} Au/TiO_2 UV: 102.44 μmol h^{-1} Vis : 5.68 μmol h^{-1} UV + Vis: 173.81 μmol h^{-1}	[235]
CdS @ZnO	Direct Z-scheme		Top-irradiation quartz cell; 10 mg photocatalysts; 100 mL deionized water; 0.35 M of sodium sulfate and 0.25 M of sodium sulfide; 225 W Xenon arc lamp; 5 h irradiation	CdS @ZnO: 11.36 mmol h^{-1} g^{-1} Pt/CdS @ZnO: 71.39 mmol h^{-1} g^{-1} (4.1×> CdS/ZnO) PdS/CdS @ZnO: 98.82 mmol h^{-1} g^{-1}, (5.7×> CdS/ZnO)	[236]
ZnO_1-$CdS_{0.2}$ core–shell nanorods (molar ratio ZnO to CdS = 10:1)	Direct Z-scheme		200 mg photocatalyst; 300 mL aqueous solution of 0.1 M Na_2S and 0.1 M Na_2SO_3; 300 W Xe lamp (135 mW cm^{-2}); 10 h irradiation	1 wt% RuO_2/ZnO_1-$CdS_{0.2}$: 6.18 mmol h^{-1} g^{-1} (2.1×~ ZnO_1-$CdS_{0.2}$) ZnO_1-$CdS_{0.2}$: 2.96 mmol h^{-1} g^{-1} (T = 400 °C) (3.53×> ZnO_1-$CdS_{0.2}$, T = 300 °C) (1.54×> ZnO_1-$CdS_{0.2}$, T = 500 °C)	[237]
$W_{18}O_{49}$/g-C_3N_4	Direct Z-scheme		quartz glass vessel; aqueous solution (10 mL) containing 10 vol% triethanolamine (TEA); 300 W Xe lamp($\lambda > 420$ nm, 340 mW cm^{-2}); 5 mg photocatalyst; 1 h irradiation	30 wt%-$W_{18}O_{49}$/g-C_3N_4 :738 μmol h^{-1} g^{-1} AQE: 1.79% (λ = 400 nm) (4.5 × pure g-C_3N_4) g-C_3N_4: 164 μmol h^{-1} g^{-1} AQE: 0.47% (λ = 400 nm)	[238]
CdS/RGO/g-C_3N_4	Direct Z-scheme		20 mg photocatalyst; water(45 mL) and lactic acid (5 mL); 350-W Xe lamp coupled with IR and UV filters; 5 h irradiation	CdS/RGO/50 wt%g-C_3N_4: 676.5 μmol h^{-1} g^{-1} (AQE = 36.5%) CdS/1wt%RGO:473.4 μmol h^{-1} g^{-1} (AQE = 24.8%) CdS:112.5 μmol h^{-1} g^{-1} (AQE = 10.3%)	[239]
SiC/$BiVO_4$	Direct Z-scheme	O_2-evolution	Labsolar II system; 300 mL Pyrex reaction vessel; 50 mg photocatalysts; 100 mL deionized water containing 0.04 mol L^{-1} $FeCl_3$; 4 h reaction time	SiC/$BiVO_4$ (w/w = 1:1): 659 μmol h^{-1} g^{-1} AQE :1.04% (λ = 420 nm)	[240]
Cubic-Fe_2O_3 Octo- Fe_2O_3	IO_3^-/I^- redox reagent		UV–vis irradiation ($\lambda > 300$ nm)	Cubic-Fe_2O_3: 309.4 μmol h^{-1} g^{-1} (84×~Octo-Fe_2O_3) Octo-Fe_2O_3: 3.7 μmol h^{-1} g^{-1}	[37]

tron mediators provide a suitable environment for the electron/hole combination, facilitating the separation of photogenerated electrons and holes. Therefore, the specific photocatalytic activity depends on the influence level of aforementioned factors.

3.4.3. O_2 evolution reaction

Only minority researches have reported the O_2 evolution reaction because this process requires four electrons transfer compared with H_2 evolution requiring two electrons transfer [244]. Wang et al. [240] found the photocatalytic O_2-evolution of $BiVO_4$ was enhanced after hybridizing micro-SiC particles. SiC/$BiVO_4$ with 1:1 mass ratio of SiC to $BiVO_4$ exhibited highest oxygen evolution rate (32.9 μmol h^{-1}), which was about 3 times that of single $BiVO_4$, of which H_2PtCl_6 was used as a molecular probe to determine the electron transport path during photocatalytic O_2 evolution. Wang et al. [37] reported the effect of photocatalytic activity towards O_2 evolution with different exposed facets of α-Fe_2O_3. The photocatalytic O_2 evolution rate of α-Fe_2O_3 exposed by {0 1 2} and {1 0 4} facets reached 309.4 μmol h^{-1} g^{-1}, which was 85 times that of α-Fe_2O_3 exposed by {1 0 1} and {1 1 1} facets under the same conditions.

3.4.4. CO_2 reduction

The increasing consumption of global fossil fuels lead to the rapid growth of CO_2 concentration in the atmosphere, which has been a great concern for its effect to undesired climate change and environmental destruction. CO_2 reduction has been a promising method to reduce increasing CO_2 since the advent of photocatalysis in the 1970s [245]. However, chemical processes based on photocatalytic technology are rarely reported because of the low photon efficiency of the material [246,247]. The photoinduced reaction of H_2O and CO_2 to form hydrocarbons is currently known as a promising technology for storing solar energy in the form of chemical bonds [248]. Over the past few decades, studies based on the photocatalytic processes of CO_2 conversion have been explored. In 1979, Inoue et al. [249] first demonstrated that photocatalytic CO_2 reduction can be achieved by a variety of semiconductor photocatalyst such as CdS, ZnO, TiO_2, WO_3 and SiC. Those photocatalysts can reduce CO_2 to formic acid, formaldehyde, methanol and methane. Subsequently, continuous studies on photoreduction of CO_2 have been carried out for enhancing reduction efficiency.

Generally, the photocatalytic CO_2 conversion requires a large amount of energy input to break the C═O bond with high thermodynamic stability. In addition, Ye et al. reported that the initial step of the photocatalytic CO_2 reduction is a one-electron reduction reaction in which CO_2 was reduced to $CO_2^{\bullet-}$, followed by the break of C–O bonds and the creation of C–H bonds [250,251]. However, due to the high negative redox potential of $CO_2/CO_2^{\bullet-}$ (−1.90 V vs. NHE), one electron-involved CO_2 reduction reaction is thermodynamically infeasible. Therefore, proton-coupled multielectron reduction reaction are more preferable due to the relatively lower redox potential. As shown in Fig. 13, under visible light irradiation, the semiconductor absorbs light and the VB-electrons are excited to the CB, leaving behind holes in the VB. Because the photocatalytic CO_2 reduction is an uphill reaction, the CB bottom potential of the semiconductor should be more negative than the redox potentials of CO_2 and the oxidation potential of water. Furthermore, the bulk charge recombination rate is faster than the rate of redox reaction occurring on the surface of catalysts. Hence, the photocatalytic performance of CO_2 reduction can be improved by promoting the spatial separation efficiency of photogenerated carriers.

In Z-scheme photocatalytic system, the photogenerated electrons in the CB of one semiconductor with lower energy would combine with the holes in another semiconductor, as a result, the strongly reductive electrons and the strongly oxidative holes are respectively left in two different semiconductors. Finally, the excited electrons participate in CO_2 reduction and the holes participate in water oxidation. In this regard, the Z-scheme photocatalytic system with charge transfer along the pathway similar to the letter "Z" preserves the strong reduction ability of electrons, which is quite beneficial for the reduction of CO_2.

At present, the studies on photocatalytic CO_2 reduction based on Z-scheme photocatalytic system have aroused widespread concern. For instance, Wang et al. prepared α-Fe_2O_3/Cu_2O composites with enhanced photocatalytic performance in CO_2 reduction [252]. An inner electrical field with the direction from Fe_2O_3 to Cu_2O was established at the contact interface, which make the photogenerated electrons in the CB of Fe_2O_3 transfer to the VB of Cu_2O and combine with the holes therein. As a result, the excited electrons with more negative potential would reduce CO_2 to its reduced-products, while the holes react with water to generate **.**OH species followed by the generation of O_2. Bae and his co-worker [253] synthesized ZnO-Cu_2O nanocatalysts by growing Cu_2O single-crystalline nanocubes on the surface of ZnO, achieving selective reduction of CO_2 to generate CH_4. The optimal CH_4 production of 1080 μmol g_{cat}^{-1} h^{-1} over ZnO-Cu_2O was 71 times and 5 times higher than that of pure ZnO and Cu_2O, respectively. The enhanced photocatalytic reduction efficiency was attribute to the suitable band structure in ZnO-Cu_2O, the VB-hole potential of ZnO is positive enough to oxidize H_2O and the CB-electron potential is negative to reduce CO_2. Besides, Cu_2O mainly exposed (1 0 0) facets with less defect in ZnO-Cu_2O composite, which facilitate the charge transfer from semiconductor to the reagents. Moreover, the high surface area produced by the colloidal dispersion is beneficial to the adsorption of CO_2 to specific crystal faces of Cu_2O, resulting in an optimal photocatalytic performance. A similar Z-scheme mechanism is also proposed in SnO_{2-x}/g-C_3N_4 [254], g-C_3N_4/WO_3 [106], CdS/WO_3 [255], α-Fe_2O_3/g-C_3N_4 [256].

Besides the direct Z-scheme, the charge separation can also achieve by electron mediator such as metals or graphene species. For example, the all solid state Z-scheme photocatalysts 3DOM Pt@CdS/TiO_2 were prepared by dispersing core-shell Pt@CdS nanoparticles on the surface of three-dimensionally ordered macroporous (3DOM) TiO_2 [257]. The photogenerated electrons in the CB of TiO_2 transfer to metallic Pt and then flow into the CdS, followed by combining with the holes therein. As a result, the strongly oxidative VB-holes of TiO_2 react with adsorbed water to generate O_2 and H^+, while the strongly reductive CB-electrons of CdS reduce CO_2 to CH_4 with the participation of H^+ protons (Fig. 14a). Moreover, 3DOM TiO_2 with highly ordered macroporous structures can promote the light absorption efficiency. Hence, the photocatalytic performance for CO_2 reduction was greatly improved. Furthermore, an efficient photocatalyst CdS/rGO/TiO_2 for CO_2 conversion was reported by Kuai et al., wherein rGO functioned as recombination center of the CB-electrons of TiO_2 and the VB-holes of CdS [258]. Such electron flow mechanism make CB-electrons of CdS with strong reduction react with CO_2 to generate CH_4, which also inhibited the photocorrosion of CdS (Fig. 14b). Li et al. [259] designed $Fe_2V_4O_{13}$/RGO/CdS composite for photocatalytic conversion of CO_2 into CH_4. RGO, which is an intermediate layer between CdS and $Fe_2V_4O_{13}$, has a high-speed charge transfer channel that improves charge separation efficiency while protecting CdS from photocorrosion. Besides, the visible light absorption region is greatly enhanced after coupling with CdS nanoparticles, endowing the $Fe_2V_4O_{13}$/RGO/CdS composite more efficient solar energy utilization. Simultaneously, the charge transfer follows the Z-scheme mechanism is also facilitate the separation of photogenerated electron-hole pairs. The photogenerated electrons in the CB of CdS would transfer to RGO, followed by flowing into the VB of $Fe_2V_4O_{13}$ and combine with the holes therein. As a result, the

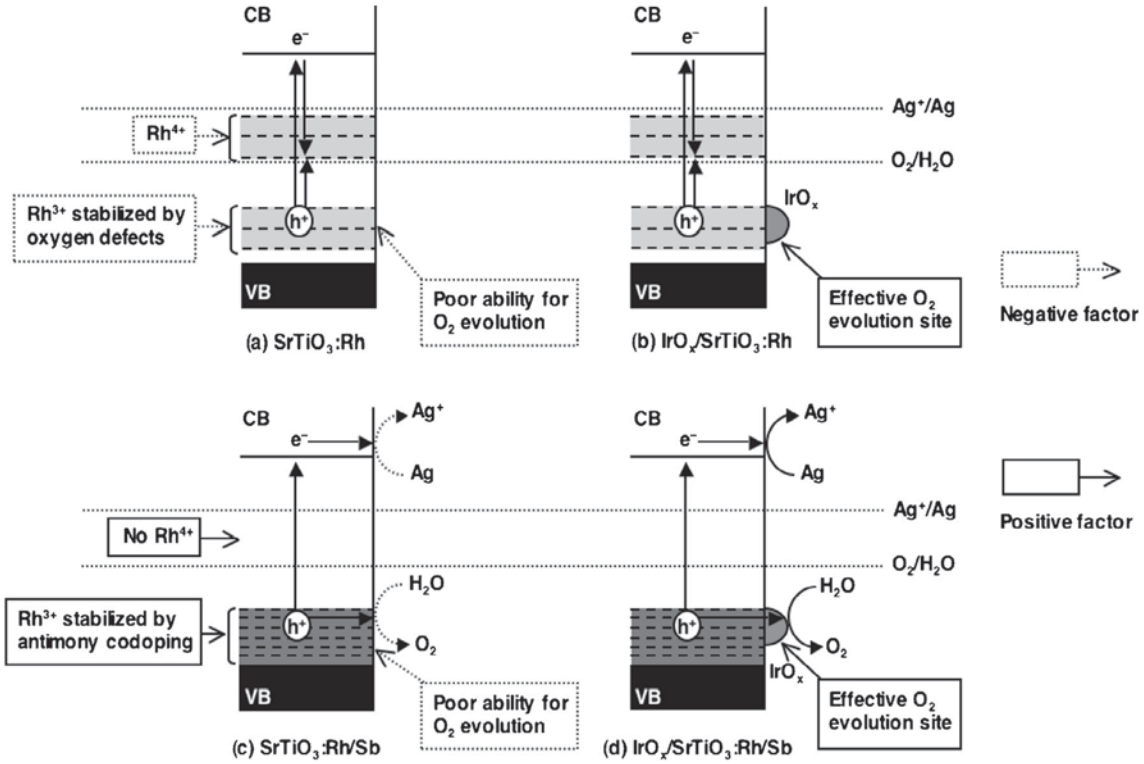

Fig. 12. Proposed scheme of photocatalytic O_2 evolution over $SrTiO_3$: Rh/Sb under visible light irradiation. Adapted and reprinted with permission from Ref. [215], Copyright 2014 Elsevier.

strongly reductive electrons in CB of $Fe_2V_4O_{13}$ participate in the photocatalytic reduction reaction of CO_2 and the strongly oxidative holes in the VB of CdS can oxidize H_2O to O_2.

Compare with single semiconductor photocatalyst, heterojunction composed of different semiconductors can achieve enhanced light responsive region and charge separation efficiency. Compared with type II heterojunction, the most prominent advantage of Z-scheme is the realization of vector electron transfer, in which the electrons with relatively low energy of one semiconductor combine with the holes of another semiconductor, resulting in a more efficiency charge separation. Therefore, a Z-scheme photocatalytic system can not only achieve an efficient charge spatial separation but also remain strongly reductive electrons to participate in the CO_2 photoreduction, which is a very good idea to improve the efficiency of CO_2 photoreduction. As shown in Table 6, the latest studies about the photoreduction of CO_2 based on Z-scheme photocatalysts are evaluated.

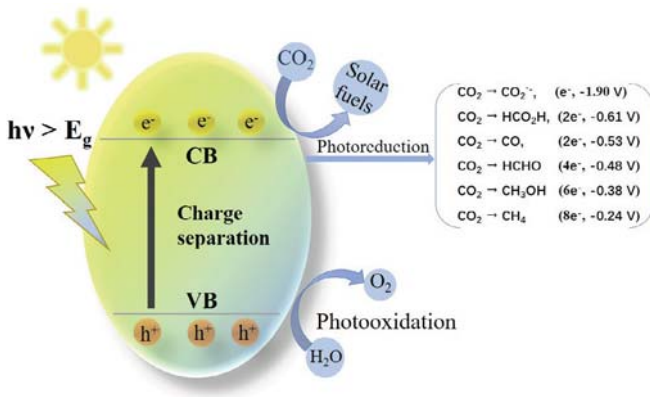

Fig. 13. Schematic illustration of probable mechanism of photocatalytic CO_2 conversion over a semiconductor photocatalyst.

Table 6 list part of the studies reported in the literature, including the reaction conditions, major product and its yield. In addition, we also discussed the design of photoreactors. For instance, Yu et al. [268] designed a dual-function photocatalyst system with IO_3^-/I^- incorporated for the first time to balance charge, which combine water-splitting and CO_2 photo-hydrogenation. GaN: ZnO-Ni/NiO photocatalysts reduce CO_2 while Pt/WO_3 photocatalysts simultaneously produce O_2 in each chamber of a twin photoreactor, the results showed that the twin photoreactor could significantly promote the photoreduction quantum efficiency (PQE) more than 4 times from 0.015% to 0.070% compared to a single photoreactor. Additionally, the selectivity for CO_2 reduction in the twin photoreactor reached 99.1%, which was higher than that in the single photoreactor (73.6%). Currently, a twin photoreactor [269] offers several advantages over other systems: (1) It blocks the backward reaction because H_2 and O_2 are generated separately; (2) It hinders the oxidation of hydrocarbon products because O_2 from water splitting is effectively isolated from CO_2 hydrogenation, which is also thermodynamically favorable; and (3) It provides sustainable operation because H_2 generated from water splitting is directly applied to CO_2 hydrogenation. The advantages of the Z-scheme and H-type reactor systems were combined in this novel twin photoreactor system, which has great potential for water conversion to solar energy. However, their efficiency is still relatively low and far away from the benchmark photo-conversion efficiency for commercialization, it is necessary to establish a model simulating the performance of photoreactors to systematically study the photocatalytic reduction of CO_2, achieving higher photo-conversion efficiency. When constructing photocatalytic reactors, not only mass transfer should be considered, the reactor should

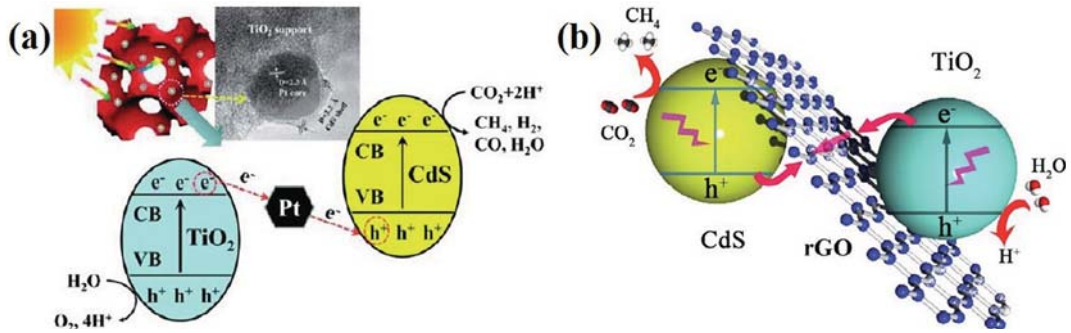

Fig. 14. (a) Schematic of the charge separation mechanism for the photoreduction of CO_2 with H_2O over 3DOM Pt@CdS/TiO_2 heterojunction catalysts. Figure reproduced with permission from Ref. [257]. Copyright 2015 The Royal Society of Chemistry. (b) Schematic illustration of photocatalytic conversion of CO_2 into CH_4 over CdS NSs/rGO/TiO_2 Z-scheme system. Figure reproduced with permission from Ref. [258]. Copyright 2015 The Royal Society of Chemistry.

also be designed to allow the catalytic active sites to be exposed to as much light as possible. Especially in slurry reactors, the scattering properties largely depend on the agglomeration phenomenon, which will affect the reaction rate. Coated catalysts in the reactor can greatly reduce the effect of scattering behavior [270]. However, how to optimize coatings to produce suitable agglomerate size and porosity to reduce scattering behavior still need to further study.

The present study has demonstrated that CO_2 is a promising and powerful alternative for the production of renewable fuels and commodity chemicals. Technology for the catalytic hydrogenation of CO_2 to CH_3OH is the most expected since it can not only replace fossil fuels also can be the source of hydrogen. Theoretically, H_2 sources for the production of CH_3OH/CH_4 from CO_2 should be sustainable. To some extent, H_2O would be the best source. However, how to activate two stable molecules (CO_2 and CO_2) into unstable molecules and not consume too much energy still need further exploration. We should first understand the reaction mechanism and optimize the product. Additionally, it is difficult to compare the photocatalytic performance because the final productivity largely depended on the experimental conditions including the type of light, pH of the solution and CO_2 pressure. Few papers report the quantum yield or efficiency because the quantity of photons absorbed by the photocatalysts is difficult to measure.

For water splitting and CO_2 reduction accompanied with water oxidation, the CB-edge potential of photocatalyst should be more negative than the redox potential of H_2O/H_2 or CO_2/CH_4 (CO_2/CH_3OH, $CO_2/CHOOH$ or CO_2/CO), the VB-edge potential should be more positive than that of the redox potential of H_2O/O_2, which seems to be more difficult to achieve than other photocatalytic reactions. As long as the active species is present in the reaction system, whether it is $\cdot O_2^-$ ($O_2/\cdot O_2^-$, −0.33 V vs. NHE), ·OH ($OH^-/\cdot OH$) or h^+ can participate in the oxidation reaction of pollutant degradation. However, in order to achieve photocatalytic CO_2 reduction, it is not enough that the photocatalyst with suitable band structure can be excited to generate electron-hole under light irradiation. Due to the redox potential of CO_2/CO_2^- of −1.90 V is relative negative, one-electron CO_2 reduction is not thermodynamically unfavorable. The proton-coupled multielectron CO_2 reduction is relative easy to carry out due to the lower redox potential of its reduced-products. Hence, a highly efficient photocatalyst that used to reduce CO_2 should be easily excited to produce multiple electrons and those generated electron can easily transfer to CO_2. Besides, the CB bottom potential of catalyst should be more negative enough to reduce CO_2. In order to reduce the possibility of bulk charge recombination, holes should be trapped by the oxide species.

Photocatalytic water splitting to O_2 and H_2 by catalysts is a promising method for obtaining chemical energy from solar energy, which is uphill reaction of Gibbs energy of 237.13 kJ mol^{-1}. In order to realize water splitting, the CB bottom potential of photocatalysts should be more negative than the redox potential of H_2O/H_2 (−0.41 V vs NHE) and the VB top potential should be more positive than the redox potential of H_2O/O_2 (−0.82 V vs NHE). Although photocatalytic water splitting based on Z-scheme photocatalytic system have been achieved about ten years ago, some challenges still need to be overcome. The determining step of water splitting in Z-scheme system is water reduction, thereby how to improve the rate of H_2 evolution is a critical step for further enhancing photocatalytic performance. Additionally, due to the backward reactions of redox-mediator Z-scheme system, constructing redox mediator-free Z-scheme system is a promising development direction to achieve maximum photocatalytic performance. However, exploring new cocatalysts that facilitate forward reactions but suppress backward reactions and the recombination of H_2-O_2 remains a critical challenge. Building a Z-scheme photocatalyst with a wider range of visible light response for a higher apparent quantum yield is another current challenge.

In order to overcome these problems to maximize the efficiency of water splitting and CO_2 photoreduction, enormous effort should be made according to the following. Firstly, exploring advanced photocatalysts that can prevent the bulk charge recombination and improve light-harvesting efficiency is crucial for water splitting and CO_2 photoreduction, such as bandgap engineering, crystal facet engineering as well as surface heterojunction. Next, optimizing the adsorbing amount and state of CO_2 and H_2O on the surface of catalysts can improve the photocatalytic performance of water splitting and CO_2 reduction in both thermodynamics and kinetics. Finally, a fundamental research based on theoretical and experimental analysis is necessary for understanding the photocatalytic mechanism, which facilitates further optimize the facets, surface and phases of semiconductor for maximum photocatalytic efficiency.

4. Summary and future prospects

As a promising candidate technology, photocatalysis can effectively degrade various pollutants and convert solar energy into sustainable chemical energy, which has been extensively explored to alleviate environmental pollution and global energy crisis. The artificial multi-component Z-scheme photocatalytic system, which can effectively promote the separation of electron-hole pairs, has better photocatalytic performance than a single photocatalyst or even Type II heterojunction photocatalyst. The present studies provide the basic review of recent significant publications about the application of Z-scheme nanocomposite photocatalysts in environmental restoration and energy conversion, including photodegra-

Table 6
Photoreduction of CO_2 based on Z-scheme photocatalysts.

Photocatalyst	CO_2 photoreactor	Irradiation source	Electron transfer	Major product	Products and Yields	Ref.
α-Fe_2O_3/Cu_2O	0.10 g of photocatalyst; 10 mL of deionized water; CO_2 pressure, 0.3 MPa; stainless steel cylindrical reactor;	300 W xenon arc lamp (λ > 400 nm)	Direct Z-scheme	CO	CO: 1.67 μmol $g_{cat}^{-1}h^{-1}$	[252]
ZnO-Cu_2O	photocatalyst, 0.019 g; CO_2 pressure, 2.6 bar; 20 mL of CO_2-saturated 0.2 M Na_2CO_3; homemade quartz flask with a total volume of 41 mL, pH = 7.4,	300 W Xe lamp (λ > 200 nm)	Direct Z-scheme	CH_4	CH_4: 1080 μmol $g_{cat}^{-1}h^{-1}$ (71× > ZnO) (5× > Cu_2O)	[253]
g-C_3N_4/WO_3	photocatalyst, 0.025 g; CO_2 pressure, 0.1 MPa; $NaHCO_3$ (1.712 g), H_2SO_4 (5 mL, 4 M); reaction temperature, 20 °C; 500 mL PLS-SXE300 Labsolar-IIIAG closed gas system	300 W Xe lamp (λ > 420 nm) (0.21 W cm^{-2})	Direct Z-scheme	CO	CO: 27.2 μmol $g^{-1}h^{-1}$ (2.2× > g-C_3N_4)	[254]
CdS/WO_3	photocatalyst, 0.025 g; CO_2 pressure, 0.1 MPa; $NaHCO_3$ (1.712 g), H_2SO_4 (5 mL, 4 M); reaction temperature, 20 °C; 500 mL PLS-SXE300 Labsolar-IIIAG closed gas system	300 W Xe lamp (λ > 420 nm) (0.21 W cm^{-2})	Direct Z-scheme	CO	CO: 27.2 μmol $g^{-1}h^{-1}$ (2.2× > g-C_3N_4)	[255]
α-Fe_2O_3/ g-C_3N_4	photocatalyst, 0.025 g; CO_2 pressure, 0.1 MPa; $NaHCO_3$ (1.712 g), H_2SO_4 (5 mL, 4 M); reaction temperature, 20 °C; 500 mL PLS-SXE300 Labsolar-IIIAG closed gas system	300 W Xe lamp (λ > 420 nm) (0.21 W cm^{-2})	Direct Z-scheme	CO	CO: 27.2 μmol $g^{-1}h^{-1}$ (2.2× > g-C_3N_4)	[256]
3DOM Pt@CdS/TiO_2	0.02 g of catalyst; CO_2 pressure, 0.1 MPa; H_2O, 1.0 mL; reaction temperature, 20 °C; gas-closed circulation system	300 W Xe lamp (320 < λ < 780 nm)	All-solid-state Z-scheme	CH_4	CH_4: 36.8 μmol $g^{-1}h^{-1}$; (24 × > 3DOM TiO_2) (26× > 3DOM CdS/TiO_2) (7× > Pt/TiO_2)	[257]
CdS/rGO/TiO_2	0.02 g of catalyst; CO_2 pressure, 0.1 MPa; H_2O, 0.4 mL; reaction temperature, 20 °C; gas-tight reaction system	300 W Xe lamp	All-solid-state Z-scheme	CH_4	CH_4: 0.1176 μmol $g^{-1}h^{-1}$; (4 × > CdS/TiO_2) (3× > CdS/rGO) (5.6× > CdS)	[258]
$Fe_2V_4O_{13}$/RGO/CdS	gas-tight system; photocatalyst, 0.025 g; CO_2 pressure, 1 atm; 0.4 mL of deionized water;	300 W Xe lamp	All-solid-state Z-scheme	CH_4	CH_4: 2.25 μmol $g^{-1}h^{-1}$; (1.4 × > $Fe_2V_4O_{13}$/CdS) (4× > $Fe_2V_4O_{13}$)	[259]
g-C_3N_4/11.4 wt.%$Bi_4O_5I_2$	photocatalyst, 0.1 g; CO_2 pressure, 1 atm; reaction temperature, 15 °C; Lab solar-III AG closed gas system,	300 W high pressure xenon lamp (λ > 400 nm)	I_3^-/I^- redox mediator	CO	CO: 45.6 μmol $g^{-1}h^{-1}$ (7.9× > g-C_3N_4) (2.3× > 11.4 wt.%$Bi_4O_5I_2$)	[260]
TiO_2/Au@CdS	photocatalyst, 0.02 g; CO_2 pressure, 0.1 MPa; H_2O, 1 mL; reaction temperature, 20 °C; gas-closed circulation system	300 W Xe lamp (320 < λ < 780 nm) (100 mW cm^{-2})	All-solid-state Z-scheme	CH_4	CH_4: 41.6 μmol $g^{-1}h^{-1}$ (26× > IO-TiO_2-195) (23× > CdS/IO-TiO_2) (8× > Au/IO-TiO_2) CO (0.6 μmol $g^{-1}h^{-1}$), (5× < IO-TiO_2-195) (7× < CdS/IO-TiO_2) (3× > Au/IO-TiO_2)	[261]
g-C_3N_4/BiOBr/Au-B	Lab solar-III AG closed gas system; photocatalyst, 0.1 g; CO_2 pressure, 1 atm;	300 W high-pressure xenon lamp	All-solid-state Z-scheme	CO	CO: 6.67 μmol $g^{-1}h^{-1}$; (2.5× > g-C_3N_4/BiOBr/Au-S) (2.67× > g-C_3N_4/BiOBr) CH_4: 0.92 μmol $g^{-1}h^{-1}$ (1.7× > g-C_3N_4/BiOBr/Au-S) (2× > g-C_3N_4/BiOBr)	[60]
g-C_3N_4/SnS_2	200 mL homemade Pyrex reactor with two openings at ambient temperature and atmospheric pressure	300 W Xe light (λ ≥ 420 nm),	Direct Z-scheme	CH_3OH	CH_3OH: 2.3 μmol $g^{-1}h^{-1}$ (2× ≈ g-C_3N_4; 3× ≈ SnS_2) CH_4: 0.64 μmol $g^{-1}h^{-1}$	[262]
30 wt%Cu_2ZnSnS_4/ZnO	A gaseous phase reactor arrangement	100 W xenon solar simulator with an AM 1.5 filter	Direct Z-scheme	CH_4	CH_4(138.90 ppm $g^{-1}h^{-1}$) (31× > unsensitized ZnO) (22× > Cu_2ZnSnS_4) AQE: 0.0128%	[263]
$ZnFe_2O_4$/TiO_2	50 mL cylindrical slurry reactor system at ambient temperature and pressure, photocatalyst, 0.01 g; reaction temperature, 25 °C;	250 W high pressure mercury lamp (360 nm, 3.2 mW cm^{-2})	Direct Z-scheme	cyclohexanone (CH), cyclohexyl formate (CF)	CH: 21.28 μmol $g_{cat}^{-1}h^{-1}$ CF: 22.26 μmol $g_{cat}^{-1}h^{-1}$	[264]
WO_3/g-C_3N_4	photocatalyst, 3 mg; CO_2 pressure, 1 atm; H_2O, 5.0 mL; reaction temperature, 24 °C;	light-emitting diode (435 nm, 3.0 mW cm^{-2})	Direct Z-scheme	CH_3OH	CH_3OH (2.4× > g-C_3N_4)	[254]
42.2 wt% SnO_{2-x}/ g-C_3N_4	a stainless steel reactor with a quartz window on the top of the reactor; photocatalyst, 0.02 g; CO_2 pressure, 0.3 MPa; H_2O, 4.0 mL; reaction temperature, 80 °C; gas-closed circulation system	500 W Xe lamp	Direct Z-scheme	CO	CO + CH_3OH + CH_4: 22.7 μmol $g_{cat}^{-1}h^{-1}$ (4.3× > g-C_3N_4) (5× > P25)	[105]
Cu_2O/TiO_2	a 135 cm^3 customized quartz photoreactor with flat circular windows (diameter = 5.08 cm); photocatalyst, 0.03 g; CO_2 pressure, 1 atm; reaction temperature, 20 °C;	1 kW high-pressure Hg (Xe) arc lamp (305 ≤ λ ≤ 665 nm)	Direct Z-scheme	CO	CO:0.55 μmol $g_{cat}^{-1}h^{-1}$ (4.0× > Cu_2O)	[265]
Al-O bridged g-C_3N_4/ α-Fe_2O_3	A cylindrical steel reactor with 100 mL volume and 3.5 cm^2 area; photocatalyst, 20 mg; CO_2 pressure, 1 atm; H_2O, 5.0 mL	300 W Xenon arc lamp	Direct Z-scheme	CO	CO:24 μmol $g^{-1}h^{-1}$ (4.0× > α-Fe_2O_3) CH_4: 3.1 μmol h^{-1} g^{-1} (10.0× > α-Fe_2O_3)	[256]

(*continued on next page*)

Table 6 (*continued*)

Photocatalyst	CO_2 photoreactor	Irradiation source	Electron transfer	Major product	Products and Yields	Ref.
AgBr/g-C_3N_4	150 mL cylindrical glass reactor equipped with a UV illumination source located in the quartz immersion tube; photocatalyst, 0.1 g	300 W xenon lamp (270 mW cm^{-2})	Direct Z-scheme	CH_4	CH_4: 61.52 μmol g^{-1} (3.59×> AgBr) (2.86×> g-C_3N_4) CH_3COCH_3: 3.32 μmol g^{-1}	[266]
3D $ZnIn_2S_4/TiO_2$	photocatalytic reduction of CO_2	300 W xenon lamp	Direct Z-scheme	CH_4	CH_4:1.135 μmol $g^{-1}h^{-1}$ (39×> $ZnIn_2S4_4$)	[267]

dation of organic pollutants, photocatalytic CO_2 reduction, water splitting, photocatalytic H_2/O_2 evolution, heavy metal reduction and photocatalytic disinfection. Simultaneously, the photogenerated charge carrier migration process and photocatalytic reaction pathways of key aspects of Z-scheme photocatalysts are discussed. It is an on-going process to search for Z-scheme photocatalysts for practical applications in the environment and energy. Up to now, quite a lot of Z-scheme photocatalysts have showed a promising photocatalytic performance in the above applications. They will continue to attract research attention until breakthrough discoveries are available for large-scale applications.

Despite considerable photocatalytic results have obtained based on the Z-scheme photocatalytic materials, there are still some critical and inspiring topics to be investigated. Rational design of Z-scheme photocatalysts that simultaneously possess effective visible light absorption, low charge carrier transfer resistance, good physical and chemical stability are critical steps for large-scale applications. Because the redox-mediator Z-scheme photocatalytic system can only work in the liquid-phase, thus constructing Z-scheme photocatalytic system without redox mediator would be a promising strategy for its widespread application, in which geometric configuration is a critical factor that influence the photocatalytic performance of Z-scheme photocatalytic performance. Specifically, for all-solid-state Z-scheme photocatalytic system, the light absorption capacity and charge spatial separation efficiency are largely depended on the crystal structures, spatial distribution as well as the morphologies of the components, thereby the photocatalytic performance can be improved by optimizing the geometric configuration. For direct Z-scheme photocatalytic system, optimizing the geometric configuration to increase the effective contact interface area and balance the distribution of incident photons between two components.

Moreover, an efficient Z-scheme photocatalysts often require a relatively narrow band gap to expand available light spectra, and simultaneously, the developed Z-scheme photocatalysts should generated as many charge carriers with appropriate energy levels as possible to perform a specific photocatalytic redox process. Besides, due to the charge carrier migration at the surface of Z-scheme photocatalysts largely depends on the energy band bending of semiconductors, so that the adjustment of energy band structures of PS II and PS I is important. Generally, built-in electric fields formed at the interface between semiconductors facilitate the separation of electron-hole pairs. However, the dynamics of carriers can only be promoted when the direction of photogenerated charge carrier migration coincides with the direction of the built-in electric field. Therefore, it is an exciting insight to introduce the external electric field induced by polarization to change the band structure of semiconductors. Additionally, the intensity of the internal electric field and its orientation can be changed under different polarization conditions, so that the electron transfer direction in the Z-scheme photocatalyst can be controlled by downward band bending from PS II to PS I. Also, depositing suitable reduction and oxidation co-catalysts respectively on reduction and oxidation active sites are also ideal methods to further enhance the separation efficiency of electron-hole, thereby optimizing the photocatalytic performance of photocatalysts.

The charge carrier migration at the surface of two semiconductor also affected by the crystal structure such as defects, lattice parameters and so forth. Optimizing the interface properties of semiconductors is also an efficient method to improve the photocatalytic performance of Z-scheme photocatalysts. What's more, theoretical material simulation based on first-principles density functional (DFT) combined with various characterization methods might be a promising method for in depth understanding the reaction pathway of Z-scheme photocatalysts.

While focusing on practical applications, Z-scheme with low-cost, high yield and environmentally-friendly is a prerequisite for its practical application. It is also worth considering whether the excellent photocatalytic performance of the Z-scheme photocatalyst can be maintained in the industrial process. Separation efficiency of materials is also one of the key factors affecting its practical application. A possible approach is to grow these materials on a functional substrate such as polymeric or inorganic membrane to achieve a synergy between photocatalytic reaction and effective separation.

Despite the challenges, it is undeniable in the scientific community that Z-scheme photocatalysts have potential advantages in energy conversion and environmental purification. It is hoped that this review will motivate researchers to fully utilize the photocatalytic potential of the Z-scheme photocatalysts through theoretical calculations and experiments.

Acknowledgements

This study was financially supported by the Program for the National Natural Science Foundation of China (51879101, 51579098, 51779090, 51709101, 51521006, 51809090, 51278176, 51378190), the National Program for Support of Top–Notch Young Professionals of China (2014), the Program for Changjiang Scholars and Innovative Research Team in University (IRT-13R17), and Hunan Provincial Science and Technology Plan Project (2018SK20410, 2017SK2243, 2016RS3026), and the Fundamental Research Funds for the Central Universities (531109200027, 531107051080, 531107050978).

References

[1] X. Liu, D. Huang, C. Lai, G. Zeng, L. Qin, C. Zhang, H. Yi, B. Li, R. Deng, S. Liu, Y. Zhang, Recent advances in sensors for tetracycline antibiotics and their applications, Trends Anal. Chem. 109 (2018) 260–274.
[2] A. Kudo, Y. Miseki, Heterogeneous photocatalyst materials for water splitting, Chem. Soc. Rev. 38 (2009) 253–278.
[3] K. Sayama, K. Mukasa, R. Abe, Y. Abe, H. Arakawa, A new photocatalytic water splitting system under visible light irradiation mimicking a Z-scheme mechanism in photosynthesis, J. Photoch. Photobio. A 148 (2002) 71–77.
[4] H. Kato, Y. Sasaki, A. Iwase, A. Kudo, Role of iron ion electron mediator on photocatalytic overall water splitting under visible light irradiation using Z-scheme systems, B. Chem. Soc. JPN. 80 (2007) 2457–2464.

[5] F. Xiao, B. Liu, In-situ etching-induced self-assembly of metal clusters decorated one-dimensional semiconductor for solar-powered water splitting: unraveling cooperative synergy by photoelectrochemical investigations, Nanoscale 9 (2017) 17118–17132.
[6] F. Kan, T. Ohno, M. Matsumura, Splitting of water by electrochemical combination of two photocatalytic reactions on TiO_2 particles, J. Chem. Soc. Faraday Trans. 94 (1998) 3705–3709.
[7] J.A. Christians, R.C. Fung, P.V. Kamat, An inorganic hole conductor for organo-lead halide perovskite solar cells. Improved hole conductivity with copper iodide, J. Am. Chem. Soc. 136 (2014) 758–764.
[8] Q. Zhang, E. Uchaker, S.L. Candelaria, G. Cao, Nanomaterials for energy conversion and storage, Chem. Soc. Rev. 42 (2013) 3127–3171.
[9] Z. Zeng, F. Xiao, H. Phan, S. Chen, Z. Yu, R. Wang, T.Q. Nguyenc, T.T.Y. Tan, Unraveling the cooperative synergy of zero-dimensional graphene quantum dots and metal nanocrystals enabled by layer-by-layer assembly, J. Mater. Chem. A 6 (2018) 1700–1713.
[10] D. Huang, X. Yan, M. Yan, G. Zeng, C. Zhou, J. Wan, M. Cheng, W. Xue, Graphitic carbon nitride-based heterojunction photoactive nanocomposites: applications and mechanism insight, ACS Appl. Mater. Interfaces 10 (2018) 21035–21055.
[11] O. Ishitani, C. Inoue, Y. Suzuki, T. Ibusuki, Photocatalytic reduction of carbon dioxide to methane and acetic acid by an aqueous suspension of metal-deposited TiO_2, J. Photoch. Photobiol. A 72 (1993) 269–271.
[12] S. Sato, T. Arai, T. Morikawa, K. Uemura, T.M. Suzuki, H. Tanaka, T. Kajino, Selective CO_2 conversion to formate conjugated with H_2O oxidation utilizing semiconductor/complex hybrid photocatalysts, J. Am. Chem. Soc. 133 (2011) 15240–15243.
[13] A. Fujishima, K. Honda, Electrochemical photolysis of water at a semiconductor electrode, Nature 238 (1972) 37–38.
[14] M.A. Fox, M.T. Dulay, Heterogeneous photocatalysis, Chem. Rev. 146 (1985) 457–489.
[15] S. Ida, A. Takashiba, S. Koga, H. Hagiwara, T. Ishihara, Potential gradient and photocatalytic activity of an ultrathin p-n junction surface prepared with two-dimensional semiconducting nanocrystals, J. Amer. Chem. Soc. 136 (2014) 1872–1878.
[16] D. Huang, Z. Li, G. Zeng, C. Zhou, W. Xue, X. Gong, X. Yan, S. Chen, W. Wang, M. Cheng, Megamerger in photocatalytic field: 2D g-C_3N_4 nanosheets serve as support of 0D nanomaterials for improving photocatalytic performance, Appl. Catal. B: Environ. 240 (2019) 153–173.
[17] W. Xue, D. Huang, G. Zeng, J. Wan, M. Cheng, C. Zhang, C. Hu, J. Li, Performance and toxicity assessment of nanoscale zero valent iron particles in the remediation of contaminated soil: a review, Chemosphere 210 (2018) 1145–1156.
[18] L.G. Devi, R. Kavitha, A review on non-metal ion doped titania for the photocatalytic degradation of organic pollutants under UV/solar light: Role of photo-generated charge carrier dynamics in enhancing the activity, Appl. Catal. B: Environ. 140–141 (2013) 559–587.
[19] X. Gong, D. Huang, Y. Liu, Z. Peng, G. Zeng, P. Xu, M. Cheng, R. Wang, J. Wan, Remediation of contaminated soils by biotechnology with nanomaterials: bio-behavior, applications, and perspectives, Crit. Rev. Biotechnol. 38 (2018) 455–468.
[20] R. Abe, T. Takata, H. Sugihara, K. Domen, Photocatalytic overall water splitting under visible light by TaON and WO3 with an IO^{3-}/I^- shuttle redox mediator, Chem. Commun. 30 (2005) 3829–3831.
[21] X. Gong, D. Huang, Y. Liu, G. Zeng, R. Wang, J. Wan, C. Zhang, M. Cheng, X. Qin, W. Xue, Stabilized nanoscale zerovalent iron mediated cadmium accumulation and oxidative damage of *Boehmeria nivea* (L.) Gaudich cultivated in cadmium contaminated sediments, Environ. Sci. Technol. 51 (2017) 11308–11316.
[22] Y. Sasaki, H. Nemoto, K. Saito, A. Kudo, Solar water splitting using powdered photocatalysts driven by S-schematic interparticle electron transfer without an electron mediator, J. Phys. Chem. C 113 (2009) 17536–17542.
[23] W. Xue, Z. Peng, D. Huang, G. Zeng, J. Wan, R. Xu, M. Cheng, C. Zhang, D. Jiang, Z. Hu, Nanoremediation of cadmium contaminated river sediments: microbial response and organic carbon changes, J. Hazard. Mater. 359 (2018) 290–299.
[24] Z. Zeng, Y. Li, S. Chen, P. Chen, F. Xiao, Insight into the charge transport correlation in Aux clusters and graphene quantum dots deposited on TiO_2 nanotubes for photoelectrochemical oxygen evolution, J. Mater. Chem. A 6 (2018) 11154–11162.
[25] W. Tang, H. An, Photocatalytic degradation kinetics and mechanism of acid blue 40 by TiO_2 UV in aqueous solution, Chemosphere 31 (1995) 4171–4183.
[26] C. Zhou, C. Lai, D. Huang, G. Zeng, C. Zhang, M. Cheng, L. Hu, J. Wan, W. Xiong, M. Wen, Highly porous carbon nitride by supramolecular preassembly of monomers for photocatalytic removal of sulfamethazine under visible light driven, Appl. Catal. B: Environ. 220 (2018) 202–210.
[27] L. Spanhel, H. Weller, A. Henglein, Photochemistry of semiconductor colloids. 22. Electron ejection from illuminated cadmium sulfide into attached titanium and zinc oxide particles, J. Amer. Chem. Soc. 109 (1987) 1–6.
[28] S.J.A. Moniz, S.A. Shevlin, D.J. Martin, Z.X. Guo, J. Tang, Visible-light driven heterojunction photocatalysts for water splitting-a critical review, Energy. Environ. Sci. 8 (2015) 731–759.
[29] K. Sayama, K. Mukasa, R. Abe, H. Arakawa, Stoichiometric water splitting into H2 and O2 using a mixture of two different photocatalysts and an IO^{3-}/I^- shuttle redox mediator under visible light irradiation, Chem. Commun. 23 (2001) 2416–2417.
[30] R. Hill, F. Bendall, Function of the two cytochrome components in chloroplasts: a working hypothesis, Nature 186 (1960) 136–137.
[31] D.A. Walker, The Z-scheme down-hill all the way, Trends Plant Sci. 7 (2002) 183–185.
[32] J. Barber, Short-circuiting the Z-scheme, Nature 376 (1995) 388–389.
[33] M. Gratzel, Photoelectrochemical cells, Nature 414 (2001) 388–389.
[34] P. Zhou, J. Yu, M. Jaroniec, All-solid-state Z-scheme photocatalytic systems, Adv. Mater. 26 (2014) 4920–4935.
[35] J. Low, C. Jiang, B. Cheng, S. Wageh, A.A. Al-Ghamdi, A review of direct Z-scheme photocatalysts, Small Methods 1 (2017) 1700080–1700101.
[36] A.J. Bard, Photoelectrochemistry and heterogeneous photocatalysis at semiconductors, J. Photochem. 10 (1979) 59–75.
[37] Y. Wang, Y. Li, X. Wang, Y. Hou, A. Chen, H. Yang, Effects of redox mediators on α-Fe_2O_3, exposed by 012 and 104 facets for photocatalytic water oxidation, Appl. Catal. B: Environ. 206 (2017) 216–220.
[38] J. Yan, H. Wu, H. Chen, Y. Zhang, F. Zhang, S.F. Liu, Fabrication of TiO_2/C_3N_4 heterostructure for enhanced photocatalytic Z-scheme overall water splitting, Appl. Catal. B: Environ. 191 (2016) 130–137.
[39] K. Sayama, R. Abe, H. Arakawa, H. Sugihara, Decomposition of water into H and O by a two-step photoexcitation reaction over a Pt-TiO_2 photocatalyst in $NaNO_3$ and $NaCO_3$ aqueous solution, Catal. Commun. 7 (2006) 96–99.
[40] Y. Sasaki, H. Kato, A. Kudo, $[Co(bpy)^3]^{3+/2+}$ and $[Co(phen)^3]^{3+/2+}$ electron mediators for overall water splitting under sunlight irradiation using Z-scheme photocatalyst system, J. Am. Chem. Soc. 135 (2013) 5441–5449.
[41] H. Tada, T. Mitsui, T. Kiyonaga, T. Akita, K. Tanaka, All-solid-state Z-scheme in CdS-Au-TiO_2 three-component nanojunction system, Nat. Mater. 5 (2006) 782–786.
[42] K. Maeda, Z-scheme water splitting using two different semiconductor photocatalysts, ACS Catal. 3 (2013) 1486–1503.
[43] C. Kim, K.M. Cho, A. Al-Saggaf, I. Gereige, J. Hee-Tae, Z-scheme photocatalytic CO_2 conversion on three-dimensional $BiVO_4$/carbon-coated Cu_2O nanowire arrays under visible light, ACS Catal. 8 (2018) 4170–4177.
[44] W. Feng, J. Fang, G. Zhou, L. Zhang, S. Lu, S. Wu, Y. Chen, Y. Ling, Z. Fang, Rationally designed Bi@BiOCl/g-C_3N_4, heterostructure with exceptional solar-driven photocatalytic activity, Mol. Catal. 434 (2017) 69–79.
[45] L. Ye, J. Liu, C. Gong, L. Tian, T. Peng, L. Zan, Two different roles of metallic Ag on Ag/AgX/BiOX (X = Cl, Br) visible light photocatalysts: surface plasmon resonance and Z-scheme bridge, ACS Catal. 2 (2012) 1677–1683.
[46] H. Hagiwara, T. Inoue, S. Ida, T. Ishihara, Long-time charge separation in porphyrin/KTa(Zr)O_3 as water splitting photocatalyst, Phys. Chem. Chem. Phys. 13 (2011) 18031–18037.
[47] T. Ishihara, H. Hagiwara, S. Ida, Photocatalytic water splitting into H_2 and O_2 and charge separation mechanism on dye modified KTa(Zr)O_3, Am. Ins. Phys. 1 (2012) 515–518.
[48] W. Tu, Y. Zhou, S. Feng, Q. Xu, P. Li, X. Wang, M. Xiao, Z. Zou, Hollow spheres consisting of $Ti_{0.91}O_2$/CdS nanohybrids for CO_2 photofixation, Chem. Commun. 51 (2015) 13354–13357.
[49] X. Wang, G. Liu, Z.G. Chen, F. Li, L. Wang, G.Q. Lu, H.M. Cheng, Enhanced photocatalytic hydrogen evolution by prolonging the lifetime of carriers in ZnO/CdS heterostructures, Chem. Commun. 23 (2009) 3452–3454.
[50] J. Yu, S. Wang, J. Low, W. Xiao, Enhanced photocatalytic performance of direct Z-scheme g-C_3N_4-TiO_2 photocatalysts for the decomposition of formaldehyde in air, Phys. Chem. Chem. Phys. 15 (2013) 16883–16890.
[51] D. Huang, Z. Tang, Z. Peng, C. Lai, G. Zeng, C. Zhang, P. Xu, M. Cheng, J. Wan, R. Wang, Fabrication of water-compatible molecularly imprinted polymer based on β-cyclodextrin modified magnetic chitosan and its application for selective removal of bisphenol A from aqueous solution, J. Taiwan. Inst. Chem. E 77 (2017) 113–121.
[52] D. Huang, Y. Wang, C. Zhang, G. Zeng, C. Lai, J. Wan, L. Qin, Y. Zeng, Influence of morphological and chemical features of biochar on hydrogen peroxide activation: implications on sulfamethazine degradation, RSC Adv. 6 (2016) 73186–73196.
[53] C. Hu, D. Huang, G. Zeng, M. Cheng, X. Gong, R. Wang, W. Xue, Z. Hu, Y. Liu, The combination of Fenton process and Phanerochaete chrysosporium for the removal of bisphenol A in river sediments: mechanism related to extracellular enzyme, organic acid and iron, Chem. Eng. J. 338 (2018) 432–439.
[54] D. Huang, C. Hu, G. Zeng, M. Cheng, P. Xu, X. Gong, R. Wang, W. Xue, Combination of Fenton processes and biotreatment for wastewater treatment and soil remediation, Sci. Total Environ. 574 (2017) 1599–1610.
[55] D. Huang, R. Wang, Y. Liu, G. Zeng, C. Lai, P. Xu, B. Lu, J. Xu, C. Wang, C. Huang, Application of molecularly imprinted polymers in wastewater treatment: a review, Environ. Sci. Pollut. Res. 22 (2015) 963–977.
[56] D. Huang, X. Qin, P. Xu, G. Zeng, R. Wang, J. Wan, X. Gong, W. Xue, Composting of 4-nonylphenol-comtaminated river sediment with inocula of *Phanerochaete chrysosporium*, Bioresource Technol. 221 (2016) 47–54.
[57] M. Cheng, G. Zeng, D. Huang, C. Lai, P. Xu, C. Zhang, Y. Liu, Hydroxyl radicals based advanced oxidation processes (AOPs) for remediation of soils contaminated with organic compounds: a review, Chem. Eng. J. 284 (2016) 582–598.
[58] A. Primo, A. Corma, H. García, Titania supported gold nanoparticles as photocatalyst, Phys. Chem. Chem. Phys. 13 (2011) 886–910.
[59] O. Legrini, E. Oliveros, A.M. Braun, Photochemical processes for water treatment, Chem. Rev. 93 (1993) 671–698.
[60] Y. Bai, T. Chen, P. Wang, L. Wang, L. Ye, X. Shi, W. Bai, Size-dependent role of gold in g-C_3N_4/BiOBr/Au system for photocatalytic CO_2 reduction and dye degradation, Sol. Energ. Mater. Sol. C. 157 (2016) 406–414.

[61] L. Zhang, W. Feng, B. Wang, K. Wang, F. Gao, Y. Zhao, P. Liu, Construction of dual-channel for optimizing Z-scheme photocatalytic system, Appl. Catal. B: Environ. 212 (2017) 80–88.

[62] L. Liang, J. Cao, H. Lin, M. Zhang, X. Guo, S. Chen, A novel double visible light active Z-scheme AgI/Ag/I-$(BiO)_2CO_3$ composite: Automatic formation of Ag bridge in the photocatalytic process, Mater. Res. Bull. 94 (2017) 291–297.

[63] H. Li, Y. Sun, B. Cai, S. Gan, D. Han, L. Niu, T. Wu, Hierarchically Z-scheme photocatalyst of Ag@AgCl decorated on $BiVO_4$ (040) with enhancing photoelectrochemical and photocatalytic performance, Appl. Catal. B: Environ. 170–171 (2015) 206–214.

[64] Z. Song, Y. He, Novel AgCl/Ag/$AgFeO_2$ Z-scheme heterostructure photocatalyst with enhanced photocatalytic and stability under visible light, Appl. Surf. Sci. 420 (2017) 911–918.

[65] Q. Liu, C. Zeng, L. Ai, Z. Hao, J. Jiang, Boosting visible light photoreactivity of photoactive metal-organic framework: Designed plasmonic Z-scheme Ag/AgCl@MIL-53-Fe, Appl. Catal. B: Environ. 224 (2018) 38–45.

[66] Y. Yang, W. Guo, Y. Guo, Y. Zhao, X. Yuan, Y. Guo, Fabrication of Z-scheme plasmonic photocatalyst Ag@AgBr/g-C_3N_4 with enhanced visible-light photocatalytic activity, J. Hazard. Mater. 271 (2014) 150–159.

[67] Q. Li, F. Wang, Y. Hua, Y. Luo, X. Liu, G. Duan, X. Yang, Deposition-precipitation preparation of Ag/Ag_3PO_4/WO_3 nanocomposites for efficient Visible-light degradation of rhodamine B under strongly acidic/alkaline conditions, J. Colloid Interface Sci. 506 (2017) 207–216.

[68] X. Li, T. Wan, J. Qiu, H. Wei, F. Qin, Y. Wang, Y. Liao, Z. Huang, In-situ, photocalorimetry-fluorescence spectroscopy studies of RhB photocatalysis over Z-scheme g-C_3N_4@Ag@Ag_3PO_4, nanocomposites: a pseudo-zero-order rather than a first-order process, Appl. Catal. B: Environ. 217 (2017) 591–602.

[69] B. Chong, L. Chen, W. Wang, D. Han, L. Wang, L. Feng, Q. Li, C. Li, Visible-light-driven Ag-decorated g-C_3N_4/Bi_2WO_6 Z-scheme composite for high photocatalytic activity, Mater. Lett. 204 (2017) 149–153.

[70] L. Deng, Z. Zhu, L. Liu, H. Liu, Synthesis of Ag_2O and Ag co-modified flower-like SnS_2 composites with enhanced photocatalytic activity under solar light irradiation, Solid State Sci. 63 (2017) 76–83.

[71] D. Ma, J. Wu, M. Gao, Y. Xin, Y. Sun, T. Ma, Hydrothermal synthesis of an artificial Z-scheme visible light photocatalytic system using reduced graphene oxide as the electron mediator, Chem. Eng. J. 313 (2017) 1567–1576.

[72] W. Zhang, X. Xiao, X. Zeng, Y. Li, L. Zheng, C. Wan, Enhanced photocatalytic activity of TiO_2 nanoparticles using SnS_2/RGO hybrid as co-catalyst: DFT study and photocatalytic mechanism, J. Alloys Compd. 685 (2016) 774–783.

[73] T. Cai, Y. Liu, L. Wang, S. Zhang, Y. Zeng, J. Yuan, J. Ma, W. Dong, C. Liu, S. Luo, Silver phosphate-based Z-Scheme photocatalytic system with superior sunlight photocatalytic activities and anti-photocorrosion performance, Appl. Catal. B: Environ. 208 (2017) 1–13.

[74] X. Miao, X. Shen, J. Wu, Z. Ji, J. Wang, L. Kong, M. Liu, C. Song, Fabrication of an all solid Z-scheme photocatalyst g-C_3N_4/GO/AgBr with enhanced visible light photocatalytic activity, Appl. Catal. A 539 (2017) 104–113.

[75] F. Chen, Q. Yang, S. Wang, F. Yao, J. Sun, Y. Wang, C. Zhang, X. Li, C. Niu, D. Wang, G. Zeng, Graphene oxide and carbon nitride nanosheets co-modified silver chromate nanoparticles with enhanced visible-light photoactivity and anti-photocorrosion properties towards multiple refractory pollutants degradation, Appl. Catal. B: Environ. 209 (2017) 493–505.

[76] T. Zhou, G. Zhang, P. Ma, X. Qiu, H. Zhang, H. Yang, G. Liu, Novel magnetically separable Ag_3PO_4@$CuFe_2O_4$ micro-nanocomposite with highly enhanced visible-light-driven photocatalytic activity, Mater. Lett. 210 (2018) 271–274.

[77] M. Sun, Q. Zeng, X. Zhao, Y. Shao, P. Ji, C. Wang, T. Yan, B. Du, Fabrication of novel g-C_3N_4 nanocrystals decorated Ag_3PO_4 hybrids: Enhanced charge separation and excellent visible-light driven photocatalytic activity, J. Hazard. Mater. 339 (2017) 9–21.

[78] Y. Li, P. Wang, C. Huang, W. Yao, Q. Wu, Q. Xu, Synthesis and photocatalytic activity of ultrafine Ag_3PO_4 nanoparticles on oxygen vacated TiO_2, Appl. Catal. B: Environ. 205 (2017) 489–497.

[79] P. Tan, X. Chen, L. Wu, Y.Y. Shang, W. Liu, J. Pan, X. Xiong, Hierarchical flower-like $SnSe_2$, supported Ag_3PO_4, nanoparticles: towards visible light driven photocatalyst with enhanced performance, Appl. Catal. B: Environ. 202 (2017) 326–334.

[80] J. Wan, X. Du, E. Liu, Y. Hu, J. Fan, X. Hu, Z-scheme visible-light-driven Ag_3PO_4, nanoparticle@MoS_2, quantum dot/few-layered MoS_2, nanosheet heterostructures with high efficiency and stability for photocatalytic selective oxidation, J. Catal. 345 (2017) 281–294.

[81] H. Li, X. Xu, Hierarchical Fe_3O_4@MoS_2/Ag_3PO_4, magnetic nanocomposites: enhanced and stable photocatalytic performance for water purification under visible light irradiation, Appl. Surf. Sci. 389 (2016) 227–239.

[82] Q. Li, C. Yang, Facile fabrication of Ag_3PO_4 supported on ZnO inverse opals for enhancement of solar-driven photocatalysis, Mater. Lett. 199 (2017) 168–171.

[83] Z. Xiang, J. Zhong, S. Huang, J. Li, J. Chen, T. Wang, M. Li, P. Wang, Efficient charge separation of Ag_2CO_3/ZnO composites prepared by a facile precipitation approach and its dependence on loading content of Ag_2CO_3, Mater. Sci. Semicond. Process. 52 (2016) 62–67.

[84] M. Zhang, Y. Zhu, W. Li, F. Wang, H. Li, X. Liu, W. Zhang, C. Ren, Double Z-scheme system of silver bromide@bismuth tungstate/tungsten trioxide ternary heterojunction with enhanced visible-light photocatalytic activity, J Colloid Interface Sci. 509 (2017) 18–24.

[85] B. Feng, Z. Wu, J. Liu, K. Zhu, Z. Li, X. Jin, Y. Hou, Q. Xi, M. Cong, P. Liu, Q. Gu, Combination of ultrafast dye-sensitized-assisted electron transfer process and novel Z-scheme system: AgBr nanoparticles interspersed MoO3, nanobelts for enhancing photocatalytic performance of RhB, Appl. Catal. B: Environ. 206 (2017) 242–251.

[86] L. Yin, H. Zhang, X. Kong, J. Huang, D. Zhang, C. Liu, J. Fang, F. Zhang, Red AgCl/SmOCl Z-scheme composites: enhanced photocatalytic performance under sunlight, Mater. Lett. 210 (2018) 42–45.

[87] M. Cui, J. Yu, H. Lin, Y. Wu, L. Zhao, Y. He, In-situ preparation of Z-scheme AgI/Bi_5O_7I hybrid and its excellent photocatalytic activity, Appl. Surf. Sci. 387 (2016) 912–920.

[88] J. Zhang, Y. Hu, X. Jiang, S. Chen, S. Meng, X. Fu, Design of a direct Z-scheme photocatalyst: preparation and characterization of Bi_2O_3/g-C_3N_4 with high visible light activity, J. Hazard. Mater. 280 (2014) 713–722.

[89] S. Chen, Y. Hu, L. Ji, X. Jiang, X. Fu, Preparation and characterization of direct Z-scheme photocatalyst Bi_2O_3/$NaNbO_3$ and its reaction mechanism, Appl. Surf. Sci. 292 (2014) 357–366.

[90] X. Ye, S. Zhao, S. Meng, X. Fu, L. Bai, Y. Guo, X. Wang, S. Chen, Remarkable enhancement of photocatalytic performance via constructing a novel Z-scheme $KNbO_3$/Bi_2O_3, hybrid material, Mater. Res. Bull. 94 (2017) 352–360.

[91] M. Sun, Y. Wang, Y. Shao, Y. He, Q. Zeng, H. Liang, T. Yan, B. Du, Fabrication of a novel Z-scheme g-C_3N_4/Bi_4O_7 heterojunction photocatalyst with enhanced visible light-driven activity toward organic pollutants, J. Colloid Interface Sci. 501 (2017) 123–132.

[92] M. Yang, Q. Yang, J. Zhong, S. Huang, J. Li, J. Song, C. Burda, Enhanced photocatalytic performance of Ag_2O/BiOF composite photocatalysts originating from efficient interfacial charge separation, Appl. Surf. Sci. 416 (2017) 666–671.

[93] C. Liu, Q. Wu, M. Ji, H. Zhu, H. Hou, Q. Yang, C. Jiang, J.J. Wang, L. Tian, J. Chen, W. Hou, Constructing Z-scheme charge separation in 2D layered porous BiOBr/graphitic C_3N_4, nanosheets nanojunction with enhanced photocatalytic activity, J. Alloys Compd. 723 (2017) 1121–1131.

[94] F. Qiu, W. Li, F. Wang, H. Li, X. Liu, J. Sun, In-situ synthesis of novel Z-scheme SnS_2/BiOBr photocatalysts with superior photocatalytic efficiency under visible light, J. Colloid Interface Sci. 493 (2017) 1–9.

[95] S. Wang, X. Yang, X. Zhang, X. Ding, Z. Yang, K. Dai, H. Chen, A plate-on-plate sandwiched Z-scheme heterojunction photocatalyst: BiOBr-Bi_2MoO_6 with enhanced photocatalytic performance, Appl. Surf. Sci. 391 (2017) 194–201.

[96] H. Li, T. Hu, R. Zhang, J. Liu, W. Hou, Preparation of solid-state Z-scheme Bi_2MoO_6/MO (M, Cu, $Co_{3/4}$, or Ni) heterojunctions with internal electric field-improved performance in photocatalysis, Appl. Catal. B: Environ. 188 (2016) 313–323.

[97] J. Zhang, Y. Ma, Y. Du, H. Jiang, D. Zhou, S. Dong, Carbon nanodots/WO_3 nanorods Z-scheme composites: remarkably enhanced photocatalytic performance under broad spectrum, Appl. Catal. B: Environ. 209 (2017) 253–264.

[98] X. Ma, W. Ma, D. Jiang, D. Li, S. Meng, Construction of novel WO_3/$SnNb_2O_6$ hybrid nanosheet heterojunctions as efficient Z-scheme photocatalysts for pollutant degradation, J. Colloid Interface Sci. 506 (2017) 93–101.

[99] C. Song, X. Wang, J. Zhang, X. Chen, C. Li, Enhanced performance of direct Z-scheme CuS-WO_3, system towards photocatalytic decomposition of organic pollutants under visible light, Appl. Surf. Sci. 425 (2017) 788–795.

[100] L. Cui, X. Ding, Y. Wang, H. Shi, L. Huang, Y. Zuo, S. Kang, Facile preparation of Z-scheme WO_3/g-C_3N_4 composite photocatalyst with enhanced photocatalytic performance under visible light, Appl. Surf. Sci. 391 (2017) 202–210.

[101] J. Wang, C. Li, J. Cong, Z. Liu, H. Zhang, M. Liang, J. Gao, S. Wang, J. Yao, Facile synthesis of nanorod-type graphitic carbon nitride/Fe_2O_3, composite with enhanced photocatalytic performance, J. Solid State Chem. 238 (2016) 246–251.

[102] Y. Li, K. Lv, W. Ho, F. Dong, X. Wu, Y. Xia, Hybridization of rutile TiO_2 ($rTiO_2$) with g-C_3N_4 quantum dots (CN QDs): an efficient visible-light-driven Z-scheme hybridized photocatalyst, Appl. Catal. B: Environ. 202 (2017) 611–619.

[103] W. Wang, H. Cheng, B. Huang, X. Liu, X. Qin, X. Zhang, Y. Dai, Hydrothermal synthesis of C_3N_4/$BiOIO_3$ heterostructures with enhanced photocatalytic properties, J. Colloid Interface Sci. 442 (2015) 97–102.

[104] F. Wang, Y.T. Zhang, Y. Xu, X. Wang, S. Li, H. Yang, X. Liu, F. Wei, Enhanced photodegradation of Rhodamine B by coupling direct solid-state Z-scheme N-$K_2Ti_4O_9$/g-C_3N_4, heterojunction with high adsorption capacity of UiO-66, J. Environ. Chem. Eng. 4 (2016) 3364–3373.

[105] Y. He, L. Zhang, M. Fan, X. Wang, M.-L. Walbridge, Q. Nong, Y. Wu, L. Zhao, Z-scheme SnO_2-x/g-C_3N_4 composite as an efficient photocatalyst for dye degradation and photocatalytic CO_2 reduction, Sol. Energy Mater. Sol. Cells 137 (2015) 175–184.

[106] Y. Shang, X. Chen, W. Liu, P. Tan, H. Chen, L. Wu, C. Ma, X. Xiong, J. Pan, Photocorrosion inhibition and high-efficiency photoactivity of porous g-C_3N_4/Ag_2CrO_4 composites by simple microemulsion-assisted co-precipitation method, Appl. Catal. B: Environ. 204 (2017) 78–88.

[107] X. Chen, P. Tan, B. Zhou, H. Dong, J. Pan, X. Xiong, A green and facile strategy for preparation of novel and stable Cr-doped $SrTiO_3$/g-C_3N_4, hybrid nanocomposites with enhanced visible light photocatalytic activity, J. Alloys Compd. 647 (2015) 456–462.

[108] W. Chen, T.Y. Liu, T. Huang, X.H. Liu, J.W. Zhu, G.R. Duan, X.J. Yang, In situ fabrication of novel Z-scheme Bi_2WO_6, quantum dots/g-C_3N_4, ultrathin nanosheets heterostructures with improved photocatalytic activity, Appl. Surf. Sci. 355 (2015) 379–387.

[109] H.C. Zhou, J.R. Long, O.M. Yaghi, Introduction to metal-organic frameworks, Chem. Rev. 112 (2017) 673–674.

[110] H. Zhu, B. Yang, J. Xu, Z. Fu, M. Wen, T. Guo, S. Fu, J. Zuo, S.Y. Zhang, Construction of Z-scheme type CdS-Au-TiO_2 hollow nanorod arrays with enhanced photocatalytic activity, Appl. Catal. B: Environ. 90 (2009) 463–469.

[111] F. Wu, X. Li, W. Liu, S. Zhang, Highly enhanced photocatalytic degradation of methylene blue over the indirect all-solid-state Z-scheme g-C_3N_4-RGO-TiO_2 nanoheterojunctions, Appl. Surf. Sci. 405 (2017) 60–70.

[112] L. Chen, F. He, N. Zhao, R. Guo, Fabrication of 3D quasi-hierarchical Z-scheme RGO-Fe_2O_3-MoS_2 nano-heterostructures for highly enhanced visible-light-driven photocatalytic degradation, Appl. Surf. Sci. 420 (2017) 669–680.

[113] F. Li, B. Dong, Construction of novel Z-scheme Cu_2O/graphene/α-Fe_2O_3 nanotube arrays composite for enhanced photocatalytic activity, Ceram. Int. 43 (2017) 16007–16012.

[114] X. Yao, X. Liu, One-pot synthesis of ternary Ag_2CO_3/Ag/AgCl photocatalyst in natural geothermal water with enhanced photocatalytic activity under visible light irradiation, J. Hazard. Mater. 280 (2014) 260–268.

[115] Y. Wan, C. Liang, Y. Xia, W. Huang, Z. Li, Fabrication of graphene oxide enwrapped Z-scheme Ag_2SO_3/AgBr nanoparticles with enhanced visible-light photocatalysis, Appl. Surf. Sci. 396 (2016) 48–57.

[116] H. Tang, Y. Fu, S. Chang, S. Xie, G. Tang, Construction of Ag_3PO_4/Ag_2MoO_4 Z-scheme heterogeneous photocatalyst for the remediation of organic pollutants, Chin. J. Catal. 38 (2016) 337–347.

[117] C. Zhang, K. Yu, Y. Feng, Y. Chang, T. Yang, Y. Xuan, D. Lei, L.L. Lou, S. Liu, Novel 3DOM-$SrTiO_3$/Ag/Ag_3PO_4, ternary Z-scheme photocatalysts with remarkably improved activity and durability for contaminant degradation, Appl. Catal. B: Environ. 210 (2017) 77–87.

[118] X. Liu, J. Jiang, Y. Jia, J. Qiu, T. Xia, Y. Zhang, Y. Li, X. Chen, Insight into synergistically enhanced adsorption and visible light photocatalytic performance of Z-Scheme heterojunction of $SrTiO_3$(La, Cr)-decorated WO_3 nanosheets, Appl. Surf. Sci. 412 (2017) 279–289.

[119] S. Chen, Y. Hu, X. Jiang, S. Meng, X. Fu, Fabrication and characterization of novel Z-scheme photocatalyst WO_3/g-C_3N_4, with highly efficient visible light photocatalytic activity, Mater. Chem. Phys. 149–150 (2015) 512–521.

[120] X. Liu, A. Jin, Y. Jia, T. Xia, C. Deng, M. Zhu, C. Chen, X. Chen, Synergy of adsorption and visible-light photocatalytic degradation of methylene blue by a bifunctional Z-scheme heterojunction of WO_3/g-C_3N_4, Appl. Surf. Sci. 405 (2017) 359–371.

[121] C. Zhu, L. Zhang, B. Jiang, J. Zheng, P. Hu, Fabrication of Z-scheme Ag_3PO_4/MoS_2 composites with enhanced photocatalytic activity and stability for organic pollutant degradation, Appl. Surf. Sci. 377 (2016) 99–108.

[122] L. Zhen, D. Kai, J. Zhang, C. Liang, G. Zhu, Facile synthesis of novel octahedral Cu2O/Ag3PO4 composite with enhanced visible light photocatalysis, Mater. Lett. 206 (2017) 48–51.

[123] L.V. Bora, R.K. Mewada, Photocatalytic treatment of dye wastewater and parametric study using a novel Z-scheme Ag2CO3/SiC photocatalyst under natural sunlight, J. Environ Chem. Eng. 5 (2017) 5556–5565.

[124] D. Xu, B. Cheng, S. Cao, J. Yu, Enhanced photocatalytic activity and stability of Z-scheme Ag_2CrO_4-GO composite photocatalysts for organic pollutant degradation, Appl. Catal. B: Environ. 164 (2015) 380–388.

[125] J. Zhang, J. Lv, K. Dai, Q. Liu, C. Liang, G. Zhu, Facile and green synthesis of novel porous g-C3N4/Ag3PO4, composite with enhanced visible light photocatalysis, Ceram. Int. 43 (2017) 1522–1529.

[126] J. Lv, K. Dai, J. Zhang, Q. Liu, C. Liang, G. Zhu, Facile constructing novel 2D porous g-C_3N_4/BiOBr hybrid with enhanced visible-light-driven photocatalytic activity, Sep. Purif. Technol. 178 (2017) 6–17.

[127] Z. Wang, J. Lv, J. Zhang, K. Dai, C. Liang, Facile synthesis of Z-scheme $BiVO_4$/porous graphite carbon nitride heterojunction for enhanced visible-light-driven photocatalyst, Appl. Surf. Sci. 430 (2017) 595–602.

[128] S. Singh, R. Sharma, B.R. Mehta, Enhanced surface area, high Zn interstitial defects and band gap reduction in N-doped ZnO nanosheets coupled with $BiVO_4$ leads to improved photocatalytic performance, Appl. Surf. Sci. 411 (2017) 321–330.

[129] J. Lv, K. Dai, J. Zhang, L. Geng, C. Liang, Q. Liu, G. Zhu, C. Chen, Facile synthesis of Z-scheme graphitic-C_3N_4/Bi_2MoO_6 nanocomposite for enhanced visible photocatalytic properties, Appl. Surf. Sci. 358 (2015) 377–384.

[130] Z. Wang, J. Lv, K. Dai, L. Lu, C. Liang, L. Geng, Large scale and facile synthesis of novel Z-scheme Bi_2MoO_6/Ag_3PO_4 composite for enhanced visible light photocatalyst, Mater. Lett. 169 (2016) 250–253.

[131] X. Zhao, J. Yu, H. Cui, T. Wang, Preparation of direct Z-scheme $Bi_2Sn_2O_7$/g-C_3N_4 composite with enhanced photocatalytic performance, J. Photochem. Photobiol. A Chem. 335 (2017) 130–139.

[132] Y. Liu, Y. Shi, X. Liu, H. Li, A facile solvothermal approach of novel Bi_2S_3/TiO_2/RGO composites with excellent visible light degradation activity for methylene blue, Appl. Surf. Sci. 396 (2017) 58–66.

[133] X. Yan, Z. Wu, C. Huang, K. Liu, W. Shi, Hydrothermal synthesis of CdS/$CoWO_4$ heterojunctions with enhanced visible light properties toward organic pollutants degradation, Ceram. Int. 43 (2017) 5388–5395.

[134] R. Ma, M.J. Islam, D.A. Reddy, T.K. Kim, Transformation of CeO_2, into a mixed phase CeO_2/Ce2O_3, nanohybrid by liquid phase pulsed laser ablation for enhanced photocatalytic activity through Z-scheme pattern, Ceram. Int. 42 (2016) 18495–18502.

[135] Z. Dong, Y. Wu, Magnetically separable photocatalyst of direct Z-scheme g-C_3N_4 nanosheets/natural hematite ore hybrids, J. Photochem. Photobiol. A. Chem. 156 (2017) 156–163.

[136] Y. Jiang, P. Liu, S. Tian, Y. Liu, Z. Peng, Sustainable visible-light-driven Z-scheme porous $Zn_3(VO_4)_2$/g-C_3N_4, heterostructure toward highly photo-redox pollutant and mechanism insight, J. Taiwan. Inst. Chem. Eng. 78 (2017) 517–529.

[137] J. Zhang, F. Xiao, Modulation of interfacial charge transfer by self-assembly of single-layer graphene enwrapped one-dimensional semiconductors toward photoredox catalysis, J. Mater. Chem. A 5 (2017) 23681–23693.

[138] X. Wang, Y. Nishihara, Photocatalytic activities of graphitic carbon nitride powder for water reduction and oxidation under visible light, J. Phys. Chem. C 113 (2009) 4940–4947.

[139] J. Li, J. Zhou, H. Hao, W. Li, Controlled synthesis of Fe_2O_3, modified Ag-010$BiVO_4$, heterostructures with enhanced photoelectrochemical activity toward the dye degradation, Appl. Surf. Sci. 399 (2017) 1–9.

[140] J. Li, H. Yuan, Z. Zhu, Fabrication of Cu_2O/Au/$BiPO_4$ Z-scheme photocatalyst to improve the photocatalytic activity under solar light, J. Mol. Catal. A: Chem. 410 (2015) 133–139.

[141] L. Wang, C.G. Niu, Y. Wang, Y. Wang, G.M. Zeng, The synthesis of Ag/AgCl/$BiFeO_3$ photocatalyst with enhanced visible photocatalytic activity, Ceram. Int. 42 (2016) 18605–18611.

[142] X. Li, D. Wu, Q. Luo, R. Yin, J. An, S. Liu, D. Wang, Fabrication of CPAN/Ag/AgCl composites and their efficient visible light photocatalytic activity, J. Alloys Compd. 702 (2017) 585–593.

[143] T. Zhou, Y. Xu, H. Xu, H. Wang, Z. Da, S. Huang, H. Ji, H. Li, In situ, oxidation synthesis of visible-light-driven plasmonic photocatalyst Ag/AgCl/g-C_3N_4 and its activity, Ceram. Int. 40 (2014) 9293–9301.

[144] T. Yan, J. Tian, W. Guan, Z. Qiao, W. Li, J. You, B. Huang, Ultra-low loading of Ag_3PO_4 on hierarchical In_2S_3 microspheres to improve the photocatalytic performance: The co-catalytic effect of Ag and Ag_3PO_4, Appl. Catal. B: Environ. 202 (2017) 84–94.

[145] Y. Fu, W. Liang, J. Guo, H. Tang, S. Liu, MoS_2 quantum dots decorated g-C_3N_4/Ag heterostructures for enhanced visible light photocatalytic activity, Appl. Surf. Sci. 430 (2017) 434–442.

[146] H. Wang, D. Peng, T. Chen, Y. Chang, S. Dong, A novel photocatalyst AgBr/ZnO/RGO with high visible light photocatalytic activity, Ceram. Int. 42 (2016) 4406–4412.

[147] J. He, D. Shao, L. Zheng, L. Zheng, D. Feng, J. Xu, X. Zhang, W. Wang, W. Wang, F. Lu, H. Dong, Y. Cheng, H. Liu, R. Zheng, Construction of Z-scheme Cu_2O/Cu/AgBr/Ag photocatalyst with enhanced photocatalytic activity and stability under visible light, Appl. Catal. B: Environ. 203 (2017) 917–926.

[148] Y. Xu, Q. Liu, C. Liu, Y. Zhai, M. Xie, L. Huang, H. Xu, H. Li, J. Jing, Visible-light-driven Ag/AgBr/$ZnFe_2O_4$ composites with excellent photocatalytic activity for *E. coli* disinfection and organic pollutant degradation, J. Colloid Interface Sci. 512 (2017) 555–566.

[149] H. Lin, J. Cao, B. Luo, B. Xu, S. Chen, Synthesis of novel Z-scheme AgI/Ag/AgBr composite with enhanced visible light photocatalytic activity, Catal. Commun. 21 (2012) 91–95.

[150] J. Cao, Y. Zhao, H. Lin, B. Xu, S. Chen, Facile synthesis of novel Ag/AgI/BiOI composites with highly enhanced visible light photocatalytic performances, J. Solid State Chem. 206 (2013) 38–44.

[151] N. Shao, J. Wang, D. Wang, P. Corvini, Preparation of three-dimensional Ag_3PO_4/TiO_2@MoS_2 for enhanced visible-light photocatalytic activity and anti-photocorrosion, Appl. Catal. B: Environ. 203 (2017) 964–978.

[152] J. Luo, X. Zhou, L. Ma, L. Xu, X. Xu, Z. Du, J. Zhang, Enhancing visible light photocatalytic activity of direct Z-scheme SnS2/Ag3PO4 heterojunction photocatalysts, Mater. Res. Bull. 81 (2016) 16–26.

[153] J. Luo, X. Zhou, L. Ma, X. Ning, L. Zhan, X. Xu, L. Xu, L. Zhang, H. Ruan, Z. Zhang, Fabrication of WO_3/Ag_2CrO_4 composites with enhanced visible-light photodegradation towards methyl orange, Adv. Polym. Tech. 28 (2017) 1018–1027.

[154] J. Luo, X. Zhou, L. Ma, X. Xu, Rational construction of Z-scheme Ag_2CrO_4/g-C_3N_4 composites with enhanced visible-light photocatalytic activity, Appl. Surf. Sci. 390 (2016) 357–367.

[155] B. Zhu, P. Xia, Y. Li, W. Ho, J. Yu, Fabrication and photocatalytic activity enhanced mechanism of direct Z-scheme g-C_3N_4/Ag_2WO_4 photocatalyst, Appl. Surf. Sci. 391 (2017) 175–183.

[156] J. Li, J. Zhong, Y. Si, S. Huang, L. Dou, M. Li, Y. Liu, J. Ding, Improved solar-driven photocatalytic performance of BiOI decorated TiO_2 benefiting from the separation properties of photo-induced charge carriers, Solid State Sci. 52 (2016) 106–111.

[157] J. Li, H. Yuan, Z. Zhu, Improved photoelectrochemical performance of Z-scheme g-C_3N_4/Bi_2O_3/$BiPO_4$ heterostructure and degradation property, Appl. Surf. Sci. 385 (2016) 34–41.

[158] S. Huang, J. Zhong, J. Li, J. Chen, Z. Xiang, Z-scheme TiO_2/g-C_3N_4 composites with improved solar-driven photocatalytic performance deriving from remarkably efficient separation of photo-generated charge pairs, Mater. Res. Bull. 84 (2016) 65–70.

[159] B. Chen, P. Li, S. Zhang, W. Zhang, X. Dong, F. Xi, J. Liu, The enhanced photocatalytic performance of Z-scheme two-dimensional/two-dimensional heterojunctions from graphitic carbon nitride nanosheets and titania nanosheets, J. Colloid Interface Sci. 478 (2016) 263–270.

[160] Y. Liu, R. Wang, Z. Yang, H. Du, Y. Jiang, C. Shen, K. Liang, A. Xu, Enhanced visible-light photocatalytic activity of Z-scheme graphitic carbon nitride/oxygen vacancy-rich zinc oxide hybrid photocatalysts, Chin. J. Catal. 36 (2015) 2135–2144.

[161] D. Ma, J. Wu, M. Gao, Y. Xin, T. Ma, Y. Sun, Fabrication of Z-scheme g-C_3N_4/RGO/Bi_2WO_6 photocatalyst with enhanced visible-light photocatalytic activity, Chem. Eng. J. 290 (2016) 136–146.

[162] X. Chen, Y. Dai, J. Guo, F. Bu, X. Wang, Synthesis of micro-nano Ag_3PO_4/$ZnFe_2O_4$ with different organic additives and its enhanced photocatalytic

activity under visible light irradiation, Mater. Sci. Semicond. Process. 41 (2016) 335–342.
[163] H. Li, X. Quan, S. Chen, H. Yu, Ferroelectric-enhanced Z-schematic electron transfer in $BiVO_4$-$BiFeO_3$-$CuInS_2$, for efficient photocatalytic pollutant degradation, Appl. Catal. B: Environ. 209 (2017) 591–599.
[164] A.B. Lavand, Y.S. Malghe, Visible light photocatalytic degradation of 4-chlorophenol using C/ZnO/CdS nanocomposite, J. Saudi. Chem. Soc. 19 (2015) 471–478.
[165] J. Wang, Y. Xia, H. Zhao, G. Wang, L. Xiang, J. Xu, S. Komarneni, Oxygen defects-mediated Z-scheme charge separation in g-C_3N_4/ZnO photocatalysts for enhanced visible-light degradation of 4-chlorophenol and hydrogen evolution, Appl. Catal. B: Environ. 206 (2017) 406–416.
[166] S. Zuo, Y. Chen, W. Liu, C. Yao, X. Li, Z. Li, C. Ni, X. Liu, A facile and novel construction of attapulgite/Cu_2O/Cu/g-C_3N_4 with enhanced photocatalytic activity for antibiotic degradation, Ceram. Int. 43 (2016) 3324–3329.
[167] F. Chen, Q. Yang, X. Li, G. Zeng, D. Wang, C. Niu, J. Zhao, H. An, T. Xie, Y. Deng, Hierarchical assembly of graphene-bridged Ag_3PO_4/Ag/$BiVO_4$ (040) Z-scheme photocatalyst: an efficient, sustainable and heterogeneous catalyst with enhanced visible-light photoactivity towards tetracycline degradation under visible light irradiation, Appl. Catal. B: Environ. 200 (2017) 330–342.
[168] W. Shi, F. Guo, S. Yuan, In situ synthesis of Z-scheme Ag_3PO_4/$CuBi_2O_4$, photocatalysts and enhanced photocatalytic performance for the degradation of tetracycline under visible light irradiation, Appl. Catal. B: Environ. 209 (2017) 720–728.
[169] F. Chen, Q. Yang, Y. Wang, J. Zhao, D. Wang, X. Li, Z. Guo, H. Wang, Y. Deng, C. Niu, G. Zeng, Novel ternary heterojunction photocatalyst of Ag nanoparticles and g-C_3N_4, nanosheets co-modified $BiVO_4$ for wider spectrum visible-light photocatalytic degradation of refractory pollutant, Appl. Catal. B: Environ. 205 (2017) 133–147.
[170] T. Wang, W. Quan, D. Jiang, L. Chen, D. Li, S. Meng, M. Chen, Synthesis of redox-mediator-free direct Z-scheme AgI/WO_3, nanocomposite photocatalysts for the degradation of tetracycline with enhanced photocatalytic activity, Chem. Eng. 300 (2016) 280–290.
[171] F. Chen, Q. Yang, F. Yao, S. Wang, J. Sun, H. An, K. Yi, Y. Wang, Y. Zhou, L. Wang, X. Li, D. Wang, G. Zeng, Visible-light photocatalytic degradation of multiple antibiotics by AgI nanoparticle-sensitized Bi_5O_7I microspheres: enhanced interfacial charge transfer based on Z-scheme heterojunctions, J. Catal. 352 (2017), 160–170.matsu.
[172] S. Song, A. Meng, S. Jiang, B. Cheng, C. Jiang, Construction of Z-scheme Ag_2CO_3/N-doped graphene photocatalysts with enhanced visible-light photocatalytic activity by tuning the nitrogen species, Appl. Surf. Sci. 396 (2017) 1368–1374.
[173] M. Mao, F. Chen, C. Zheng, J. Ning, Y. Zhong, Y. Hu, Facile synthesis of porous Bi_2O_3-$BiVO_4$, p-n heterojunction composite microrods with highly efficient photocatalytic degradation of phenol, J. Alloys Compd. 688 (2016) 1080–1087.
[174] D. Huang, X. Wang, C. Zhang, G. Zeng, Z. Peng, J. Zhou, M. Cheng, R. Wang, Z. Hu, X. Qin, Sorptive removal of ionizable antibiotic sulfamethazine from aqueous solution by graphene oxide-coated biochar nanocomposites: Influencing factors and mechanism, Chemosphere 186 (2017) 414–421.
[175] D. Huang, X. Guo, Z. Peng, G. Zeng, P. Xu, X. Gong, R. Deng, W. Xue, R. Wang, H. Yi, C. Liu, White rot fungi and advanced combined biotechnology with nanomaterials: promising tools for endocrine-disrupting compounds biotransformation, Crit. Rev. Biotechnol. 38 (2017) 671–689.
[176] W. Wang, G. Li, D. Xia, T. An, H. Zhao, P. Wong, Photocatalytic nanomaterials for solar-driven bacterial inactivation: recent progress and challenges, Environ. Sci. Nano. 4 (2017) 782–799.
[177] H. Hidaka, S. Horikoshi, K. Ajisaka, J. Zhao, N. Serpone, Fate of amino acids upon exposure to aqueous titania irradiated with UV-A and UV-B radiation Photocatalyzed formation of NH_3, NO^{3-}, and CO_2, J. Photochem. Photobiol. A: Chem. 108 (1997) 197–205.
[178] X. Yang, Y. Wang, Photocatalytic effect on plasmid DNA damage under different UV irradiation time, Bull. Environ. 43 (2008) 253–257.
[179] Y. Su, R. Kinjo, Boron-containing radical species, Coord. Chem. Rev. 352 (2017) 346–378.
[180] B. Halliwell, S. Chirico, Lipid peroxidation: its mechanism, measurement, and significance, Am. J. Clin. Nutr. 57 (1993) 715S.
[181] D. Xia, W. Wang, R. Yin, Z. Jiang, T. An, G. Li, H. Zhao, P.-K. Wong, Enhanced photocatalytic inactivation of Escherichia coli by a novel Z-scheme g-C_3N_4/*m*-Bi_2O_4, hybrid photocatalyst under visible light: the role of reactive oxygen species, Appl. Catal. B: Environ. 214 (2017) 23–33.
[182] E.M. Anastasi, T.D. Wohlsen, H.M. Stratton, M. Katouli, Survival of *Escherichia coli* in two sewage treatment plants using UV irradiation and chlorination for disinfection, Water Res. 47 (2013) 6670–6679.
[183] O.K. Dalrymple, E. Stefanakos, M.A. Trotz, D.Y. Goswami, A review of the mechanisms and modeling of photocatalytic disinfection, Appl. Catal. B: Environ. 98 (2010) 27–38.
[184] D. Huang, R. Deng, J. Wan, G. Zeng, W. Xue, X. Wen, C. Zhou, L. Hu, X. Liu, X. Guo, X. Ren, Remediation of lead-contaminated sediment by biochar-supported nano-chlorapatite: accompanied with the change of available phosphorus and organic matters, J. Hazard. Mater. 348 (2018) 109–116.
[185] T. Matsunaga, R. Tomoda, T. Nakajima, H. Wake, Photoelectrochemical sterilization of microbial cells by semiconductor powders, FEMS Microbiol. Lett. 29 (1985) 211–214.
[186] Z. Xiong, M. Zheng, C. Zhu, B. Zhang, L. Ma, W. Shen, One-step synthesis of highly efficient three-dimensional $Cd_{1-x}Zn_xS$ photocatalysts for visible light photocatalytic water splitting, Nanoscale Res. Lett. 8 (2013) 1–6.
[187] X. Wang, T.T. Lim, Highly efficient and stable Ag-AgBr/TiO_2 composites for destruction of Escherichia coli under visible light irradiation, Water Res. 47 (2013) 4148–4158.
[188] M. Xing, J. Zhang, F. Chen, New approaches to prepare nitrogen-doped TiO_2 photocatalysts and study on their photocatalytic activities in visible light, Appl. Catal. B: Environ. 89 (2009) 563–569.
[189] T. Baran, S. Wojtyła, A. Dibenedetto, M. Aresta, W. Macyk, Zinc sulfide functionalized with ruthenium nanoparticles for photocatalytic reduction of CO_2, Appl. Catal. B: Environ. 178 (2015) 170–176.
[190] F. Su, S.C. Mathew, G. Lipner, X. Fu, M. Antonietti, S. Blechert, X. Wang, mpg-C_3N_4-catalyzed selective oxidation of alcohols using O_2 and visible light, J. Amer. Chem. Soc. 132 (2010) 16299–16301.
[191] W. Wang, T. An, G. Li, D. Xia, H. Zhao, J.C. Yu, P.K. Wong, Earth-abundant Ni_2P/g-C_3N_4 lamellar nanohydrids for enhanced photocatalytic hydrogen evolution and bacterial inactivation under visible light irradiation, Appl. Catal. B: Environ. 217 (2017) 570–580.
[192] G. Mamba, A.K. Mishra, Graphitic carbon nitride (g-C_3N_4) nanocomposites: a new and exciting generation of visible light driven photocatalysts for environmental pollution remediation, Appl. Catal. B: Environ. 198 (2016) 347–377.
[193] X. Zeng, Z. Wang, G. Wang, T.R. Gengenbach, D.T. Mccarthy, A. Deletic, J. Yu, X. Zhang, Highly dispersed TiO_2, nanocrystals and WO_3, nanorods on reduced graphene oxide: z-scheme photocatalysis system for accelerated photocatalytic water disinfection, Appl. Catal. B: Environ. 218 (2017) 163–173.
[194] D. Guan, C. Niu, X. Wen, H. Guo, C. Deng, G. Zeng, Enhanced *Escherichia coli* inactivation and oxytetracycline hydrochloride degradation by a Z-scheme silver iodide decorated bismuth vanadate nanocomposite under visible light irradiation, J Colloid Interface Sci. 512 (2017) 272–281.
[195] J. Liang, F. Liu, J. Deng, M. Li, M. Tong, Efficient bacterial inactivation with Z-scheme AgI/Bi_2MoO_6 under visible light irradiation, Water Res. 123 (2017) 632–641.
[196] D. Huang, W. Xue, G. Zeng, J. Wan, G. Chen, C. Huang, C. Zhang, M. Chen, P. Xu, Immobilization of Cd in river sediments by sodium alginate modified nanoscale zero-valent iron: impact on enzyme activities and microbial community diversity, Water Res. 106 (2016) 15–25.
[197] R. Wang, D. Huang, Y. Liu, C. Zhang, C. Lai, G. Zeng, M. Cheng, X. Gong, J. Wan, H. Luo, Investigating the adsorption behavior and the relative distribution of Cd^{2+} sorption mechanisms on biochars by different feedstock, Bioresour. Technol. 261 (2018) 265–271.
[198] D. Huang, X. Gong, Y. Liu, G. Zeng, C. Lai, H. Bashir, L. Zhou, D. Wang, P. Xu, M. Cheng, J. Wan, Effects of calcium at toxic concentrations of cadmium in plants, Planta 245 (2017) 1–11.
[199] D. Huang, Z. Hu, Z. Peng, G. Zeng, G. Chen, C. Zhang, M. Cheng, J. Wan, X. Wang, X. Qin, Cadmium immobilization in river sediment using stabilized nanoscale zero-valent iron with enhanced transport by polysaccharide coating, J. Environ. Manag. 210 (2018) 191–200.
[200] X. Guo, Z. Peng, D. Huang, P. Xu, G. Zeng, S. Zhou, X. Gong, M. Cheng, R. Deng, H. Yi, H. Luo, X. Yan, T. Li, Biotransformation of cadmium-sulfamethazine combined pollutant in aqueous environments: phanerochaete chrysosporium bring cautious optimism, Chem. Eng. J. 347 (2018) 74–83.
[201] W. Xue, D. Huang, G. Zeng, J. Wan, C. Zhang, R. Xu, M. Cheng, R. Deng, Nanoscale zero-valent iron coated with rhamnolipid as an effective stabilizer for immobilization of Cd and Pb in river sediments, J. Hazard. Mater. 341 (2018) 381–389.
[202] D. Huang, X. Qin, Z. Peng, Y. Liu, X. Gong, G. Zeng, C. Huang, M. Cheng, W. Xue, X. Wang, Z. Hu, Nanoscale zero-valent iron assisted phytoremediation of Pb in sediment: Impacts on metal accumulation and antioxidative system of *Lolium perenne*, Ecotox. Environ. Safe 153 (2018) 229–237.
[203] Y. Yang, Z. Zeng, C. Zhang, D. Huang, G. Zeng, R. Xiao, C. Lai, C. Zhou, H. Guo, W. Xue, M. Cheng, W. Wang, J. Wang, Construction of iodine vacancy-rich BiOI/Ag@AgI Z-scheme heterojunction photocatalysts for visible-light-driven tetracycline degradation: transformation pathways and mechanism insight, Chem. Eng. J. 349 (2018) 808–821.
[204] D. Huang, L. Liu, G. Zeng, P. Xu, C. Huang, L. Deng, R. Wang, J. Wan, The effects of rice straw biochar on indigenous microbial community and enzymes activity in heavy metal-contaminated sediment, Chemosphere 174 (2017) 545–553.
[205] X. Gong, D. Huang, Y. Liu, G. Zeng, R. Wang, W. Xue, C. Huang, P. Xu, J. Wan, C. Zhang, Pyrolysis and reutilization of plant residues after phytoremediation of heavy metals contaminated sediments: for heavy metals stabilization and dye adsorption, Bioresour. Technol. 253 (2018) 64–71.
[206] M. Owlad, M.K. Aroua, W.D.W. Ashri, S. Baroutian, Removal of hexavalent chromium-contaminated water and wastewater: a review, Water Air Soil Poll. 200 (2009) 59–77.
[207] L.B. Khalil, W.E. Mourad, M.W. Rophael, Photocatalytic reduction of environmental pollutant Cr(VI) over some semiconductors under UV/visible light illumination, Appl. Catal. B: Environ. 17 (1998) 267–273.
[208] X. Yang, Y. Xiang, Y. Qu, X. Ding, H. Chen, Novel in situ fabrication of conjugated microporous poly(benzothiadiazole)-Bi_2MoO_6 Z-scheme heterojunction with enhanced visible light photocatalytic activity, J. Catal. 345 (2017) 319–328.

[209] Y. Zhou, G. Chen, Y. Yu, L. Zhao, J. Sun, F. He, H. Dong, A new oxynitride-based solid state Z-scheme photocatalytic system for efficient Cr(VI) reduction and water oxidation, Appl. Catal. B: Environ. 183 (2016) 176–184.

[210] W. Wang, P. Xu, M. Chen, G. Zeng, C. Zhang, C. Zhou, Y. Yang, D. Huang, C. Lai, M. Cheng, L. Hu, W. Xiong, H. Guo, M. Zhou, Alkali metal-assisted synthesis of graphite carbon nitride with tunable band-gap for enhanced visible-light-driven photocatalytic performance, ACS Sustainable Chem. Eng. 6 (2018) 15503–15516.

[211] M.A. Barakat, New trends in removing heavy metals from industrial wastewater, Arab. J. Chem. 4 (2011) 361–377.

[212] Y. Qu, X. Duan, Progress, challenge and perspective of heterogeneous photocatalysts, Chem. Soc. Rev. 42 (2013) 2568–2580.

[213] W. Chen, H. Liu, X. Li, S. Liu, L. Gao, L. Mao, Z. Fan, W. Shangguan, W. Fang, Y. Liu, Polymerizable complex synthesis of $SrTiO_3$:(Cr/Ta) photocatalysts to improve photocatalytic water splitting activity under visible light, Appl. Catal. B: Environ. 192 (2016) 145–151.

[214] X. Wu, J. Zhao, L. Wang, M. Han, M. Zhang, H. Wang, H. Huang, Y. Liu, Z. Kang, Carbon dots as solid-state electron mediator for $BiVO_4$/CDs/CdS Z-scheme photocatalyst working under visible light, Appl. Catal. B: Environ. 206 (2017) 501–509.

[215] R. Niishiro, S. Tanaka, A. Kudo, Hydrothermal-synthesized $SrTiO_3$ photocatalyst co-doped with rhodium and antimony with visible-light response for sacrificial H_2, and O_2, evolution and application to overall water splitting, Appl. Catal. B: Environ. 150–151 (2014) 187–196.

[216] D. Wang, Z. Guo, Y. Peng, W. Yuan, Visible light induced photocatalytic overall water splitting over micro-SiC driven by the Z-scheme system, Catal. Commun. 61 (2015) 53–56.

[217] B.J. Ng, L.K. Putri, L.L. Tan, P. Pasbakhsh, S.P. Chai, All-solid-state z-scheme photocatalyst with carbon nanotubes as an electron mediator for hydrogen evolution under simulated solar light, Chem. Eng. J. 316 (2017) 41–49.

[218] S. Wei, Y. Song, Y. Rong, L. Tang, Y. Chen, A novel Z-scheme Er^{3+}: $YAlO_3$/Ta_2O_5-$CaIn_2S_4$/$MoSe_2$-reduced graphene oxide photocatalyst with superior photocatalytic hydrogen evolution activity, Renewable Energy 111 (2017) 628–637.

[219] F. Peng, Q. Zhou, D. Zhang, C. Lu, Y. Ni, J. Kou, J. Wang, Z. Xu, Bio-inspired design: Inner-motile multifunctional ZnO/CdS heterostructures magnetically actuated artificial cilia film for photocatalytic hydrogen evolution, Appl. Catal. B: Environ. 165 (2015) 419–427.

[220] F.Q. Zhou, J.C. Fan, Q.J. Xu, Y.L. Min, Nanowires decorated with CdS nanoparticles as Z-scheme photocatalyst with enhanced H2 generation, Appl. Catal. B: Environ. 201 (2017) 77–83.

[221] J. Zhao, P. Zhang, J. Fan, J. Hu, G. Shao, Constructing 2D layered MoS_2 nanosheets-modified Z-scheme TiO_2/WO_3 nanofibers ternary nanojunction with enhanced photocatalytic activity, Appl. Surf. Sci. 430 (2018) 466–474.

[222] R. Zhu, F. Tian, G. Cao, F. Ouyang, Construction of Z scheme system of $ZnIn_2S_4$/RGO/$BiVO_4$ and its performance for hydrogen generation under visible light, Int. J. Hydrogen Energy 42 (2017) 17350–17361.

[223] X. Jia, M. Tahir, L. Pan, Z.-F. Huang, X. Zhang, L. Wang, J.J. Zou, Direct Z-scheme composite of CdS and oxygen-defected $CdWO_4$: An efficient visible-light-driven photocatalyst for hydrogen evolution, Appl. Catal. B: Environ. 198 (2016) 154–161.

[224] A. Meng, B. Zhu, B. Zhong, L. Zhang, B. Cheng, Direct Z-scheme TiO_2/CdS hierarchical photocatalyst for enhanced photocatalytic H_2-production activity, Appl. Surf. Sci. 422 (2017) 518–527.

[225] F. Xu, W. Xiao, B. Cheng, J. Yu, Direct Z-scheme anatase/rutile bi-phase nanocomposite TiO_2, nanofiber photocatalyst with enhanced photocatalytic H_2-production activity, Int. J. Hydrogen Energy 39 (2014) 15394–15402.

[226] J.M. Bao, S.K. Jin, H.C. Chang, S.I. Woo, Enhanced hydrogen generation from methanol aqueous solutions over Pt/MoO_3/TiO_2 under ultraviolet light, Int. J. Hydrogen Energy 38 (2013) 3582–3587.

[227] W. Zhao, L. Xie, M. Zhang, Z. Ai, H. Xi, Y. Li, Q. Shi, J. Chen, Enhanced photocatalytic activity of all-solid-state g-C_3N_4/Au/P_{25} Z-scheme system for visible-light-driven H_2 evolution, Int. J. Hydrogen Energy 41 (2016) 6277–6287.

[228] H. Zhao, X. Ding, B. Zhang, Y. Li, C. Wang, Enhanced photocatalytic hydrogen evolution along with byproducts suppressing over Z-scheme $Cd_xZn_{(1-x)}S$/Au/g-C_3N_4 photocatalysts under visible light, Sci. Bull. 62 (2017) 602–609.

[229] K. He, J. Xie, X. Luo, J. Wen, S. Ma, X. Li, Y. Fang, X. Zhang, Enhanced visible light photocatalytic H_2 production over Z-scheme g-C_3N_4 nansheets/WO_3 nanorods nanocomposites loaded with $Ni(OH)_x$ co-catalysts, Chinese J. Catal. 38 (2017) 240–252.

[230] W.P. Hsu, M. Mishra, W.S. Liu, C.Y. Su, T.P. Perng, Fabrication of direct Z-scheme Ta_3N_5-$WO_{2.72}$ film heterojunction photocatalyst for enhanced hydrogen evolution, Appl. Catal. B: Environ. 201 (2017) 511–517.

[231] X. Wang, H. Dong, Z. Hu, Z. Qi, L. Li, Fabrication of a Cu_2O/Au/TiO_2 composite film for efficient photocatalytic hydrogen production from aqueous solution of methanol and glucose, Mater. Sci. Eng., B. 219 (2017) 10–19.

[232] H. Zhou, L. Ding, T. Fan, J. Ding, D. Zhang, Q. Guo, Leaf-inspired hierarchical porous CdS/Au/N-TiO_2 heterostructures for visible light photocatalytic hydrogen evolution, Appl. Catal. B: Environ. 147 (2014) 221–228.

[233] B. Lin, Y. Zhou, L. He, W. Yang, Y. Chen, B. Gao, Mesoporous CdS-pillared $H_2Ti_3O_7$ nanohybrids with efficient photocatalytic activity, J. Phys. Chem. Solids 79 (2015) 66–71.

[234] Y.P. Xie, Y. Yang, G. Wang, G. Liu, Oxygen vacancies promoted interfacial charge carrier transfer of CdS/ZnO heterostructure for photocatalytic hydrogen generation, J. Colloid Interface Sci. 503 (2017) 198–204.

[235] H. Gao, P. Zhang, J. Zhao, Y. Zhang, J. Hu, G. Shao, Plasmon enhancement on photocatalytic hydrogen production over the Z-scheme photosynthetic heterojunction system, Appl. Catal. B: Environ. 210 (2017) 297–305.

[236] D. Ma, J.W. Shi, Y. Zou, Z. Fan, X. Ji, Rational design of CdS@ZnO core-shell structure via atomic layer deposition for drastically enhanαααααced photocatalytic H_2 evolution with excellent photostability, Nano Energy 39 (2017) 183–191.

[237] X. Wang, G. Liu, G.Q. Lu, H.M. Cheng, Stable photocatalytic hydrogen evolution from water over ZnO-CdS core-shell nanorods, Int. J. Hydrogen Energy 35 (2010) 8199–8205.

[238] K. Song, F. Xiao, L. Zhang, F. Yue, X. Liang, $W_{18}O_{49}$ nanowires grown on g-C_3N_4, sheets with enhanced photocatalytic hydrogen evolution activity under visible light, J. Mol. Catal. A: Chem. 418–419 (2016) 95–102.

[239] W.K. Jo, N.C.S. Selvam, Z-scheme CdS/g-C_3N_4 composites with RGO as an electron mediator for efficient photocatalytic H2 production and pollutant degradation, Chem. Eng. J. 317 (2017) 913–924.

[240] D. Wang, Z. Guo, Y. Peng, W. Yuan, A simple route to significant enhancement of photocatalytic water oxidation on $BiVO_4$ by heterojunction with SiC, Chem. Eng. J. 281 (2015) 102–108.

[241] D. Wang, J. Ye, T. Kako, T. Kimura, Photophysical and photocatalytic properties of $SrTiO_3$ doped with Cr cations on different sites, J. Phys. Chem., B 110 (2006) 15824–15830.

[242] Y. Qi, S. Chen, J. Cui, Z. Wang, F. Zhang, L. Can, Inhibiting competing reactions of iodate/iodide redox mediators by surface modification of photocatalysts to enable Z-scheme overall water splitting, Appl. Catal. B: Environ. 224 (2017) 579–585.

[243] W. Yu, J. Chen, T. Shang, L. Chen, L. Gu, T. Peng, Direct Z-scheme g-C_3N_4/WO_3, photocatalyst with atomically defined junction for H_2 production, Appl. Catal. B: Environ. 219 (2017) 693–704.

[244] K.N. Ferreira, T.M. Iverson, K. Maghlaoui, J. Barber, S. Iwata, Architecture of the photosynthetic oxygen-evolving center, Science 303 (2004) 1831–1838.

[245] R.L. House, N.Y.M. Iha, R.L. Coppo, L. Alibabaei, B.D. Sherman, P. Kang, M.K. Brennaman, P.G. Hoertz, T.J. Meyer, Artificial photosynthesis: where are we now? Where can we go?, J Photochem. Photobiol. C: Photochem. Rev. 25 (2015) 32–45.

[246] W. Yu, D. Xu, T. Peng, Enhanced photocatalytic activity of g-C_3N_4 for selective CO_2 reduction to CH_3OH via facile coupling of ZnO: a direct Z-scheme mechanism, J. Mater. Chem. A 3 (2015) 19936–19947.

[247] D. Xu, B. Cheng, W. Wang, C. Jiang, J. Yu, Ag_2CrO_4/g-C_3N_4/graphene oxide ternary nanocomposite Z-scheme photocatalyst with enhanced CO_2 reduction activity, Appl. Catal. B: Environ. 231 (2018) 368–380.

[248] G. Mul, C. Schacht, W.P.M. van Swaaij, J.A. Moulijn, Functioning devices for solar to fuel conversion, Chem. Eng. Process 51 (2012) 137–149.

[249] T. Inoue, A. Fujishima, S. Konishi, K. Honda, Photoelectrocatalytic reduction of carbon dioxide in aqueous suspensions of semiconductor powders, Nature 277 (1979) 637–638.

[250] T. Wang, X. Meng, P. Li, P.S. Ouyang, K. Chang, G. Liu, Z. Mei, J. Ye, Photoreduction of CO_2 over the well-crystallized ordered mesoporous TiO2 with the confined space effect, Nano Energy 9 (2014) 50–60.

[251] X. Meng, S. Ouyang, T. Kako, P. Li, Q. Yu, T. Wang, J. Ye, Photocatalytic CO_2 conversion over alkali modified TiO_2 without loading noble metal cocatalyst, Chem. Commun. 50 (2014) 11517–11519.

[252] J. Wang, L. Zhang, W. Fang, J. Ren, Y. Li, H. Yao, J. Wang, Z. Li, Enhanced photoreduction CO_2 activity over direct Z-scheme α-Fe_2O_3/Cu_2O heterostructures under visible light irradiation, ACS Appl. Mater. Interfaces 7 (2015) 8631–8639.

[253] K.L. Bae, J. Kim, C.K. Lim, K.M. Nam, H. Song, Colloidal zinc oxide-copper(I) oxide nanocatalysts for selective aqueous photocatalytic carbon dioxide conversion into methane, Nat. Commun. 8 (2017) 1156.

[254] T. Ohno, N. Murakami, T. Koyanagi, Y. Yang, Photocatalytic reduction of CO_2 over a hybrid photocatalyst composed of WO3 and graphitic carbon nitride (g-C3N4) under visible light, J. CO2 Util. 6 (2014) 17–25.

[255] J. Jin, J.G. Yu, D.P. Guo, C. Cui, W.K. Ho, A hierarchical Z-scheme CdS-WO_3 photocatalyst with enhanced CO_2 reduction activity, Small 11 (2015) 5262–5271.

[256] J. Wang, C. Qin, H. Wang, M. Chu, A. Zada, X. Zhang, J. Li, F. Raziq, Y. Qu, L. Jing, Exceptional photocatalytic activities for CO_2 conversion on Al-O bridged g-C_3N_4/α-Fe_2O_3 Z-scheme nanocomposites and mechanism insight with isotopes, Appl. Catal. B: Environ. 221 (2018) 459.

[257] Y. Wei, J. Jiao, Z. Zhao, W. Zhong, J. Li, J. Liu, G. Jiang, A. Duan, 3D ordered macroporous TiO_2-supported Pt@CdS core-shell nanoparticles: design, synthesis and efficient photocatalytic conversion of CO_2 with water to methane, J. Mater. Chem. A 3 (2015) 11074–11085.

[258] L. Kuai, Y. Zhou, W. Tu, P. Li, H. Li, Q. Xu, L. Tang, X. Wang, M. Xiao, Z. Zou, Rational construction of a CdS/reduced graphene oxide/TiO_2 core-shell nanostructure as an all-solid-state Z-scheme system for CO_2 photoreduction into solar fuels, RSC Adv. 5 (2015) 88409–88413.

[259] P. Li, Y. Zhou, H. Li, Q. Xu, X. Meng, X. Wang, M. Xiao, Z. Zou, All-solid-state Z-scheme system arrays of $Fe_2V_4O_{13}$/RGO/CdS for visible light-driving photocatalytic CO_2 reduction into renewable hydrocarbon fuel, Chem. Commun. 51 (2015) 800–803.

[260] Y. Bai, L. Ye, L. Wang, X. Shi, P. Wang, W. Bai, P.K. Wong, g-C_3N_4/$Bi_4O_5I_2$, heterojunction with I^{3-}/I^- redox mediator for enhanced photocatalytic CO_2 conversion, Appl. Catal. B: Environ. 194 (2016) 98–104.

[261] Y. Wei, J. Jiao, Z. Zhao, J. Liu, J. Li, G. Jiang, Y. Wang, A. Duan, Fabrication of inverse opal TiO_2-supported Au@CdS core-shell nanoparticles for efficient photocatalytic CO_2 conversion, Appl. Catal. B: Environ. 179 (2015) 422–432.
[262] T. Di, B. Zhu, B. Cheng, J. Yu, J. Xu, A direct Z-scheme g-C_3N_4/SnS_2 photocatalyst with superior visible-light CO_2 reduction performance, J. Catal. 352 (2017) 532–541.
[263] M. Zubair, A. Razzaq, C.A. Grimes, S.I. In, Cu_2ZnSnS_4(CZTS)-ZnO: a noble metal-free hybrid Z-scheme photocatalyst for enhanced solar-spectrum photocatalytic conversion of CO_2 to CH_4, J. CO_2 Utiliz. 20 (2017) 301–311.
[264] G. Song, F. Xin, X. Yin, Photocatalytic reduction of carbon dioxide over $ZnFe_2O_4$/TiO_2 nanobelts heterostructure in cyclohexanol, J. Colloid Interface Sci. 442 (2015) 60–66.
[265] M.E. Aguirrea, R. Zhou, A.J. Eugene, M.I. Guzman, Cu_2O/TiO_2 heterostructures for CO_2 reduction through a direct Z-scheme: Protecting Cu2O from photocorrosion, Appl. Catal. B: Environ. 217 (2017) 485–493.
[266] P. Murugesan, S. Narayanan, M. Manickam, Experimental studies on photocatalytic reduction of CO_2 using AgBr decorated g-C_3N_4 composite in TEA mediated system, J. CO_2 Utiliz. 22 (2017) 250–261.
[267] G. Yang, D. Chen, H. Ding, J. Feng, J. Zhang, Y. Zhu, S. Hamid, D. Bahnemann, Well-designed 3D $ZnIn_2S_4$ nanosheets/TiO_2 nanobelts as direct Z-scheme photocatalysts for CO_2 photoreduction into renewable hydrocarbon fuel with high efficiency, Appl. Catal. B: Environ. 219 (2017) 611–618.
[268] S. Yu, C. Chiu, Y. Wu, C. Liao, V. Nguyen, J. Wu, Photocatalytic water splitting and hydrogenation of CO_2 in a novel twin photoreactor with IO^{3-}/I^- shuttle redox mediator, Appl. Catal. A 518 (2016) 158–166.
[269] V. Nguyena, J. Wu, Recent developments in the design of photoreactors for solar energy conversion from water splitting and CO_2 reduction, Appl. Catal. A 550 (2018) 122–141.
[270] P. Pathak, M. Meziani, L. Castillo, Y. Sun, Metal-coated nanoscale TiO_2 catalysts for enhanced CO_2 photoreduction, Green Chem. 7 (2005) 667–670.